Doctoral theses at NTNU, 2023:358

Torjus Lines Steffensen

Vitals on the wrist

Sensor development for unobtrusive and ubiquitous cardiovascular monitoring

Doctoral thesis

NTNU
Norwegian University of Science and Technology
Thesis for the Degree of
Philosophiae Doctor
Faculty of Medicine and Health Sciences
Department of Circulation and Medical Imaging

NTNU
Norwegian University of
Science and Technology

Torjus Lines Steffensen

Vitals on the wrist

Sensor development for unobtrusive and ubiquitous cardiovascular monitoring

Thesis for the Degree of Philosophiae Doctor

Trondheim, November 2023

Norwegian University of Science and Technology
Faculty of Medicine and Health Sciences
Department of Circulation and Medical Imaging

NTNU
Norwegian University of
Science and Technology

NTNU
Norwegian University of Science and Technology

Thesis for the Degree of Philosophiae Doctor

Faculty of Medicine and Health Sciences
Department of Circulation and Medical Imaging

ISBN 978-82-326-7416-9 (printed ver.)
ISBN 978-82-326-7415-2 (electronic ver.)
ISSN 1503-8181 (printed ver.)
ISSN 2703-8084 (online ver.)

Doctoral theses at NTNU, 2023:358

Printed by NTNU Grafisk senter

Abstract

Cardiovascular monitoring has become ubiquitous with the advent of modern smartwatches and smartphones. We can track our heart rates and oxygen saturation through the day, as we sleep, we can record our breathing rate and how much we toss and turn. Some devices allow for detection of arrhythmia. An additional vital sign has been a high research priority. Tracking blood pressure at the same level of ease and high temporal resolution offers to revolutionize diagnosis and management of hypertension, as well as ambulatory blood pressure research.

Bringing about this vision has proven difficult. Developments in sensor systems, physiological understanding, and signal processing have brought this technology to the cusp of reliability. This thesis presents seven contributions revolving around a central study of a wrist-worn wearable sensor intended to investigate novel approaches for blood pressure estimation. Supporting this study are several sub-projects contributing to technology development and problem understanding.

The primary results indicate that the use of such sensors, in combination with advanced signal processing and deep learning techniques, allows for the non-invasive estimation of blood pressure and arterial stiffness even during moderate to high-intensity exercise. The additional contributions offer insights into the domain applications, further enriching their respective bodies of literature.

Sammendrag

Med moderne smartklokker og smarttelefoner har overvåking av hjerte- og karsystemet blitt dagligdags. Vi kan følge hjertefrekvens og oksygenmetning gjennom dagen, mens vi sover kan vi logge pustefrekvens og hvor urolige vi er. Noen enheter kan også detektere arytmier. En annen parameter har vært en høy forskningsprioritet. Overvåkning av blodtrykk med samme letthet og høye tidsoppløsning kan revolusjonere diagnose og behandling av hypertensjon så vel som ambulant blodtrykksforskning.

Å realisere denne visjonen har vist seg å være vanskelig. Utviklinger innen sensorsystemer, fysiologisk forståelse og signalbehandling har brakt teknologien til randen av pålitelighet. Denne avhandlingen presenterer syv bidrag som bygger opp om en sentral studie av en bærbar sensor ment for å undersøke nye metoder for blodtrykksestimering. Støttende for denne studien er flere underprosjekter som har bidratt til teknologiutvikling og problemforståelse.

Hovedresultatene indikerer at bruk av disse sensorene, i kombinasjon med avansert signalbehandling og maskinlæringsteknikker som dyp læring, muliggjør ikke-invasiv estimering av blodtrykk og arteriestivhet selv under moderat til høy intensitet trening. De ytterligere bidragene gir innsikt i respektive domeneapplikasjoner og beriker den respektive litteraturen.

What makes it difficult is that research is immersion in the unknown. We just don't know what we're doing. We can't be sure whether we're asking the right question or doing the right experiment until we get the answer or the result.

If we don't feel stupid it means we're not really trying.

Martin Schwartz

Acknowledgements

I distinctly remember a conversation at the Trondheim Student Society sometime in the spring or summer of 2019. I was being encouraged to pursue a PhD at TrollLABS with Professor Martin Steinert, like my two drinking companions had recently done. I told them that was the stupidest idea I'd ever heard.

To my fellow travellers: thank you.

Thank you, Martin, for the patience, for the encouragement when I didn't see what I had, and most of all for creating TrollLABS.

Trolls and colleagues: Håvard, Marius, Sampsa, Sindre, Kim, Henrikke, Daniel, Pasi, Evangelos, Ole, Øystein, Kjetil, Vetle. Nothing happens in a vacuum. Thank you for filling the empty spaces, thank you for the conversations, thank you for the coffee. Thank you for giving so much of who you are to create this thing we've been a part of. It's not always been great, in fact, it's often been crushing and disappointing. But at its best it has been some of the best and most beautiful time of my life.

To those who went before: thank you to Heikki, Carlo, Achim, Jørgen, Fredrik, and the others who rightly feel left out. Thank you for leaving a legacy to build on, one that says anything goes so long as it's not boring.

To my MyMDT collaborators: better late than never. Thank you, Filip and Emma, in particular.

To family, distant relations, enemies, friends near and far: thank you for always being there, even if I haven't been. To my parents, thank you for your patience and for letting me figure things out on my own. To my sister, thank you for the capybaras.

It's been real.

Trondheim, Summer 2023.

Table of Contents

List of Abbreviations

ABP	Arterial Blood Pressure
AI	Augmentation Index
AUC	Area Under Curve
AVO	Aortic Valve Opening
BCG	Ballistocardiography
BP	Blood Pressure
BPM	Beats Per Minute
CNN	Convolutional Neural Network
CV	Cardiovascular
CVD	Cardiovascular Disease
CWT	Continuous Wavelet Transform
DBP	Diastolic Blood Pressure
ECG	Electrocardiography
EEMD	Ensemble Empirical Mode Decomposition
EMD	Empirical Mode Decomposition
FF	Form Factor
FFT	Fast Fourier Transform
HF	High Frequency
HR	Heart Rate
IBP	Invasive Blood Pressure
ICG	Impedance Cardiography
IPG	Impedance Plethysmography
LVOT	Left Ventricle Outflow Tract
MAE	Mean Absolute Error
MAP	Mean Arterial Pressure
MEMS	Microelectromechanical System
ML	Machine Learning
NIBP	Non-Invasive Blood Pressure
PAT	Pulse Arrival Time
PCG	Phonocardiography
PEP	Pre-Ejection Period
PPG	Photoplethysmography
PTT	Pulse Transit Time
PWV	Pulse Wave Velocity
RMSE	Root Mean Square Error
SBP	Systolic Blood Pressure
SCG	Seismocardiography
STFT	Short-Time Fourier Transform
SVM	Support Vector Machine

Table of Figures

1 Introduction

Continuous, unobtrusive monitoring of our vital signs is rapidly becoming part of our daily lives. Technology is now at a point of maturity where more and more of our vital signs can be monitored ubiquitously with reasonable accuracy. The reader might themselves be wearing a smart watch continuously recording heart rate (HR), peripheral oxygen saturation, and respiratory rate.

Another vital sign is becoming ubiquitously measurable through new technologies. Cuffless noninvasive blood pressure (BP) measurement is a particularly high priority area of wearable sensor research. Regular BP monitoring is key to both diagnosis and management of hypertension (Kitt et al., 2019; Stergiou et al., 2014), a leading contributor to global morbidity (H. Wang et al., 2016). Going beyond the paradigm of regular cuff sphygmomanometer measurement is a vision of ubiquitous smartphone or smartwatch-based monitoring, heightening mass awareness, thus driving diagnosis. High temporal resolution longitudinal monitoring —often compared to going from still photos to video – would offer unobtrusive insight into BP throughout an individual's day to day life, potentially revolutionizing hypertension management. Beyond hypertension management, convenient continuous measurement of BP trends in the clinical setting could improve detection of hypotension, potentially improving outcomes for patients during post-surgical recovery (Maheshwari et al., 2018; Sessler & Saugel, 2019).

This motivation sets the stage for intense research effort in realizing this potential. In this thesis, I present my contributions towards this goal.

1.1 Scope

The work was done under the PhD program in medical technology at the Faculty of Medicine and Health Sciences at the Norwegian University of Science and Technology. The project consisted of

a primary study and several supportive sub-projects. The core study focused on the development of a wearable sensor, encompassing a process of concept selection and iterative prototyping, experimentation and data collection, and extensive data analysis. This involved creating and prototyping technology for experiments, from benchtop test rigs to invasive in-clinic measurements in healthy volunteers. As such, there was a strong development phase transitioning into a human subject measurement phase.

Complementing the core study were several sub-projects. They either emerged from the work on the main study or were initiated to develop the necessary tools, skills, and understanding to support the larger study. The tools and methods used have involved rapid prototyping, low-volume fabrication techniques, electronics design, benchtop testing and human subject research.

The overarching objectives of this thesis, reflecting the divided nature of the work, are:

1. **Primary Research Objective**
   Develop wearable technologies that allow for ubiquitous and non-invasive cardiovascular monitoring towards enabling close-to beat-to-beat blood pressure monitoring via iterative development, benchtop test rigs, and human trials.
2. **Secondary Research Objective**
   To achieve the primary objective, generate insights into wearable sensor design and development techniques as they apply to cardiovascular monitoring in noisy situations, including prototyping and experimental techniques relevant to sensor design.

To target the research objectives, the work has been divided into the following research tasks:

Primary Research Objective:

Research Task 1. To develop and use lab test rigs to benchmark devices for wearable cardiovascular monitoring, focusing on tonometer-derived pulse wave analysis and ballistocardiography

Research Task 2. To develop devices measuring physiologically relevant variables using these techniques to probe central cardiac events distally

Research Task 3. To test these devices under a broad range of physiological states in healthy volunteers against ground truth invasive measurements

Secondary Research Objective:

Research Task 4. To develop methods for simulating and benchmarking relevant artifacts of the cardiovascular system

Research Task 5. Develop and apply signal processing methods to obtain usable results in high noise scenarios

Research Task 6. Contribute to an understanding of prototyping methods in the concept selection phase of sensor product development.

The research tasks resulted in 7 contributions, of which 4 have been published in international peer-reviewed scientific publications. One article is under review as of this writing.

The rest of this chapter will present the contributions that are presented as part of this thesis. Following this, chapter 2 contains a review of current approaches in wearable and unobtrusive cardiovascular (CV) monitoring, with an emphasis on BP estimation. It aims to provide a current view of the field of ubiquitous and unobtrusive blood pressure (BP) measurement, focusing on underlying sensors and enabling technologies. Chapter 3 presents views and approaches to address some general aspects of physiology sensor design problems.

Chapter 4 will present the main study undertaken in this project, including ethical considerations, methods, and preliminary results in BP estimation, intended for further analysis and future publication. At the end of the thesis, in chapter 5, I will conclude with a summary of the research and my thoughts on the future direction of the field with suggestions for further research.

1.2 Present contributions

Individual contributions that have been generated as part of the project work are presented here. Seven concrete research contributions have been generated over the course of the project.

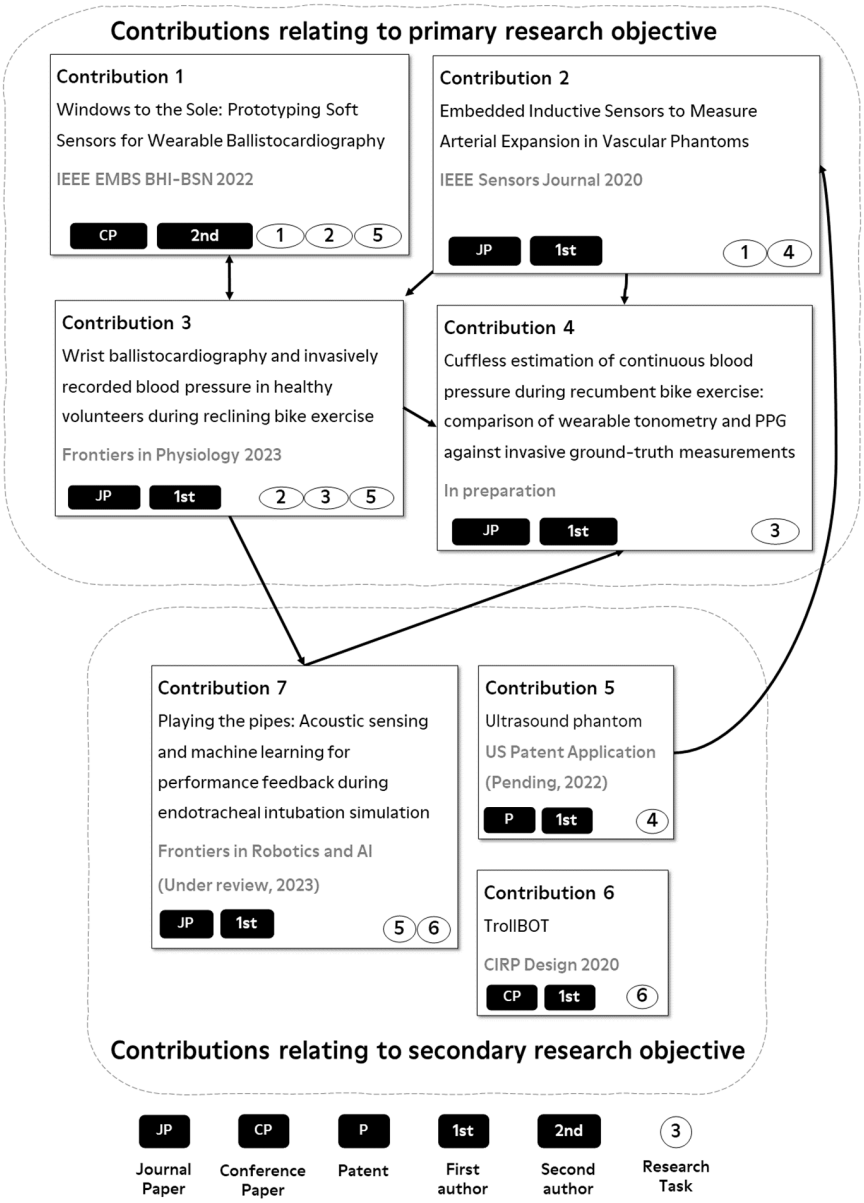

Figure 1. Relationship between contributions in this thesis. Solid lines indicate direction of influence.

The contributions comprise scientific papers published in international peer reviewed journals and conference proceedings, a patent application, and one abstract describing a manuscript in preparation based on the preliminary results presented in chapter 3.

The contributions are grouped by research objective, as illustrated in Figure 1. Note that there is overlap between research tasks addressed by each contribution. For the scientific papers, each contribution lists the Norwegian Register for Scientific Journals, Series and Publishers level ("HK-Dir Level") for each of the outlets.

Many of the concepts and abbreviations presented in the following section will be explained in greater detail in chapter 2.

1.3 Contributions relating to the Primary Research Objective

1.3.1 Contribution 1

Title:	Windows to the Sole: Prototyping Soft Sensors for Wearable Ballistocardiography
Authors:	Simon Gjerde, Torjus Steffensen, Håvard Vestad, and Martin Steinert
Status:	Published 2022. IEEE-EMBS International Conference on Wearable and Implantable Body Sensor Networks (BSN). Peer reviewed conference article, HK-Dir Level 1.
Purpose:	This paper describes a prototype sensor device for continuously recording the whole-body force BCG in a wearable insole, demonstrating that the proposed method combining fluid bladders and a distal PPG sensor is capable of recording PTT under a physiological intervention.
Author's contributions:	Proposed the research, designed the experiment, analyzed the sensor data, outlined the paper, revised the manuscript, and presented the paper at the IEEE BHI-BSN 2022 conference.

Background

Much of the early work in the revival of ballistocardiography (BCG) around 2010 and to this day has focused on recording the force BCG, that is, the direct reaction caused by the movement of the body's center of mass during the cardiac cycle. Yet most wearable techniques for BCG focus on recording acceleration at the chest (seismocardiography, or SCG). By capturing the force BCG in the form of an insole, we aimed to investigate the potential of this under-investigated technique in a wearable setting.

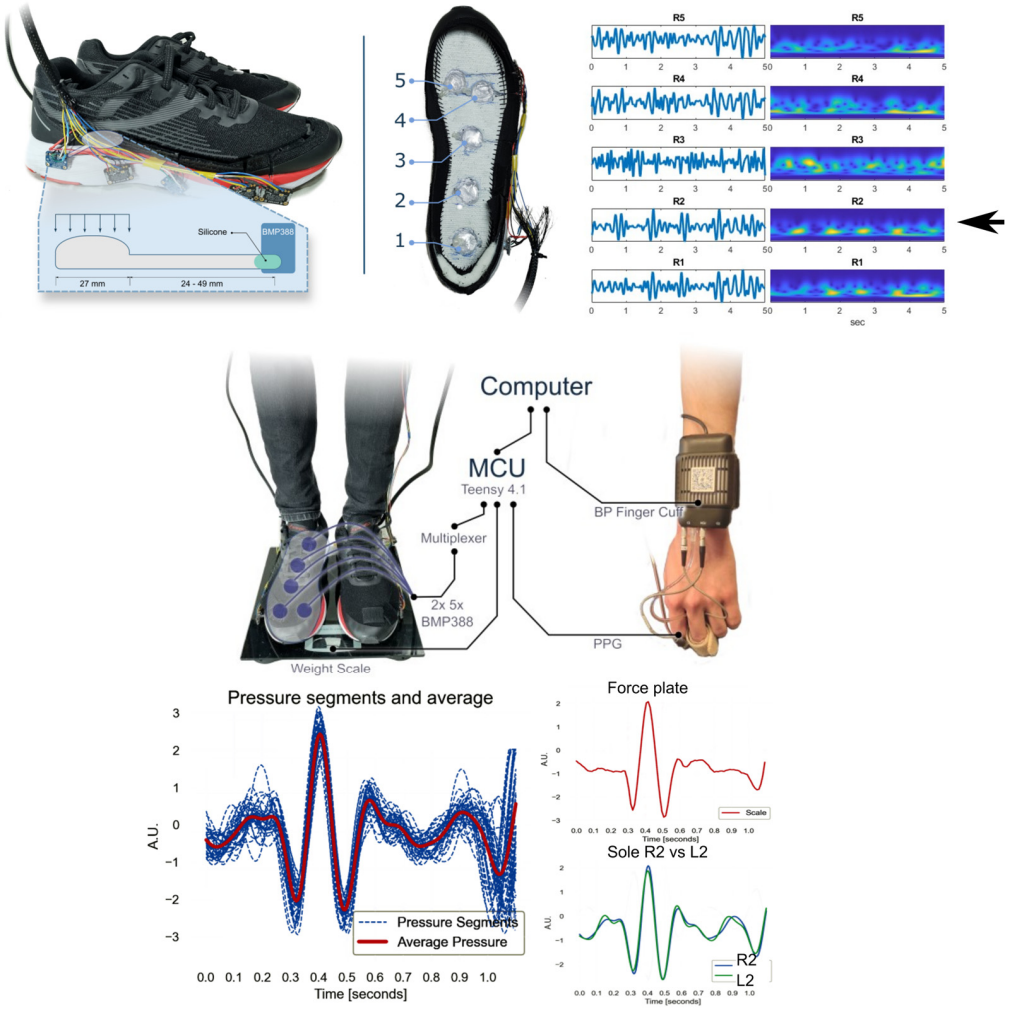

Figure 2. Summary illustrations from Contribution 1, illustrating the prototype concept, the measurement setup during the experiment and sample data. Adapted from Gjerde et al., 2022. See Appendix 1.

The concept

At the end of an iterative process the final prototype consisted of an array of fluid-filled bladders connected to digital barometric pressure sensors. The prototype was designed to estimate the pulse transit time against continuous blood pressure. The soft bladders in the soles of the shoes served as a compliant interface between the sensing unit and the body, and the pressure sensor IC was de-lidded and a thin layer of silicone was applied in the end of the tube, creating a waterproof

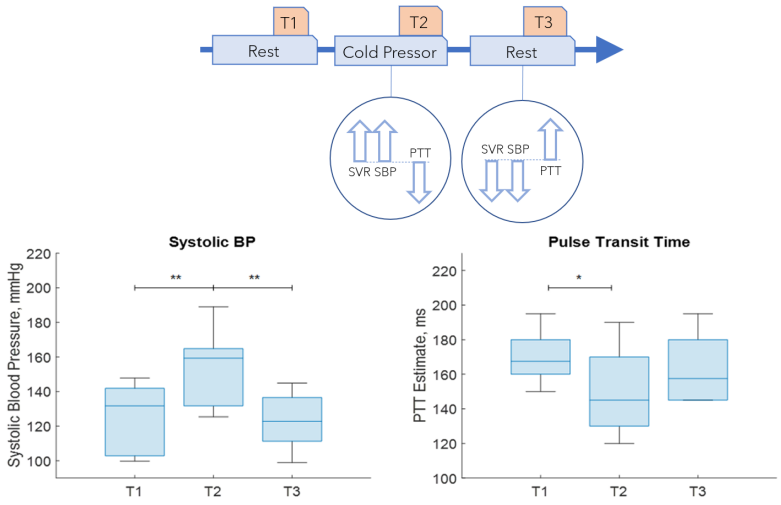

Figure 3. Schematic representation of the cold pressor experiment and the results. SBP: Systolic Blood Pressure, SVR: Systemic Vascular Resistance, PTT: Pulse Transit Time.

interface to the sensor. The prototype was designed to be used in conjunction with a commercial fingertip reflectance photoplethysmography (PPG) sensor for the estimation of pulse transit time.

Research approach

The research approach in this study was primarily experimental, with the development of a prototype sensor system for recording ballistocardiograms in a wearable format. The prototype consisted of an array of soft bladders filled with water, which were integrated into the soles of a pair of shoes and connected to barometric pressure sensors.

To assess the ability of the sensor shoe to record physiologically relevant cardiovascular information, an experiment was carried out to record pulse transit times (PTT) and BP during a cold pressor intervention. 14 healthy volunteers undertook a cold pressor test while wearing the sensor shoes and standing on top of a modified bathroom weigh-scale to record comparison BCG using a standard literature method. Simultaneous recordings were taken of the sole pressure arrays, finger-clip photoplethysmography, and continuous blood pressure via the volume-clamp method.

Key findings

The key findings of the study were that the waveform of the ballistocardiograms captured by the proposed sensor system corresponded well to the simultaneously collected waveforms from the reference weigh-scale. Furthermore, PTT estimated from shoe BCG and PPG showed inverse correlation to vasoconstriction-induced BP increase. This demonstrated the potential of sensorized insoles as a wearable interface for cardiovascular monitoring. Important insights on sensor placement for BCG signal acquisition were also obtained.

Implications

The study demonstrated the feasibility of shoes as a vector for PTT measurement, potentially facilitating development of new methods of wearable CV monitoring in an under-investigated context. Such a device could also be useful for other applications, such as gait analysis. The findings suggest that further development is needed to improve the robustness and reliability of the sensor system, particularly in terms of the fluid-filled bladders and the placement of the sensors.

1.3.2 Contribution 2

Title:	Embedded Inductive Sensors to Measure Arterial Expansion in Vascular Phantoms
Authors:	Torjus Steffensen, Marius Auflem, Håvard Vestad, and Martin Steinert.
Status:	Published 2022. IEEE Sensors Journal. Peer reviewed journal article, HK-Dir Level 2.
Purpose:	To assess the usability of inductive coils in a weaved pattern to accurately record minute diameter changes in vascular simulators of different diameters, roughly corresponding to the brachial and radial arteries.
Author's contributions:	Wrote the manuscript, co-ideated the research, designed experiments, derived and applied the theoretical model, built the phantom test rig and analyzed the waveform data.

Background

This study was conducted to assess the potential of inductive coils arranged in a weaved McKibben pattern around a viscoelastic tube for accurately recording minute diameter changes in vascular simulators. These simulators were designed to mimic the diameters of the brachial and radial arteries and their dilation and constriction over the course of the cardiac cycle.

The research was driven by the lack of clear understanding of the relationship between the internal arterial pressure in the radial artery and the pressure exerted on a pressure-sensitive element in the context of wearable tonometry, where complete applanation cannot be assumed. Tubular phantoms are commonly used for experiments in vascular mechanical modeling, but to enable direct observation are often isolated, outside the tissue that would normally surround arteries.

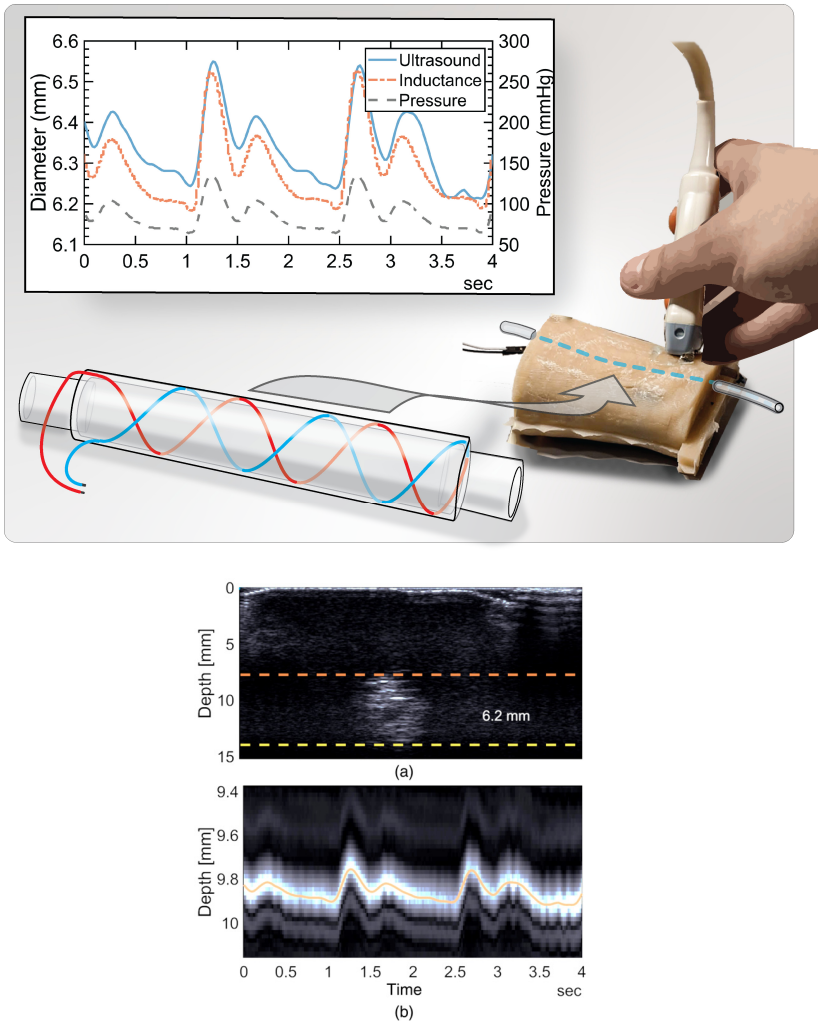

Figure 4. Overview of the vascular phantom with weaved coil surrounding a viscoelastic tube representing the radial artery. Ultrasound B-mode (above) and M-mode (below) recording under pulsatile pressure (right). Depth was corrected for material speed of sound.

Methods

The research involved the development of lab test rigs and the design and execution of a series of experiments. These experiments were guided by a theoretical model based on the thin solenoid model. The model and the experimental design were aimed at estimating arterial expansion due to

pulse pressure via induced changes in coil inductance, compared against an optical deflection measurement and an M-mode ultrasound investigation.

Key findings

The inductive sensors were very sensitive and proved capable of detecting small changes in diameter caused by differences in internal pressure with high fidelity. By applying the thin solenoid model, differences in diameter estimate and measurement was low. The sensors exhibited some drift and hysteresis, likely due to thermal and viscoelastic effects. Despite these challenges, the resolution of the sensors was found to be satisfactory for deformations in the tenths of a millimeter range.

Implications

The demonstrated potential of the inductive sensors suggests that they could be a valuable component of vascular phantoms, where diameter expansion under pressure fluctuations is of particular interest as arterial compliance is an important parameter in vascular mechanics. Similar structures could also be of interest in other areas where accurate measurement of tubular diameter changes is needed, for example mold channel cleaning or in arterial palpation simulators.

Experience and skills developed over the course of this study contributed to an understanding of arterial BP waveform data, used in Contribution 3 and 4.

1.3.3 Contribution 3

Title:	Wrist ballistocardiography and invasively recorded blood pressure in healthy volunteers during reclining bike exercise
Authors:	Torjus Steffensen, Filip Schjerven, Hans Martin Flade, Idar Kirkeby-Garstad, Emma Ingeström, Fredrik Solberg, and Martin Steinert
Status:	Published 2023. Frontiers in Physiology. Peer reviewed journal article, HK-Dir Level 1.
Purpose:	To explore wrist BCG under more extreme physiological perturbations than had previously been done, to observe morphological evolution with increased cardiovascular load, explore relationship between wrist-based BCG-PPG PTT and arterial blood pressure (ABP) and explore any serendipitous observations.
Author's contributions:	Wrote the manuscript, conceptualized the paper, prototyped the sensor hardware and software, recruited participants, analyzed the data, revised regulatory filing for use of novel medical device and wrote risk assessment.

Background

The study aimed to assess the feasibility of wrist acceleration BCG during exercise for estimating PTT. The study also examined the relationship between PTT, BP, and stroke volume (SV) during exercise and posture interventions.

Methods

25 participants underwent a bike exercise protocol with four incremental workloads (0 W, 50 W, 100 W, and 150 W) in supine and semirecumbent postures. BCG, invasive artery BP (ABP) in the radial artery, tonometry, photoplethysmography (PPG) and echocardiography were recorded.

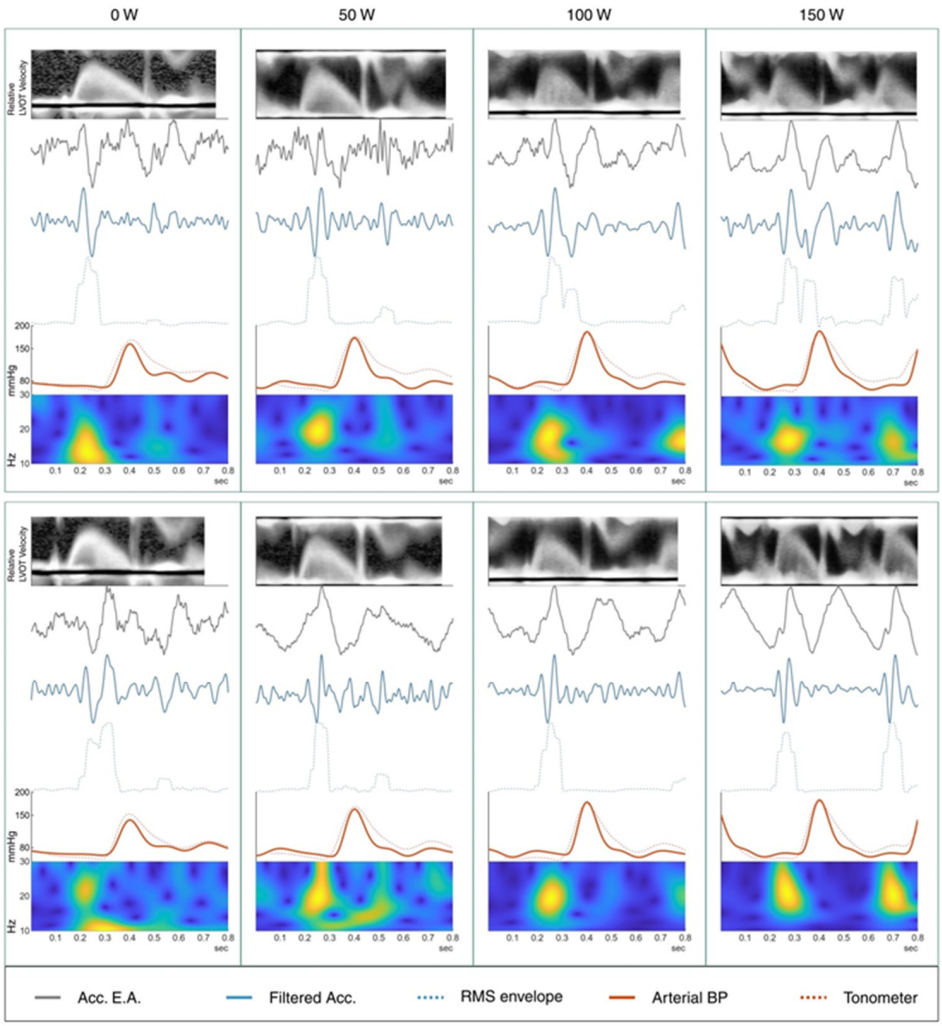

Figure 5. Ensemble averages of various cardiovascular signals from a male participant during eight exercise conditions, in both supine and semirecumbent positions. It displays left ventricle outflow tract (LVOT) flow velocity, accelerometer readings (raw, filtered, and RMS envelope), arterial blood pressure (ABP) alongside the average tonometer signal, and a scalogram of the accelerometer signals. A prominent feature between 0.2 and 0.3 seconds in the scalograms, possibly related to rapid ventricle ejection, is also observed in the filtered ballistocardiogram (BCG). Illustration from Steffensen, 2023.

Ensemble averages of BCG signals, decomposed using ensemble empirical mode decomposition (EEMD), determined aortic valve opening (AVO) timings, combined with peripheral pulse wave arrival times to calculate PTT. The association between filtered BCG features and AVO was confirmed by echo Doppler derived blood flow velocity tracings in the left ventricle outflow tract.

Key findings

BCG was successfully recorded at the wrist during exercise. PTT exhibited a moderate negative correlation with systolic BP. PTT differences between supine and semirecumbent conditions were significant at 0 W and 50 W, less at 100 W and 150 W.

Although the signal is weak, wrist BCG may allow convenient PTT and possibly SV tracking during exercise, enabling studies of cardiovascular response to acute exercise and convenient monitoring of cardiovascular performance. Developments in instrumentation and signal processing are likely necessary to create a practical measuring system. That the AVO signal appeared to become more distinct at higher levels of exercise is intriguing.

1.3.4 Contribution 4

Title:	Cuffless estimation of continuous blood pressure during recumbent bike exercise: comparison of wearable tonometry and PPG against invasive ground-truth measurements
Authors:	Torjus Steffensen, Filip Schjerven, Hans Martin Flade, Idar Kirkeby-Garstad, Emma Ingeström, Fredrik Solberg, and Martin Steinert
Status:	Abstract. Manuscript is in preparation.
Purpose:	To demonstrate methods of noninvasive cuffless BP estimation during controlled laboratory exercise setting against gold-standard ground truth data in healthy volunteers. To compare performance between wearable tonometry and PPG signals for cuffless BP estimation during exercise.
Author's contributions:	Prototyped the sensor hardware and software, revised regulatory filing for use of novel medical device and wrote risk assessment, recruited participants, analyzed the data, conceptualized the paper.

Background

Continuous, noninvasive and cuffless BP estimation during moderate to high intensity exercise using convenient wearable sensors is underinvestigated in the literature. CV response to exercise, including BP, is known to contain valuable markers of cardiovascular disease (CVD) risk. Personal health tracking and longitudinal observational studies also motivate continuous tracking in non-static conditions.

Recently, European Society of Hypertension recommendations mandate exercise tests for cuffless BP estimating devices whose predictive models are based on population data. Against this backdrop, more research is needed on how common machine learning (ML) models perform on exercise data.

Methods

The data are from the data collection described in chapter 4 and in Contribution 3. The methods are described in chapter 4.

Key findings and outlook

Single-source waveform data – both PPG and tonometry – is capable of estimating BP trend changes during moderate bicycle exercise. This work adds to the literature demonstrating potential of noninvasive waveform data for continuously estimating BP during exercise. We would hypothesize that, as tonometry is more directly related to the intraarterial pressure, tonometry models ought to outperform PPG models, which is borne out by the results. However, tonometry is more reliant on accurate sensor placement, possibly limiting data availability.

Models combining data from both sources should be investigated as well as different model architectures.

1.4 Contributions relating to the Secondary Research Objective

1.4.1 Contribution 5

Title:	Ultrasound phantom
Authors:	Torjus Steffensen, Carlo Kriesi, Martin Steinert, Thomas Lafrenz, Jostein Brede, and Marius Auflem
Status:	US patent pending.
Purpose:	Commercialization of a developed technology for simulating arterial access or other ultrasound-guided medical procedures using a combination of easily processed materials whose properties in combination provide a superior tactile response as well as realistic representation on normally calibrated ultrasound imaging equipment.
Author's contributions:	Primary inventor, developed the technology, iteratively implemented the technology in commercial products sold to an outside partner, contributed to application revisions.

Background

The simulation of arterial access and other ultrasound-guided medical procedures currently involve either virtual methods using synthetic imagery and sham tools or physical trainers built from materials with properties similar to human tissue. Although the virtual method has the advantage of endless repetition, it lacks the tactile feedback necessary for many procedures. Physical trainers, while capable of mimicking the sensation of a needle moving through various tissue types, are often hampered by durability concerns.

Hydrogels like gelatin and silicone polymers, while each offering some advantages, have significant drawbacks in either shelf stability or mechanical properties. Yet, with ultrasound-guided procedures increasingly becoming a standard of care for radial cannulation, there's a pressing need for an improved, more realistic simulation approach.

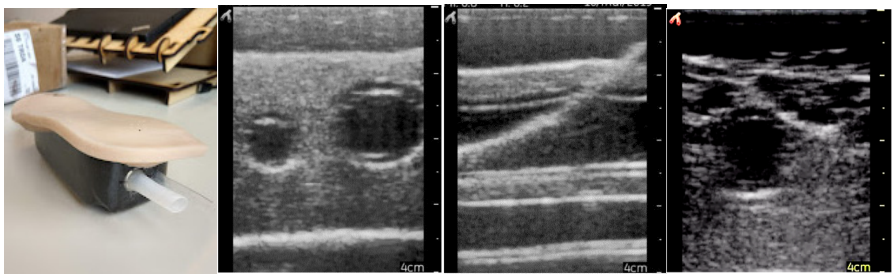

Figure 6. From left to right: photo of a phantom module representing part of the groin, including a simulated femoral artery and vein. Cross sectional ultrasound image of a representative phantom, showing the included structures. In-line view of the artery being punctured, verifying correct introduction of a catheter. Ultrasound capture of a real femoral artery and vein captured using the same device. Note that while phantom is intentionally simple and pedagogical, a wide range of echo can be generated as in the real tissue. Also note that imaging gain will be adjusted dynamically during acquisition, affecting brightness and contrast.

The patent describes a new phantom model that combines the best aspects of both worlds. By integrating an acoustically compliant hydrocarbon polymer gel with a protective silicone rubber coating, the resulting composite structure that exhibits excellent mechanical properties during cannulation and provides a highly realistic ultrasound image.

Methods

We combined a hydrocarbon polymer gel with a silicone rubber protective coating. The polymer gel melts at around 70 degrees Celsius, allowing it to be poured into a mold. The silicone polymer layer solidifies at room temperature and is cast into shape. By adding inclusions in the mold and varying the amount of echogenic dopants in the gel and rubber, the resulting composite structure can mimic various anatomical features.

The development process involved iterative physical prototyping with rapid iterations and user interaction. This iterative process allowed us to better understand the underlying physical principles and to eventually craft a usable product. The phantom's performance was evaluated based on feedback from expert users and objective comparisons using real devices.

Key findings

Our phantom showed promising results with an acceptable unit cost, a superior tactile response, and a realistic ultrasound image. It was noted by expert users as being superior in tactile and ultrasound realism to the leading commercial alternative. Notably this phantom technology has been effectively implemented in a training program for prehospital REBOA (Brede et al., 2019), and was continually used by the Norwegian Air Ambulance Foundation for maintenance training in the REBOA procedure leading up to a larger multi-center study, attesting to its practical applicability and potential in clinical training scenarios.

The skills learned from this project informed work on the vascular benchtop simulator presented as part of the work published in Contribution 2.

1.4.2 Contribution 6

Title:	TrollBOT: A Spontaneous Networking Tool Facilitating Rapid Prototyping of Wirelessly Communicating Products
Authors:	Torjus Steffensen, Sampsa Kohtala, Håvard Vestad, and Martin Steinert
Status:	Published 2020 in Procedia CIRP. Peer reviewed conference paper, HK-Dir Level 1
Purpose:	Develop tools for easier collaboration in mechatronics prototyping in an early phase student lab setting
Author's contributions:	Wrote the manuscript, contributed to concept development and code implementation, presented the paper at CIRP Design 2020.

Summary of the Paper

The paper presents TrollBOT, an Arduino library developed to facilitate rapid prototyping of wirelessly communicating products. The authors developed this tool in response to the need for designers to quickly implement and test new functionalities, particularly in the realm of wireless communication technologies.

Methods of Interest

TrollBOT simplifies the implementation of wireless communication between two or more Arduinos, using inexpensive nRF24-based radio transceivers to form nodes in a tree topology. The library is designed to minimize the learning of new language syntax, allowing all nodes to be programmed from a single master node, reducing the amount of code that needs to be written compared to similar existing solutions.

Key findings

The authors found that TrollBOT offers a clear advantage in terms of the required number of logic lines of code needed to program a simple example scenario. The library enables even a novice user to establish a wireless network quickly. After the library was made available to other lab users, it disseminated to other project groups as an example of in-lab skill sharing, allowing these groups to make their own "skill-jumps" as they had an easy-to-use starting point for their own applications.

Implications of the Work

The TrollBOT library facilitates rapid prototyping and testing of design concepts early in the design process, aligning with the research objective of contributing to an understanding of prototyping methods in the concept selection phase of product development. The library's user-friendly design can help lower the barrier to entry for designers and researchers working on wireless communication technologies, contributing to the goal of advancing the field of mechatronics prototyping.

1.4.3 Contribution 7

Title:	Playing the pipes: Acoustic sensing and machine learning for performance feedback during endotracheal intubation simulation
Authors:	Torjus Steffensen, Brage Bartnes, Maja Fuglstad, Marius Auflem, and Martin Steinert
Status:	Under review (2023). Frontiers in Robotics & AI. Peer reviewed journal article, HK-Dir Level 1.
Purpose:	To demonstrate application of ultrasonic acoustic sensing in combination with machine learning techniques to determine the geometry of a complex multi-material structure at a distance. Secondarily, to obtain skills in using NN models in time series machine learning applications.
Author's contributions:	Wrote the manuscript, co-ideated the research, designed the experiment, developed the transfer learning pipeline, and analyzed the results.

Background

This paper explores the application of ultrasonic acoustic sensing combined with machine learning techniques to classify the geometry of a complex multi-material structure from a distance. The study was conducted in the context of simulated endotracheal intubation, a critical medical procedure that requires precise skill. The primary objectives of the research were to develop and apply signal processing methods for noisy time series data in challenging scenarios and to contribute to understanding of prototyping methods in the sensor product development phase.

Concept

In the context of endotracheal intubation, novice learners practice on simulated airways. Performance feedback is a crucial aspect of training, but in the case of intubation the procedure is not visible from the outside. The simulated airway is a painstakingly accurate model, placing

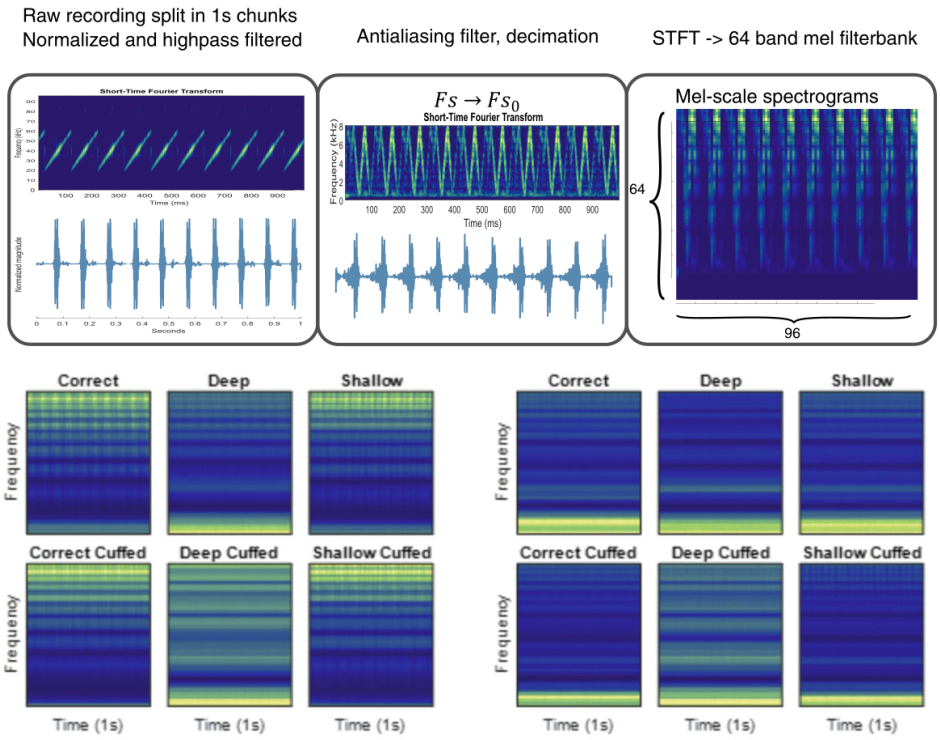

Figure 7. Preparation of spectrograms used for input to the classifier.

sensing devices in the airway can interfere with the tactile sensations that the trainers are relying on. To assess the location of the tube, acoustic sonar is an option, but the highly complex multi-material geometry of the simulated airway makes this difficult. However, we hypothesized that we can sidestep the limitations of traditional sonar by re-framing the problem as a classification problem and applying pre-trained sound classification models, which have seen tremendous technical advances in recent years. We focus on two critical failure modes that can occur: incorrect placement of the tube, either too far or too shallow, and insufficient inflation of the balloon cuff surrounding the tube after placement, resulting in 6 distinct geometrical configurations together with the 'correct' state for each variable.

Methods

We designed an experiment using a simulated airway in a commercially available patient simulator. Piezo buzzers were used to generate ultrasonic acoustic signals in the airway. These signals were

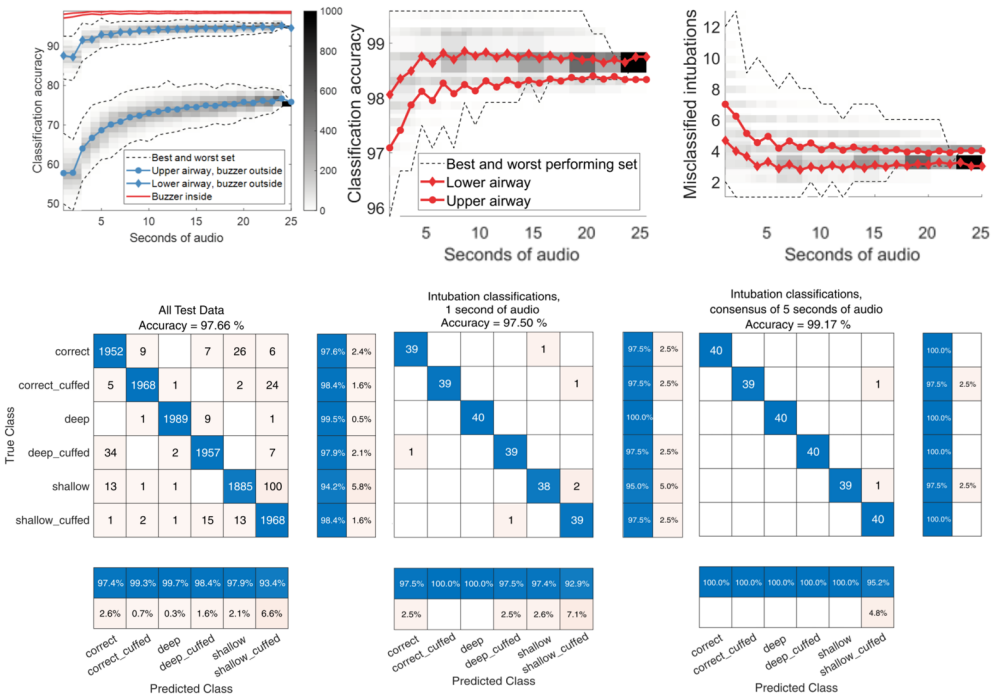

Figure 8. Bootstrap sensitivity analysis of input size on CNN performance. Adapted from (Steffensen et al., Submitted).

captured by microphones in two locations. The combination of different emitter and receiver locations let us compare the effects of noise and distance on the model performance, and to make concrete recommendations on sensor placement. The audio signals were preprocessed and used to train two machine learning models: a Support Vector Machine (SVM) and a Convolutional Neural Network (CNN) pretrained on the publicly available YAMNet dataset.

We developed a transfer learning pipeline to adapt the CNN to the task of classifying the acoustic signals according to the geometry of the simulated airway. The performance of the models was evaluated based on their ability to accurately classify the signals using a leave-one-group-out cross-validation scheme. Influence of input sound duration on classifier performance was estimated using a bootstrap resampling scheme.

Key findings

The CNN model significantly outperformed the SVM model in classifying the acoustic signals. The best model performed very well, attaining global accuracy above 97% on a set of 12,000 one-second clips. The best performance was achieved when the microphone was placed inside the closed airway tubing and the buzzer was in the lower airway audio configuration. The higher frequency range appeared to be important for classification performance, even with aggressive compression and aliasing.

Implications

The successful application of acoustic sensing and machine learning techniques to determine airway geometry could enhance the quality of feedback and performance metrics in medical simulation, potentially leading to better training outcomes. Future work could explore the robustness and generalizability of this approach in different training scenarios and environments. This study is also a practical example of the application of transfer learning into a mechanical engineering design context, adding to the literature on out-of-domain application of ML models.

The practical experience gained in the development and testing of the system contributed necessary experience to develop and train the CNN models described in chapter 4 and Contribution 4.

2 Cardiovascular monitoring

This chapter intends to provide a brief overview of current developments in the field of unobtrusive CV monitoring with an emphasis on BP estimation. Theoretical principles and approaches are followed by commonly used sensor types and selected signal processing topics. The selection of references is not intended to provide an authoritative description of the presented technologies, but rather to give a broad overview of current directions. Relevant contributions of this thesis are placed into context.

Here, we use the terms "ubiquitous" and "unobtrusive" to mean the following:

Ubiquitous collection of CV data is the goal of reliable, continuous data collection regardless of location of activity. This is hoped to be enabled by developments in wearable technology.

Such measurements should be *unobtrusive*: noninvasive and nondisruptive. A successful unobtrusive device should seamlessly integrate in daily life for consistent data collection.

2.1 Current approaches in cuffless BP estimation

Ubiquitous cardiovascular sensing is hoped to enable a breadth of benefits to diverse groups of people. For consumers, longitudinal monitoring of cardiovascular health may contribute to early detection of cardiovascular disease (CVD) by alerting the user to worrying changes in CV parameters, and can be useful in behavior change interventions (Brickwood et al., 2019; Piwek et al., 2016). In healthcare, clinically significant applications of wearable monitoring are growing while facing a number of technical bottlenecks (Lu et al., 2020). Use in health research is growing into an increasingly diverse field with a broad scope of interests (Huhn et al., 2022). Outside of wearables, incentives to reduce costs in the healthcare sector motivate non-contacting technologies for unobtrusive CV monitoring of patients and care receivers (see e.g. Jung et al., 2021, 2022; Lydon et al., 2015; Rosales et al., 2017).

Clinical need and technological opportunity have driven recent developments in unobtrusive CV measurement. Primary applications are heart rate monitoring, arrhythmia detection and BP estimation. Cuffless BP estimation in particular is a highly active research topic with multiple different technologies under investigation, and several devices have recently reached market. As yet, however, the accuracy of these devices is doubted and none are yet considered reliable enough for clinical use (Stergiou et al., 2022).

A comprehensive review of cuffless BP technology lays out the fundamental case for the technology (Mukkamala et al., 2022):

> Eliminating the cuff from noninvasive BP measurement is necessary for addressing the following issues:
>
> 1) Hypertension awareness by bringing regular BP monitoring to the masses during daily life
> 2) Long-term hypertension control by continually monitoring and revealing high BP readings to individual patients
> 3) Precise hypertension evaluation and diagnosis by affording unobtrusive BP monitoring during the day and night
> 4) Hypotension surveillance and therapy by providing seamless, continuous BP monitoring

> Furthermore, by furnishing unprecedented BP data during all daily circumstances rather than merely providing snapshots of the BP profile (e.g., video versus pictures), the cuffless paradigm could revolutionize hypertension evaluation and management altogether. In these and other ways, cuffless BP measurement can improve the assessment of BP and thereby mitigate the devastating burden of elevated and low BP.

A challenge is the unique difficulties in validation of such devices, which is not addressed by existing standards and guidelines for cuff-based BP measuring devices. The first technical standard for cuffless BP sensors was published in 2014 and amended in 2019 ("IEEE Standard for Wearable Cuffless Blood Pressure Measuring Devices," 2014). Very recently, the European Society of Hypertension released their first recommendations for validating cuffless BP devices (Stergiou et al., 2023), demonstrating the rapidly maturing state of the field while pulling attention to areas of lacking understanding in current approaches, such as non-resting state conditions.

While there are significant differences in technical details and implementation, cuffless BP estimation depends on a small number of fundamental techniques, implemented using different sensor types. Here, we will briefly review two of the major approaches – pulse wave velocity (PWV) and pulse wave analysis (PWA) – before reviewing commonly used sensors and their uses in the current literature.

2.2 Timing intervals and pulse wave analysis

A common application of many of the sensors described thus far in a longitudinal context is derivation of timing metrics. Heart rate is the most obvious, many applications also attempt to extract the respiratory rate. But by combining more than one sensor we can compare fiducial points in the recorded signals to determine timing intervals between events in different parts of the cardiovascular system.

One of the most popularly investigated is the pulse transit time (PTT). Ejection of blood from the left ventricle creates a pressure wave moving through the arterial tree. This wave moves significantly faster than the blood itself and can be recorded at different locations as it transits.

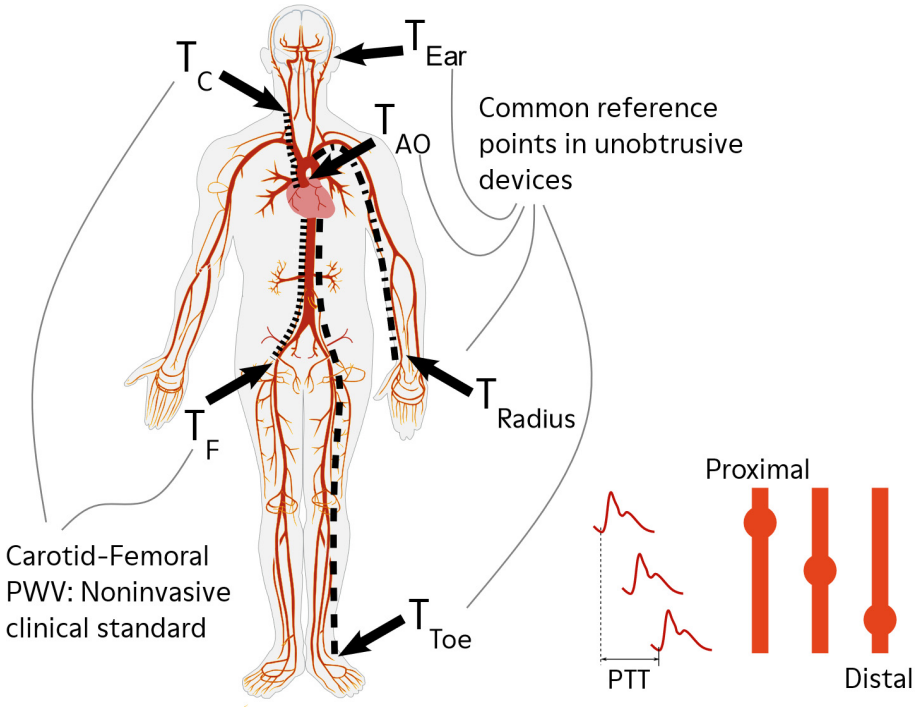

Figure 9. Illustration of the principle of PTT measurement, along with common reference points.

As the PTT is the time difference between a proximal (closer to the origin) and distal (farther) site, it is the inverse of the pulse wave velocity (PWV). Figure 9 illustrates this concept.

The relationship between PWV and the incremental elastic modulus ("stiffness") of the arterial wall, E_{inc}, the blood density ρ and the vessel radius and wall thickness r and h is modeled in the Moens-Korteweg equation:

$$PWV = \sqrt{\frac{E_{inc}h}{2r\rho}} \quad (1)$$

This proportional relationship means PWV is often used as a non-invasive measurement of arterial stiffness. Arterial stiffness is itself valuable as an index of vascular aging and the development of age-induced arteriosclerosis (Cecelja & Chowienczyk, 2009; Nichols et al., 2011). Outside the aorta, arterial stiffness is also largely affected by contraction and relaxation of arterial smooth muscle, i.e., autonomous regulation of the peripheral vascular resistance. There is initial evidence

to suggest that PTT can be a marker of hypovolemia distinguishable from autonomic pain responses, presenting possible clinical monitoring applications in e.g. postoperative observation (Djupedal et al., 2022).

The idea of using pulse transit time as an indicator of blood pressure has been suggested for a long time (Geddes et al., 1981), but it has increasingly become seen as the only theoretically sound correlate of blood pressure that can be practically recorded. E_{inc} increases with increasing BP due to the material properties of the arterial wall. This has led to many recent applications of PTT in unobtrusive continuous BP estimation (Barvik et al., 2022; Ganti et al., 2021; Mukkamala et al., 2015, 2022). Generally, PTT decreases with higher BP as, stiffness of the arterial wall increases with BP. The specific relationship between BP and stiffness is complex, and dependent on the selection of a material model for the vessel wall. There are several alternatives, resulting in a number of theoretically derived models relating BP to PTT (Finnegan et al., 2021). As stiffness is also affected by age, PWV based models often attempt to correct for age effects.

The typical method of measuring PTT is to record the onset of a pulse wave at two different locations along the artery and calculate the time difference, as shown in Figure 9.
PTT recorded in the descending aorta is ideally desired for arterial stiffness studies, and carotid-femoral transit time is considered the clinical standard (cfPWV). CfPWV is typically recorded with two applanation tonometers either simultaneously or referenced to the electrocardiogram (ECG). This approach is not convenient for longitudinal monitoring. The methods of recording PTT commonly encountered in this space rely on recording the arrival of a pulse wave at two locations along the same artery. This can be done by, for example, recording the onset of a photoplethysmogram (PPG) or impedance plethysmogram (IPG) wave at two relatively closely spaced locations along a peripheral artery. However, as the pulse wave moves fast, on the scale of 6-10 m/s, the closer the two measurement sites are the higher the sample rate necessary to record the PTT. A different approach is by recording a peripheral pulse wave and estimating the time of AVO from peripherally recorded signals, as will be discussed further on.

Note that the arterial pathway in which PWV is measured is not the same in all measurements. Wrist based measurements for example record pulse transmission in the peripheral arteries of the

Table I. Body worn sensor locations for unobtrusive CV monitoring

Body location	Social acceptance	Technical maturity	Selected applications
Sternum	Medium	High	PEP (ECG / SCG), SV (SCG), BP (SCG / PPG PWA), Arrythmia (ECG)
Wrist (**smartwatch**)	Very high	High	PTT (BCG / PCG), BP (PWA). SV? (BCG), Arrythmia (ECG)
Upper arm	Medium	High	PTT (IPG)
Finger (**ring**)	Medium	Moderate	PTT (IPG), BP (PWA)
Face	Low	Low	PTT (PPG / BCG)
Ear	High	Moderate	PTT (PPG / Acoustic + BCG)
Feet	Uncertain	Moderate	PTT (PPG + BCG), SV? (BCG)

Social acceptability based on recommendations of Zeagler, 2017. Technical maturity is the author's assessment based on state of current research and OEM adoption. HR monitoring not included.

arm. In order to improve performance of PTT models, it has been suggested to focus research on PWV primarily in the descending aorta (Mukkamala et al., 2022). This might motivate PTT measurements via the feet or seated measurements. Table I includes suggestions for wearable locations.

A related measure is the Pulse Arrival Time (PAT), which is the time from the ECG R-peak to pulse wave arrival at the distal measurement site. The QRS complex in the normal ECG represents atrial depolarization, signifying the onset of the electromechanical systole. The PAT therefore also contains the duration of isovolumic contraction, the Pre-Ejection Period (PEP):

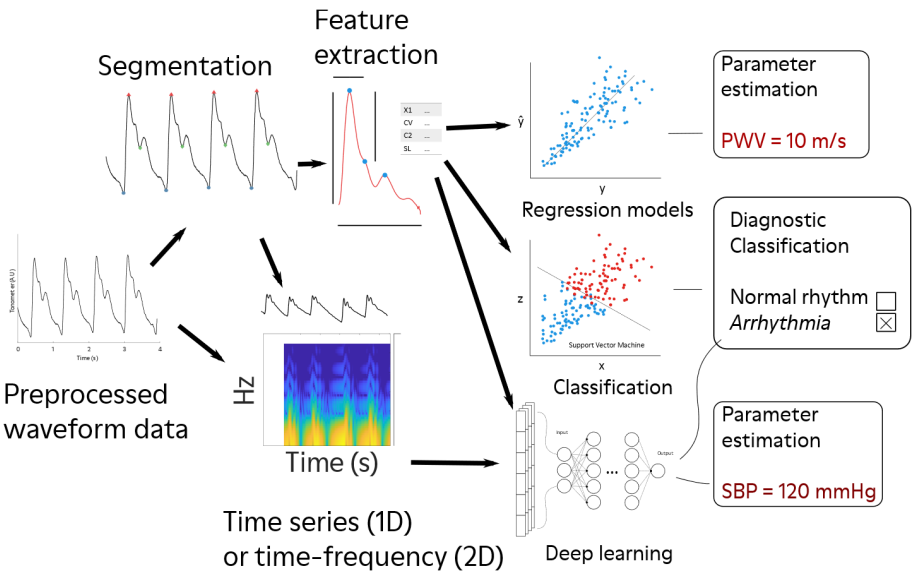

Figure 10. Overview of typical applications of CV signals in the literature. Based on Charlton et al., 2022.

$$PAT = PTT + PEP \tag{2}$$

As a measure of cardiac contractility, PEP is of interest in its own right. Due to the relative reliability and sharply defined QRS features of ECG signals, PAT has commonly been used as a proxy for PWV and in studies of BP estimation, although the inclusion of PEP means that it is not a true measure of PWV. There remains some disagreement on its interchangeability with PTT in this context (see e.g. W. Chen et al., 2000; Finnegan et al., 2021; Heimark et al., 2022; Martin et al., 2016; Zhang et al., 2011).

Beyond PTT, the second method of BP estimation attempts to estimate BP or other clinically relevant hemodynamic parameters – again often related to estimating vascular aging – via empirical modeling. Such approaches typically rely on either pulse wave analysis (PWA), or deep learning approaches which can ingest continuous heartbeat sequences. Figure 10 illustrates typical applications of this approach.

PWA is the analysis of the morphology of the pulse wave in question. Techniques range from simple geometrical features of the timeseries data to complex theories such as wave separation and

impedance analysis, which involves combining pressure or PPG waves with blood flow velocity curves obtained experimentally (or alternatively estimated using population based models as this data is rarely available (Alastruey et al., 2023)).

Certain PWA-derived metrics are discussed in chapter 4. Output of PWA is used as features in regression or classification models, or in deep learning applications. Such "Black box" models are discussed in greater detail in chapter 4.

2.3 Important sensor types and their application

Improvements over the past few decades in miniaturization, production technology, and processing techniques, not to mention battery and power management technology, have vastly improved the practicality of small sensor circuits suitable for implementation in wearable formats. There are four fundamental sensing principles used in this space: electrical, optical, and force/pressure. Each of these fundamental principles has been applied in various applications, and each is capable of probing different aspects of the peripheral CV system. Of these, the most relevant are electrical, optical, and force systems. Figure 11 shows portions of several CV signals that will be discussed and their rough temporal relationship. The definition of the PTT, PAT, and PEP are shown.

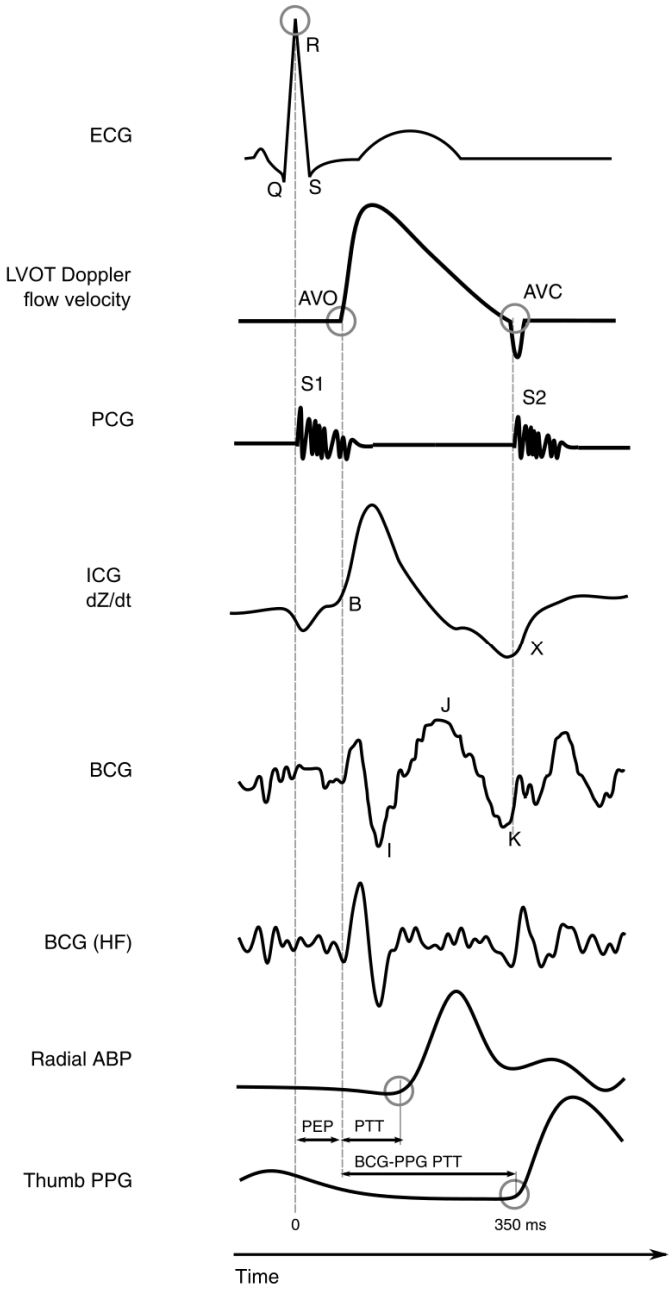

Figure 11. Diagram of different CV measurements and their temporal relation to the systolic intervals. ECG: electrocardiogram, LVOT: left ventricle outflow tract, ICG: impedance cardiogram, BCG: acceleration ballistocardiogram, BCG HF: high-pass BCG, PCG: phonocardiogram, ABP: arterial blood pressure, PPG: photoplethysmogram.

2.3.1 Optical

Photoplethysmography (PPG) is the observed effect that the optical absorption of light in well-perfused tissues varies in time with the cardiac rhythm (Charlton et al., 2022). The signal recorded in this way varies slightly but significantly with the wavelength of the light, and has been used extensively in medical devices for estimating oxygen saturation in the peripheral vasculature etc. (Allen, 2007). PPG is the predominant method of recording heart rate in wearables, due to the small footprint, low cost, and technical maturity of modern PPG sensors (Charlton et al., 2022; Charlton & Marozas, 2022).

The PPG signal consists of a rapid deflection followed by a slower decline, in which a second peak and dicrotic notch may or may not be visible, corresponding to systolic and diastolic portions of the cardiac cycle. Beyond oxygen saturation, typical wearable applications include deriving HR and respiratory rate (Charlton et al., 2017), with interest in estimating BP.

BP estimation techniques involving the use of PPG can be divided into black-box modeling approaches and physiology or physics-based approaches. In black-box models, large feature sets such as time-frequency representations (e.g. spectrograms, scalograms, or other image-type representations) are derived from PPG pulse trains and are then used to train neural network models (see e.g. Kurylyak et al., 2013; Leitner et al., 2022; Wang et al., 2022).

Physics based approaches will either be based on calibrated PTT models, or via the principle of controlled volume: by compressing the tissue while recording the PPG the sudden cessation of the pulsatile portion of the PPG denotes when the external pressure has overcome the internal arterial pressure. This principle is used together with an oscillometric cuff in the volume-clamp method found in the Finapres device to continuously measure BP noninvasively with the help of a high-frequency pneumatic servo pump and is commonly used in research. More recently it has been investigated for on-the-go pressure measurement using consumer devices such as smartphones by having the user press a finger against a surface containing a PPG sensor while increasing the pressure (Mukkamala et al., 2022). It has been demonstrated that contact pressure between the skin and the sensor affects the shape of the waveform, particularly, by delaying the onset or the

foot of the PPG wave. This has notable effects on estimation of PAT and PTT measurements (Chandrasekhar et al., 2020).

Given the wide adoption of PPG in both consumer wearables and clinical diagnostic devices it is remarkable to note that the origin of the signal is not clearly understood. As PPG has matured and become commonplace in clinical use, designers have become particularly interested in other applications of the signal beyond oximetry and heart rate estimation, raising the question of what other mechanisms are involved in the generation of the shape of the waveform. According to Kyriacou & Chatterjee (2022):

> The global acceptance of pulse oximeters in a way has diminished and somewhat overshadowed progress toward further fundamental PPG research. The need for such research has again gained momentum in the recent past where research endeavors were made to extend the application of PPG beyond pulse oximetry, especially for the PPG-based wearable technologies, and hence the simple question was raised again: "Where is the PPG signal coming from?"

What is known is that the shape of the observed waveform is the result of several complex physiological interactions between the local vasculature and the surrounding tissues. More practically, the effects of differences in skin tone has been a recurrent concern, the mitigation of which is a topic of ongoing research (Fine et al., 2021; Nowara et al., 2020).

2.3.2 Electrocardiography

Electrical biosensing can be divided into passive and active sensing methods. In the passive configuration, a time-varying electrical potential is recorded across two or more locations on the skin. Depending on the placement of the electrodes, this method can be used to record several different signals: the depolarization and repolarization signals traveling outwards from the sinoatrial node in the heart, resulting in the electrocardiogram (ECG) in its many forms, the electromyogram originating with the electrical activity of the skeletal muscles, the electrical activity of the brain in the electroencephalogram, or the local variance in skin resistance resulting from sweat gland activity, in the form of electrodermal activity, et cetera.

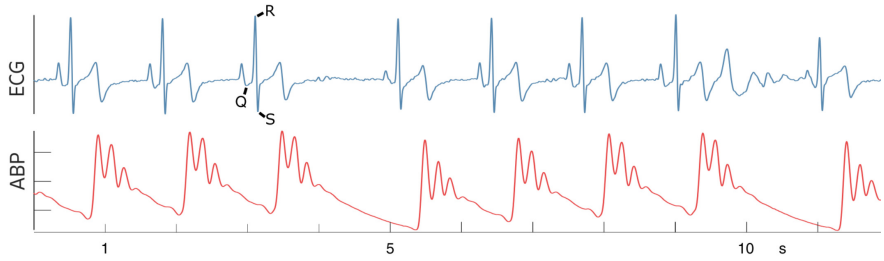

Figure 12. A sequence of ECG and ABP signals.

Figure 12 shows an ECG sequence together with radial ABP, recorded from a female volunteer (see chapter 4). The morphology of the ECG depends on the arrangement of the electrodes, but in most configurations the normal ECG is characterized by a "spiky" sequence of deflections called the QRS complex. The distinctive R peak is commonly used in wearable applications of ECG as an easy-to-detect reference for the beginning of systole. In this sequence, we can also see "dropped" heartbeats around 4 and 10 seconds. While other types of CV signals, like the invasive BP waveform, will show the missing systole, the ECG is supremely useful for analysis of the cardiac timing system and provides more information for classifying arrhythmias.

The ECG is a highly important signal modality, primarily in the clinical setting, where affordable and reliable devices for wearable monitoring have become available. Clinical wearable ECG systems have been demonstrated to be no less capable of detecting arrhythmia compared to current standard of care, the 12-lead ECG (Bouzid et al., 2022; Kamga et al., 2022). As perhaps the most mature wearable CV monitoring technology with direct clinical relevance, consumer level wearable ECG is currently confronting difficult questions on how data from such devices can be integrated into existing healthcare infrastructures (Isakadze & Martin, 2020; Sana et al., 2020).

Beyond its status as the clear benchmark for arrhythmia and heart rate analyses, the ECG is highly useful for many CV applications as a reliable timing reference that is relatively robust against artifacts. It is also relatively simple to record. ECG is often used in wearable studies involving other sensing modalities as a robust timing reference, which is highly useful for some signal processing applications, and is therefore often recorded alongside sensor devices that, in an out-of-lab

environment would likely not have access to ECG. The main downside of the ECG for unobtrusive recording is the need to have reference contact points across the heart. In the most common applications this is achieved via chest contacts or by touching the opposite hand to an electrically isolated part of a smartwatch.

2.3.3 Bioimpedance

The active counterpart to passive electrical biosignals is the measurement of bioimpedance, or bio-Z. In a physical system, if resistance is the opposition to a constant flow at a constant potential, the impedance of the system is the opposition to flow with a time-varying component. In the context of an electrical circuit, we can say that the impedance of the system is the expansion of resistance to a non-steady state.[1]

Measuring bioimpedance relies on applying an external alternating current between two parts of the body and measuring the time-varying change in opposition to the changing current, having both a magnitude Z and phase, ϑ. A problem in bioimpedance measurement is selecting an appropriate AC drive frequency for the specific application.

In the context of CV monitoring bioimpedance is primarily valuable for its ability to record fluid movement, as the impedance between two measurement locations varies with the volume fraction of water between the two measurement sites. One application of this principle is impedance cardiography (ICG), based on impedance in the thorax. As the large bodies of blood in the thorax move over the cardiac cycle, a characteristic change in impedance magnitude can be recorded corresponding to this difference. Alongside heart rate and respiration rate, ICG has been used to estimate SV and to detect the onset of ejection to record PEP together with ECG, although SV estimation has been reported to be unreliable by some authors (Borzage et al., 2017; Malmivuo & Plonsey, 1995).

[1] As an amusing aside, physical impedance experienced by fluids moving in a closed system is central to mechanical models of the vascular system as the coupling between the heart and the vasculature. These models often use equivalent electrical circuits to equate the flow of blood with the flow of electrical current. Simultaneously, the so-called "hydraulic analogy" of electricity is a commonly used analogy for teaching electrical theory by equating electrical flows to the flow of fluid in a closed system.

In the wearable context, bioimpedance has been used to record pulse waveforms (IPG waves) in the distal limbs with an aim towards continuous BP estimation (Kireev et al., 2022; Sel et al., 2023). Intuitively, given the relationship between bioimpedance and local fluid volume, an expectation would be that the waveform should record a similar signal to the PPG, but perhaps without the confounding factors associated with PPG waveform synthesis (Kyriacou & Chatterjee, 2022), and this does appear to be the case. An insightful comparison of PPG and BioZ waveforms across a range of user skin tone scales – a recurring concern in PPG based devices (Nowara et al., 2020) – seemed to imply less variation of the IPG signal with skin tone (Sel et al., 2023). For BP estimation, aside from the different principles from which the waveform is derived, the processing techniques and estimation approaches are thus otherwise in line with previous work on peripheral PPG.

The wide use of wearable impedance cardiography wearables is likely some distance out, but results like these seem quite promising. The same problem remains as with other bioelectrical sensor modes, namely, the quality of the electrode-skin interface. This is a rapidly developing field, however, and advances in dry electrodes could be a boon to development of this technique (Fu et al., 2020; Kireev et al., 2022; Ma & Soin, 2022).

2.3.4 Arterial tonometry

Tonometry is the recording of pressure by means of directly applying to pressure transducer to a site of interest. In CV monitoring, this is typically the skin above an artery. Tonometry is typically done by a trained operator applying a pen-like device with a pressure sensitive element at the end to an artery, typically the radial, femoral, or the subclavian.

The benefit of tonometry is that when applied correctly, the pressure sensing elements compress the radial artery against the underlying radius bone, theoretically eliminating most factors effecting the transmission of the pressure wave and thus recording a true representation of the intramural pressure of the artery. This concept is usually referred to as applanation tonometry, as the artery is flattened or applanated (Figure 13).

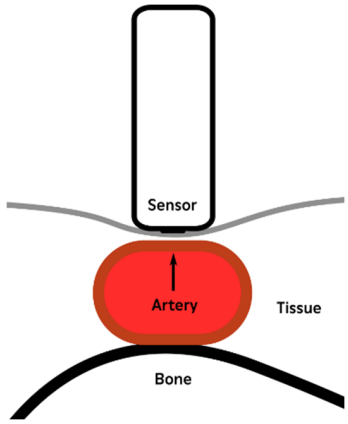

Figure 13. Conceptual schematic of applanation tonometry (not to scale). By squishing the artery flat against the underlying radius bone, tangential forces in the lumen are eliminated and the transmural pressure becomes equal to the intramural pressure. While complete applanation is the goal in traditional tonometry, it is rarely achieved in modern device concepts owing to the difficulty of compressing the artery accurately, as well as user discomfort when wearing plunger-style sensors over long periods.

Use of peripheral tonometry in the past two decades was primarily driven by the derivation of mathematical functions that estimate the shape of the central aortic pressure wave from that collected peripherally at the radial artery. Several such functions, termed transfer functions, have been described. The most well-known are the population averaged generalized transfer functions (C. H. Chen et al., 1997; Fetics et al., 1999; Karamanoglu et al., 1993). A clinically validated variant of these is used in the SphygmoCor tonometer, and has been validated at rest (Gallagher et al., 2004) and investigated during mild exercise (Sharman et al., 2006; Stok et al., 2006, 2011). More recent developments include attempts to derive adaptive transfer functions (Gao et al., 2016; Stok et al., 2011), as well as the notion that a simple N-point moving average filter might be sufficient to accurately estimate systolic and diastolic aortic pressures from a calibrated tonometric waveform (Shih et al., 2014; Williams et al., 2011; Xiao et al., 2018).

Being able to estimate the shape of the central aortic pressure was highly valuable to cardiovascular researchers as it directly influences the action of the left ventricle (Davies & Struthers, 2003), but there are limitations to the use of derived aortic pressure waves in longitudinal monitoring as transfer functions validated at rest have not been extensively validated or otherwise in conditions out of rest. They also rely on the assumption of complete applanation.

The development of accurate and inexpensive MEMS pressure sensors have renewed interest in wearable tonometry. Commercial devices have existed for some time, older devices have relied typically on plunger-style force probes with single points of measurement, typically leading to devices that, while accurate, have been uncomfortable and reliant on very precise placement. The small footprint and high sensitivity in the relevant pressure domain of modern capacitive sensors has led to applications in which several sensing nodes have been arranged at regular intervals, increasing the usable area (Kaisti et al., 2019; Mieloszyk et al., 2022; Solberg et al., 2019; Steffensen et al., 2023). These devices typically consist of an array of pressure sensing elements bonded to a solid or flexible PCB, on top of which is deposited a rubbery skin-safe material like PDMS to provide a compliant interface between the skin and the pressure sensors. The shape of the interface layer varies significantly between devices, from hemispherical domes covering individual sensor elements, to square pads covering the entire grid area, to more complicated structures intended to shape the force propagation towards the sensing elements.

Wearable tonometry applications cannot rely on an experienced operator or correct applanation, in pressure pad-type wearable tonometry this will typically not be the case. As such, there will be an unknown contribution to the shape of the recorded wave from transmission effects through the tissue between the lumen and the surface of the skin as well as through the interface layer. These contributions are significant to attempts to create mechanical models or calibration techniques to relate the recorded signal directly to the internal blood pressure (Choudhury et al., 2018; Shimura et al., 2018; Singh et al., 2017). These are so far not very successful. Wearable tonometric data is therefore more typically used to estimate BP via a posteriori regression modeling. In these applications, particular relevant features from the time or frequency domain are extracted from the waveform signal, much in the same way as a PPG signal would be.

2.3.5 Force ballistocardiography

The ejection of blood into the aorta results in a reaction force through the body as the center of mass of the thorax subtly changes. If recorded over time this force yields the ballistocardiogram (BCG). As a record of the mechanical action of the heart, BCG saw significant research efforts around the middle of the 20th century but was largely abandoned due to the cumbersome equipment necessary and the advent of echocardiography. In the past decade and a half, it has been

picked up again as modern sensor and microprocessor technology has made the BCG more convenient to record, and as interest in convenient, noninvasive CV monitoring has grown.

As a force signal, the BCG can be recorded via force plates or load cells such as those found in home weigh scales (Campo et al., 2017; Inan et al., 2009), via pneumatic pressure sensors used as under mattress inlays (Rosales et al., 2017; Su et al., 2019), smart chairs, toilet seats, and numerous other scenarios where the "weight" of the body can be recorded over time at a relatively high sample rate. A clear application has been non-contact HR and respiratory monitoring in bedside situations, such as in hospitals (Jung et al., 2021, 2022) or in extended care facilities such as nursing homes (Enayati, 2019; Lydon et al., 2015). Several products are commercially available for this purpose (e.g., Withings Sleep, Withings, France).

As the signal is generated by the action of the heart, there is rich information on the mechanical performance of the CV system. The association between the amplitude and duration of the main systolic complex of the BCG, the so-called IJK complex, with stroke volume has long been noted (Starr, 1955; Starr et al., 1939). Unfortunately, the BCG is observed to vary significantly between individuals, making consistent identification of morphological features challenging. This is hypothesized to be largely due to natural individual variations in anatomy. The origin of the BCG waveform remains poorly understood, and mathematical modeling of the BCG is an ongoing endeavor (Marazzi et al., 2022).

An application of the BCG morphology that has been demonstrated repeatedly is the ability to use the initial energetic deflection of the systolic complex (the I-wave) as a stand-in for aortic valve opening. As a force that moves through the gross structures of the body, the BCG vibration signal travels very rapidly (at the local speed of sound), and it can therefore be used as a distal proxy for central AVO (Campo et al., 2017; Inan et al., 2015; Kim et al., 2015; Mukkamala et al., 2015, 2022). This principle is applied in smart bathroom weigh scales, toilet seats et.c. for estimating arterial stiffness. Example recordings from a lightly modified (wires were soldered onto the transducer amplifier to directly record output from the transducer.) commercially available BCG device is shown in Figure 14.

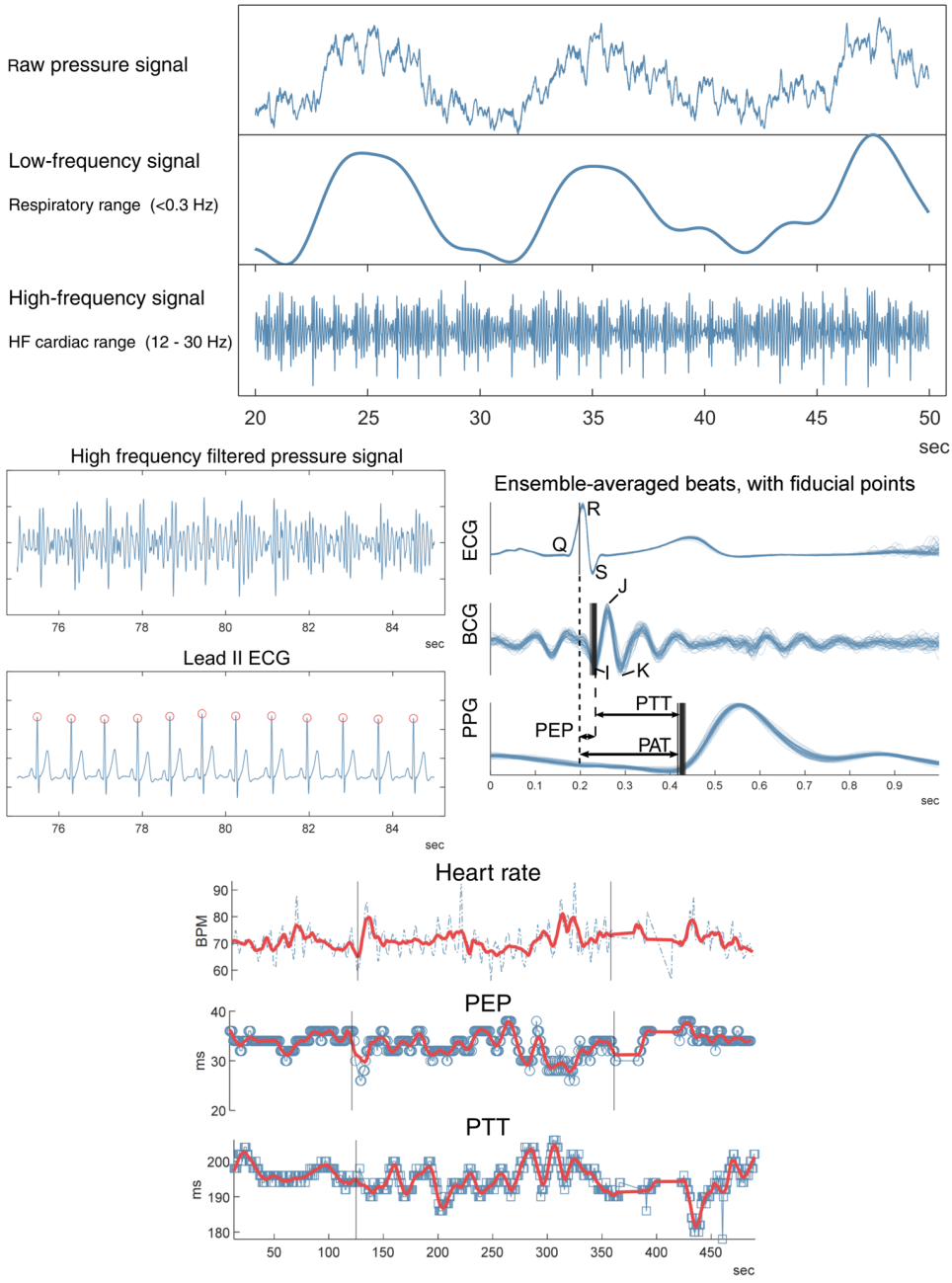

Figure 14. Force BCG data recorded with a modified commercial pneumatic under-mattress sensor (Withings Sleep). Starting top left, the raw signal is filtered to extract respiratory and cardiac frequency signals. Using a second sensor modality, here ECG, sequential beats are segmented and averaged. This allows moving average estimation of PEP and PTT.

Figure 14 demonstrates recording of PEP and PTT by combining an under-mattress pneumatic sensor, a fingertip PPG sensor, and chest pad ECG. Given the proportionality of peripheral PTT with BP, tracking trends this way offers possibilities for early detection of the onset of hypotension in patients in post-surgical recovery, or for signs of hypovolemia (Djupedal et al., 2022).

Wearable force BCG requires the sensor to be placed in a location where the force of the body can be detected while moving. In contribution 1, we presented a sensorised insole to record the force BCG using fluid-filled pneumatic sensors and atmospheric pressure sensors (Gjerde et al., 2022). Volunteers undertook a cold pressor test, increasing peripheral resistance and SBP, which should result in a decrease in PTT, recorded via finger PPG (future devices should consider implementing ankle PPG, to record the central aortic PTT, and consolidate monitoring at a single location). We observed a decrease in PTT and a simultaneous increase in SBP recorded using a volume-clamp device (ADInstruments NIBP).

While the signals recorded from the pads were noisy and of fairly low quality, they did record a signal that was broadly similar to a reference weigh-scale based device, demonstrating potential.

2.3.6 Acceleration ballistocardiography

The same mechanical action that generates the force BCG also results in physical motion in the body. This effect is sometimes not distinguished from the force BCG, or conflated with a related measure, seismocardiography (SCG). We will refer to it here as acceleration BCG. The total movement induced by the acceleration is also sometimes used, termed the displacement BCG.

For sake of clarity, we will consider SCG as a special case of acceleration BCG, worthy of its own discussion. SCG is the record of cardiogenic vibrations at the chest wall. It has been noted to be relatively easy to record and to contain rich information about the mechanical action of the heart. In addition to the unsurprising ability of the SCG to detect heart rate, it appears to be quite capable in accurately denoting AO (Inan et al., 2015; Sørensen et al., 2018). More interestingly SCG signals have been shown to have predictive capability for cardiac hemodynamics that may be of direct clinical relevance (Hoffmann et al., 2022; Shandhi et al., 2022) (for an analysis of triaxial acceleration measured directly in the wall of the heart itself, see for instance Krogh et al., 2021). The implementation of SCG is typically in the form of a chest-strap, or otherwise a device

attached to the chest wall using a contact adhesive, typically also used to record ECG. As the SCG signal is recorded close to the heart, it is not capable of recording the PWV, but eminently able to record the duration of PEP and left ventricle ejection time (LVET) when used in combination with ECG.

Wearable SCG has been used to estimate a number of CV parameters of interest, including blood pressure, left ventricular stroke volume and oxygen uptake (Ashouri et al., 2018; Etemadi & Inan, 2018; Shandhi et al., 2021). As the generation of the BCG and SCG signals remains unclear and modeling efforts are ongoing (Marazzi et al., 2022), these parameters tend to be estimated using feature sets without clear theoretical relationships to physiological phenomena. They nevertheless seem effective in intra-individual models, indicating predictive capability.

The primary weakness of SCG remains the use of a chest-worn device which must be precisely located on the sternum, which limits user acceptance (Table I, Gemperle et al., 1998; Zeagler, 2017).

Recording acceleration BCG at the wrist is motivated by the presence of accelerometers in all modern smartwatches, usually together with PPG. Remarkably, wrist BCG has been demonstrated to be able to track AVO at rest, which has been examined with an eye to BP estimation via PTT (Shin et al., 2021, 2022; Wiens et al., 2017; Yousefian et al., 2019, 2020). However, these signals are extraordinarily noisy, and typically cannot be used on their own, requiring a secondary, more robust signal to reference for creating ensemble averages in order to improve SNR.

PTT estimation from wrist BCG during exercise has been demonstrated in contribution 3 of this thesis (Steffensen et al., 2023), counterintuitively suggesting that recording AVO might become easier with increasing HR as SV increases the amplitude of the systolic complex.

2.3.7 Acoustics

After noting the use of acceleration signals recorded at the wrist to capture signals in the 1-100 Hz range, it is interesting to note that at least one device has been demonstrated to record acoustic-frequency (~ 2 KHz) CV signals at the radial artery (Sharma et al., 2019; Sharma & Rodriguez-

Villegas, 2021). The authors report success in recording heart rate using passive contact microphones recording from the radial artery at the wrist. Unfortunately, as the authors' comparator PPG signal was not synchronized, it is difficult to assess the use of this technique for timing interval assessment as it is unclear if the recorded sound corresponds temporally to the first heart sound of the PCG. In such an event, a hypothetical device could be envisioned in which the closing of the mitral valve – and the onset of the first heart sound – can be detected using the high-frequency wrist PCG, the opening of the aortic valve via wrist BCG, and the arrival of the pulse wave at the distal site via PPG or tonometry, allowing longitudinal recording of PEP and PTT at a single point, without requiring an ECG signal. A further advantage of such a device lies in noting that the authors report a signal with a sharply delineated onset, potentially making it more suitable for segmentation tasks than PPG, which has a smooth morphology.

Away from the wrist, there are notable ongoing developments using low-frequency microphones to record cardiogenic pressure variations in the ear, a technique that has been referred to as infrasonic hemodynography (Gilliam et al., 2022; Park et al., 2015; Wheeler et al., 2021). The goal is to record BP directly via smart earbuds ("hearables"). This is an area of ongoing research seeing rapid development.

Lastly, there are several efforts to develop wearable ultrasound devices to record e.g. blood flow velocity (Hu et al., 2023; C. Wang et al., 2022). These efforts are highly interesting, but while leading developments are being made in probe design, the electronics these probes currently need to be interfaced to are not yet near fulfilling the aspirations of being ubiquitous or unobtrusive. This field has tremendous potential, and developments in miniaturization and probe design should be followed.

2.4 Some points on cardiovascular signal processing

The sensor methods discussed above, when applied to cardiovascular monitoring, yield time series that vary due to the action of the cardiovascular system. Due to the repeating, continuous action of the heart, we conceptualize these signals as waves, and talk of them as different *waveforms*. There

are crucial differences between these signals due to the different mechanisms that generate them, but many of the methods of processing and analysis are similar.

The goal in CV signal analysis is normally either diagnostic categorization (e.g., hypertensive, young/old, et.c.) or parameter estimation (HR / RR, PWV, AI, BP et.c.). The data processing pipeline in each situation will reflect the goal of the analysis, but typically starts out with preprocessing to remove high frequency measurement noise and perhaps low-frequency drift or motion artifacts, depending on the measurement setup.

2.4.1 Quality indexes

Due to the nature of wearable measurement, signal quality is often disrupted by motion artifacts or loss of skin contact. If the goal is longitudinal measurement and/or further processing techniques rely on ensemble averaging, a common problem is accepting or rejecting sequences of waveforms. This is typically done by applying some form of quantifiable metric of beat "quality". Common methods are based on measures of signal-to-noise ratio, signal entropy, or temporal autocorrelation, either with the signal itself or with a referent signal. Quality indices are commonly combined in practice and will often include some "common sense" metrics such as beat duration and signal amplitude (Orphanidou et al., 2015).

Figure 15 shows an example of a series of pulses recorded with a tonometer. An algorithm (Alexandre Laurin & Jona Joachim, 2017) has been used to identify the onset of candidate beats. The series includes two areas of motion artifacts resulting in corrupted signals. As we are often interested in analyzing individual beats in future processing steps, either sequentially or as ensemble averages, the goal of the beat quality assessment is to accept or reject the identified candidate beats. In this illustration, a sliding window template autocorrelation assessment is used to assign a value between -1 and 1 to each candidate beat. A threshold for acceptance, for example Pearson's $\rho > 0.8$, will typically be set empirically by weighing tolerance of poor quality beats against the need for available data.

One longitudinal study of wearable tonometry, ECG, and PPG in 548 participants over a rough 24 hour period reported an average signal "availability", reported as fraction of successful measurement attempts, of between 0.4 and 0.6 for tonometry, compared with 0.4 - 0.9 for PPG

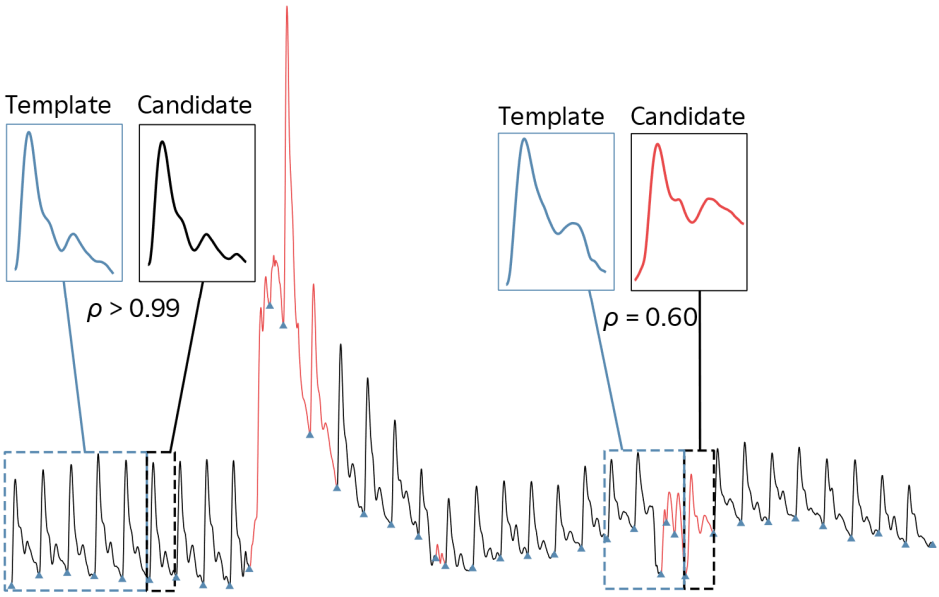

Figure 15. Quality assessment using a sliding template matching method. The blue triangles are tentatively identified systolic feet used to segment individual beats. Red sections are rejected. A template consisting of the mean signal of N previous beats is compared to the next candidate beat via cross-correlation. If the correlation coefficient is below a threshold, the candidate beat is rejected. Autocorrelation is typically used together with "sanity check" markers such as a realistic beat length. While the templating window may include low quality beats, typical problems like motion artifacts are noisy and chaotic, resulting in a poor correlation between subsequent low-quality beats as well. There are several autocorrelation techniques, with or without dynamically adaptive thresholds. Data from the study described in Steffensen, 2023 and chapter 4.

and above 95% for ECG (Mieloszyk et al., 2022). It should be noted that this fraction includes failure due to device removal etc. alongside poor signal quality. Other reported results from similar population sizes and comparable devices are rare, but the reported range seems in line with anecdotal evidence. Notably, the authors found that while tonometry data was less available than PPG during sleep, the two modalities were broadly comparable during daily activity.

2.4.2 Filtering, segmentation, and decomposition

There are both natural and sensor-induced variation in cardiovascular signals. There are low-frequency fluctuations induced by the respiratory cycle, at around 0.1 to 0.3 Hz, as well as Mayer waves, a roughly 0.1 Hz fluctuation caused by the body's various systems for regulating blood

pressure (Julien, 2006; Nichols et al., 2011). Sensors have some level of inherent measurement noise, and sudden motions can influence our readings by adding rapid transients.

For this reason, waveform data is almost always lowpass filtered. Any number of filtering approaches are in common use, both analog and digital. The passband of interest changes with the application and sensor type – rapidly fluctuating features in the ECG can be very important, while BP waveform data rarely contains interesting information above 30 Hz (see for example Figure 20).

BCG and SCG data are special cases. As typical applications rely on accelerometers with relatively low SNR these measurements can be very noisy. Dedicated filtering approaches have been suggested depending on the intended use case of the signal (Yao et al., 2022).

Sometimes, even after filtering, physiological mechanisms can cause differences in the signal we are interested in. For example, if we want to avoid the amplitude oscillation caused by respiration, we can look at the average wave over a longer period, for example 5-10 beats. These *ensemble averages* are also highly useful in the case of highly noise-influenced or weak signals, such as can be the case with BCG and SCG.

The first step of obtaining the ensemble average is to identify a clear reference point in the signal of interest. Depending on the signal, this will typically be the systolic peak or the foot of the systolic rise. Identifying these points is of large interest in algorithms for determining heart rate, and there are various approaches available with specific adaptations for particular signal types (e.g., Alexandre Laurin & Jona Joachim, 2017; Charlton et al., 2016; Lin et al., 2018; Pan & Tompkins, 1985). Several approaches are then available: the simplest approach is to select a window of samples before and after the identified point. This approach simplifies dealing with the end effects induced by variable length of individual beats and is popular where the resulting signals are used in machine learning approaches requiring constant frame size (see e.g. Shandhi et al., 2022). Another option is foot-to-foot or peak-to-peak, which require a strategy for dealing with end effects, such as cutting to uniform length, padding, or using normalized time windows (e.g. Sel et al., 2023). Both approaches are made difficult in situations involving variation in heart rate, such as free living or exercise studies.

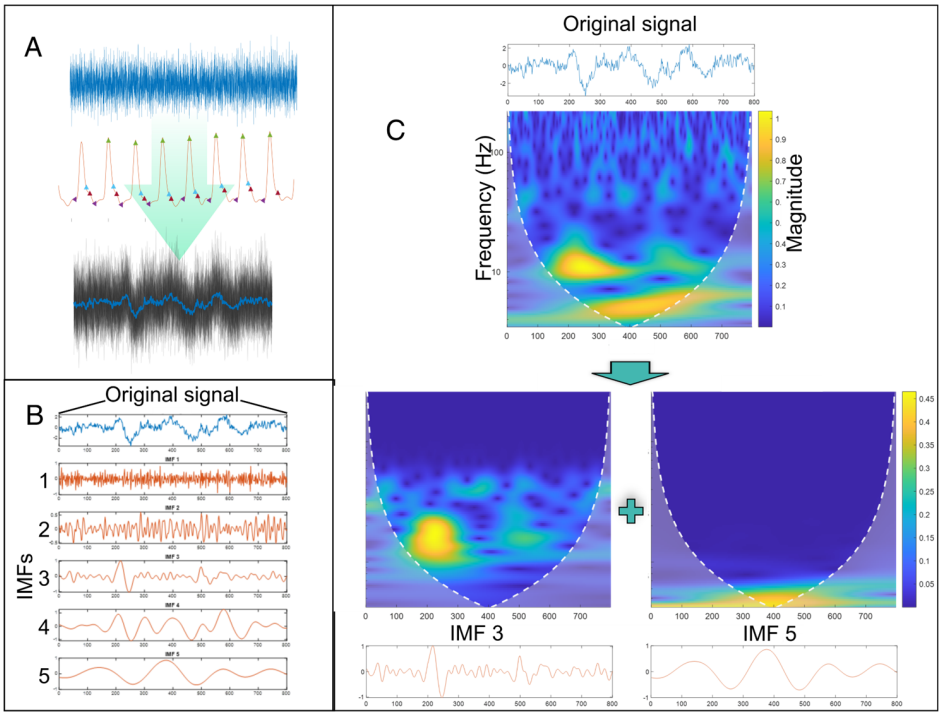

Figure 16. Signal decomposition via EEMD of wrist BCG. A: raw accelerometer data is segmented using a reference waveform signal. B: the ensembled signal is decomposed into several basis functions using the EEMD algorithm. C: wavelet scalograms of the original signal (top) and two of the basis functions, demonstrating the ability of the algorithm to isolate the two main energetic features. Adapted from illustrations used in Steffensen et al., 2023.

Once the sequence of beats has been thus segmented, the average is creating by taking the average value of several beats for each timepoint, resulting in an averaged waveform. It is important to be aware of the assumption of relatively steady state signals over the averaging period if the averaged beat is intended for further analysis.

2.4.2.1 Decompositions

As noted, BCG signals can be particularly challenging to deal with in a wearable scenario due to the very high level of noise that can be present. In addition, the BCG is notably variable between persons, and we are often interested in particular features, which makes specifying filter passbands difficult. One approach is to fit personalized passbands to each participant (Wiens et al., 2017), but this requires a posteriori knowledge.

Another approach to isolating accelerometry signals of interest is signal decomposition. Decomposition is the process of iteratively creating partial functions that can be linearly combined to recreate the original signal. The classic example is the Fourier decomposition, in which a continuous signal is represented as a sum of simple sine waves. In applications dealing with noisy BCG data, wavelet decomposition and empirical mode decomposition (Wu & Huang, 2011) have been demonstrated as particularly capable techniques (Enayati, 2019; Gjerde et al., 2022; Steffensen et al., 2023). Figure 16 shows an example of EEMD applied to BCG data. EEMD is primarily noted here as a very useful tool for analysis of highly noisy and complex data. Unfortunately, EEMD may be prohibitively computationally expensive for on-line computation.

Using wavelet of EMD decompositions still require selecting which "level" of the decomposition to use, particularly in variable HR situations. However, it may be easier to create "rules" for selection based on quality metrics or requirements for each layer.

2.5 Summary

In summary, there are several sensor types currently under investigation for ubiquitous, unobtrusive BP estimation. Some are more widely used and technologically mature than others, such as ECG and PPG. BP estimation techniques often rely on measuring some flavor of PWV, a parameter with a strong theoretical connection to BP. This is often achieved by combining more than one sensor. Black-box modeling without using PWV will be discussed further in chapter 4.

3 Solving physiology sensor problems

The development side of this project has relied on engineering techniques common to early-phase pre-requirement product development (the "fuzzy front end"), such as rapid iteration and prototyping and development through convergent and divergent design cycles (Auflem, 2023; Sjöman, 2019; Vestad, 2022). This track has involved building sensor devices and supporting technologies as well as benchtop test rigs to benchmark performance and assist in method development and problem understanding.

This chapter focuses on sensor design. Following the techniques presented in the previous chapter, this chapter is intended to provide a view on how these techniques have to be considered from a design engineer's perspective in order to successfully solve a physiology sensing problem.

3.1 Artifacts and target variables

When it comes to design problems involving sensors, we need a clear-eyed conception of what a sensor is and what it does. In this context, we will follow a common definition of a sensor as a device that in some way reacts in response to an external physical stimulus by changing some characteristic that can be measured electrically (Fraden, 2016). An example is the strain gauge.

In its simplest form, we can think of a strain gauge as a length of conductive material of uniform thickness with a known and consistent electrical resistance. Under certain mechanical loads, the conductive material will elastically deform (i.e., it is strained), and as a result, the length of the resistor increases. By measuring the voltage across the component, a relative change in resistance can be observed.

In practice, the change in resistance will be very small, as will the resulting voltage difference, and circuitry to amplify the voltage will be necessary. In practice, strain gauges will also typically be built into devices called load cells, wherein the strain gauge itself will be bonded to a metal structure of precisely known dimensions such that the load condition can be controlled for calibration purposes.

3.1.1 Translation

As an example, let us say that a hypothetical strain gauge, if loaded under flexion with a 1 kg load, records a voltage drop of 1 volt. If the load is increased to a 2 kg load, the voltage drop increases to 2 volts. It is not correct to say that the sensor has measured a change of 1 kg; rather, we need to translate the true, recorded change – a difference in electrical characteristics of a circuit – into a concept that holds meaning for us. In the case of the load cell, the translation is ideally linear, and the entire system will be calibrated empirically – such that a load difference of 0.1 kg results in a voltage difference of 0.1 V across a reasonable range, for example – by repeated measures.

What the sensor is recording is directly caused by the load applied to the load cell, but the crucial distinction is that the component is *not* measuring *load*, it is measuring the *deformation of the stressed structure* (via change in resistance). In the case of our load cell, we can say that the target variable is the mass of the weight. The deformation of the bar is a secondary effect that we can

encode electrically. We can apply a model based on our physical understanding of the system (in this case, by assuming small, linear deformations in the scale and applying elementary beam theory) to estimate the target variable.

The example of the strain gauge is significant in the context of CV sensing. The clinical reference method of continuously recording arterial BP (ABP) consists of a fluid filled catheter, inserted into the artery, which in turn pushes on a small deformable membrane on which sits one or more strain gauges (Ortega et al., 2017). This device, the pressure transducer, is electrically connected to a Wheatstone bridge and amplification circuitry in the patient monitor, providing a varying electrical signal as the fluid pressure in the system changes.

In the absence of an a priori model, the measurement our sensor gives us is of limited value. We will say that the sensor is recording an *artifact* of the real world, rather than the real world itself. Staying aware of the separation between the output of the sensor and the true target variable is of great importance when approaching sensor design problems. In the setting of physiological monitoring, we are often interested in some physiological mechanism's response to a stimuli or development of some property of a biological system's development over time.

3.2 Hidden artifacts

In very many situations it will not be possible to directly measure the target variable of interest. In these situations, the next step is to identify secondary measurements that we have reason to believe are in some way relatable to the target variable.

As an example, the stiffness of the arterial wall – the lumen – is important increases with age, consequently, arterial stiffness is a valuable measure of relative "vascular age". Directly measuring the stiffness of the wall is, however, almost always impractical. But the stiffness of the arterial wall is related to the velocity of pressure propagation through incompressible fluid within it (via, for example, the Moens-Korteweg equation). We can probe the target variable, the stiffness, via the derived metric of pulse wave velocity.

What information is necessary for the designer's system to perform its task? In the cardiovascular or physiological setting, we are often concerned with measurement targets that are fairly concrete: is the central nervous system of this animal more or less activated? How much blood is being moved through the heart per second? How well oxygenated or hydrated is this tissue? But as concrete as these questions are, there are no sensors that will answer these questions directly. There is no such thing as a blood flow sensor – although there are several methods of determining blood flow velocity. The key concept is that all of the methods we can use to determine the target measure are indirect.

3.3 What do we *want* to measure?

The first task for a designer is to decide on what information their product ought to be able to provide. That is, what is the target variable? This is a question that can have several answers depending on the scope and framing of the problem. We can conceptualize three levels of information output: an overarching question about physiological state, a second, intermediary level in which we combine sensor measurements with established models or existing physiological knowledge, and a third and final layer where changes in the physical environment are causing the sensor to produce an electrical signal we can measure and pass up through the chain.

Figure 17 shows a diagram representation of how we can think of this kind of sensor problems. As an example, the most common type of automatic blood pressure monitor today is based on the oscillometric principle (Geddes, 2013). In an oscillometric device, an inflatable cuff is placed on the upper arm, and automatically inflated. A pressure sensor continuously records the air pressure in the cuff. The pressure is first increased to a point where the brachial artery is fully occluded, and is then allowed to decrease linearly. As the pressure decreases, a characteristic oscillating signal can be measured as the brachial artery is partially occluded, roughly coinciding with the Korotkoff sounds found in auscultatory techniques. The point of maximum amplitude of the oscillation is the mean arterial pressure. The systolic and diastolic pressures will then be extrapolated using any number of proprietary methods.

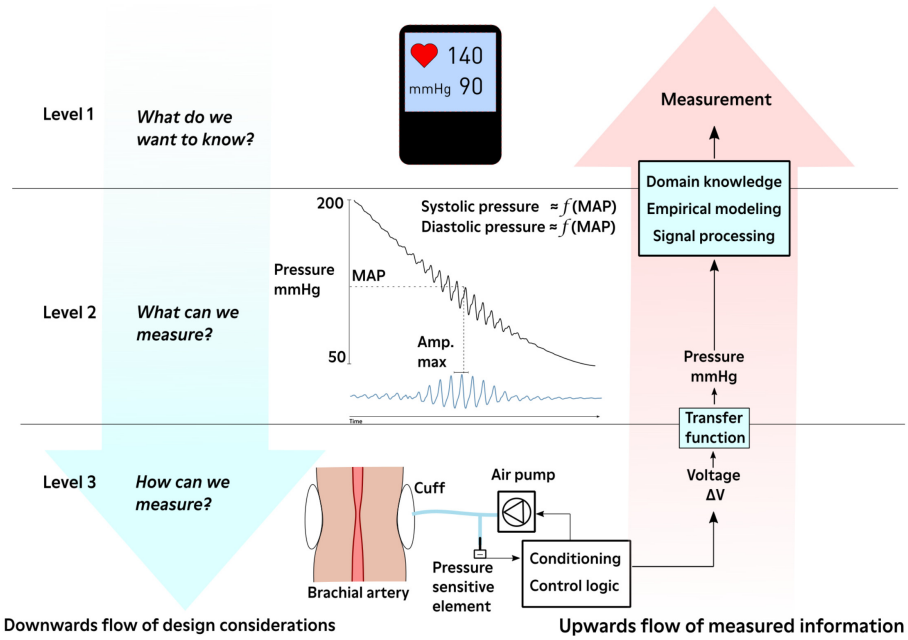

Figure 17. Diagram of the conceptual structure of a sensor problem, illustrated using an automated oscillometric blood pressure measuring device. From the engineering design perspective, each stage is broken up into deeper questions that eventually reach concrete technical implementations of sensing devices that react electrically to an external stimulus. This signal must be translated back up through the levels of abstraction. The first translation is typically transformation to an understandable representation, for example from voltage to physical pressure. To obtain an actionable measurement, we apply domain knowledge, modeling, and signal processing techniques to combine our recorded signal with other contextual information to obtain an actionable measurement at the end.

In the case of the oscillometric cuff, the large-scale question we want to answer is "what is the systolic and diastolic blood pressure?" This makes up the first level of our framework. To answer this question we apply knowledge of cardiovascular physiology and empirically based models to interpret a record of an electrical signal obtained from the inflation cuff device, making up the second, more abstracted layer. To obtain a usable signal that we can reliably interpret, we need to apply pressure in a controlled manner to a pressure sensor that is appropriately sensitive in the range of interest and be able to calibrate the sensor to provide a true representation of the actual pressure it is experiencing. This physical interface is the third level of our model.

3.3.1 Example application: acoustic sensing

Without a priori models, modern techniques in signal processing can enable us to extract patterns in our indirect measurements that may otherwise be very challenging. In Contribution 7, we describe a sensor problem based on determining the placement of an endotracheal intubation tube in a simulated human airway using ultrasonic acoustic pulses. The goal is to give performance feedback to a user training on the procedure.

Using the format presented in Figure 17, we can think of the question "what is the location of the endotracheal tube?" as our Level 1 question. The constraints of the problem limit our available options in Level 2: restrictions on possible sensor locations rules out sensors directly sensing the tube's location, and the complex geometry of the airway makes conventional sonar very challenging. In response, we can modify our question: is the tube inserted too deeply, correctly, or too shallowly? By using our domain knowledge of what the key parameters of the problem are, we rephrase the continuous location sensing problem to a categorical classification problem.

Level 3 now becomes a question of direct implementation. In our case, ultrasound acoustic sensing allowed us to record a signal that would be modulated by the geometry of the airway and keep the sensor discreet. Storing the signal as audio, we could apply a neural network transfer learning approach to translate our audio recordings into a label assigning the recording to one of a small number of states – too shallow, too deep, or correct. We thus ended up with a solution that showed high accuracy in the holistic sensor problem (Steffensen et al., 2023, submitted).

3.4 Solving complex physio sensing problems

Designers must keep in mind the different levels of the sensing problem and take a holistic approach in order to successfully solve the problem. This will often require integrating experience and knowledge from different disciplines such as engineering, data science, biology and medicine.

For example, mechanical engineering and materials science is necessary to design robust sensors that are fit to function in their operating environment. Engineering design can make informed decisions about human factors in the system, leading to user benefits and possibly user-derived

serendipity (see for example Contribution 6). Electronics and data science enable the conversion of physical stimuli into measurable signals and to let us extract meaning from raw data. A grasp of the relevant physiology is equally important for interpreting the sensor's performance during development and understanding the sensor's operating context.

3.4.1 Prototyping and Expert Users

No one designer will have all the necessary knowledge. Interaction with key users and domain experts can be crucial to extract lessons about the problem (Auflem, 2023). As an example, Contribution 5 describes a technology in which the use of sensors designed for humans had to be simulated in several crucial ways. The close interaction between designers and users led to a product that was both used successfully for its intended purpose (Brede et al., 2019), and commercially licensed following the filing of the patent application.

In essence, solving sensor problems for physio logging isn't about creating devices that convert physical effects into a series of digits. It's about understanding the target variable, distinguishing it from the sensor output, and working with the complexity of the problem. Successful designs are highly interdisciplinary and require combining insight from diverse disciplines to build a reliable and precise system.

To attack the complexity in these problems prototyping is a valuable tool (Vestad, 2022). The purpose of a sensor prototype varies, but one primary goal in the early phase of development is benchmarking and comparison to other methods. Controlled benchtop experiments can be very helpful in this regard. For example, to test the tonometer used in the wearable sensor described in the next chapter, the benchtop phantom described in Contribution 2 was used to provide a steady, repeatable pressure in the "artery". The phantom, shaped as a wrist with the radial artery running over a 3D-printed radius bone, let us attach the wrist worn sensor and probe design aspects like probe placement repeatability, logging software, et c. providing valuable opportunity for functional prototyping and verification alongside lab-level human tests using noninvasive volume clamp data (Finapres).

Ultimately the goal is to test our sensors on human subjects in as rigorous a manner as possible. As we shall see in the next chapter, testing on human subjects – central to CV sensor problems – can be a very involved process, potentially exposing subjects to risks which must be justified.

4 Human subject data collection

Two data collections took place involving human subjects. The main study involved 25 healthy volunteers undergoing radial artery catheterization and performing a bike exercise protocol. This study will be discussed here in some detail, alongside unpublished preliminary results. One publication, contribution 3, has so far been published based on this data collection.

The second collection involved in-lab recording of noninvasive CV data and anonymous biometrics, approved by Norwegian Agency for Shared Services in Education and Research (reference 250185). This study is presented in contribution 1.

4.1 Recording blood pressure during recumbent bike exercise

Work on cuffless BP estimation has primarily focused on rest conditions, which is valuable in the context of monitoring hypertension development and treatment response. However, there is little work available on exercise estimation, with a few notable exceptions. Cardiovascular responses to physical exercise, particularly acute blood pressure (BP) response, are risk markers for development of hypertension and overall cardiovascular events (Miyai et al., 2002; Thanassoulis et al., 2012). In order to contribute more meaningfully to the field of cuffless BP sensors, we set out to conduct data collection in a controlled exercise context.

4.1.1 Ethical considerations

Primary data collection for the BP sensor studies took place at St. Olavs hospital in late 2021. The study was approved by Regional Committee for Medical and Health Research Ethics Central Norway (REK Midt), application number *62226*. As a pre-requirement for approval by REK, approval for the use of a prototype medical device was applied for and obtained from the Norwegian Medicines Agency (Statens Legemiddelverk, SLV) with reference 21/06743. The study was registered at ClinicalTrials.gov with identifier NCT05008133.

As part of the approvals process, I undertook revision work to incorporate feedback from the original application, which could not be approved without approval from the Norwegian Medicines Agency. My primary contribution was writing the formal risk assessment, with medical subject matter assessment from the PI, Dr. Kirkeby-Garstad, completing the device description and assessing materials compliance with ISO 10993 standards, revising the documentation to be compliant with GCP and EU Medical Device Directives regulation, and overseeing the submission process.

4.1.2 Study design and protocol

The study was designed as a dual-posture ramping exercise protocol undertaken on a recumbent bicycle. Primary measurements were invasive BP collected via radial catheter and transducer, LVOT Doppler flow echocardiography, PPG, ECG, and tonometry plus accelerometry via the investigational device.

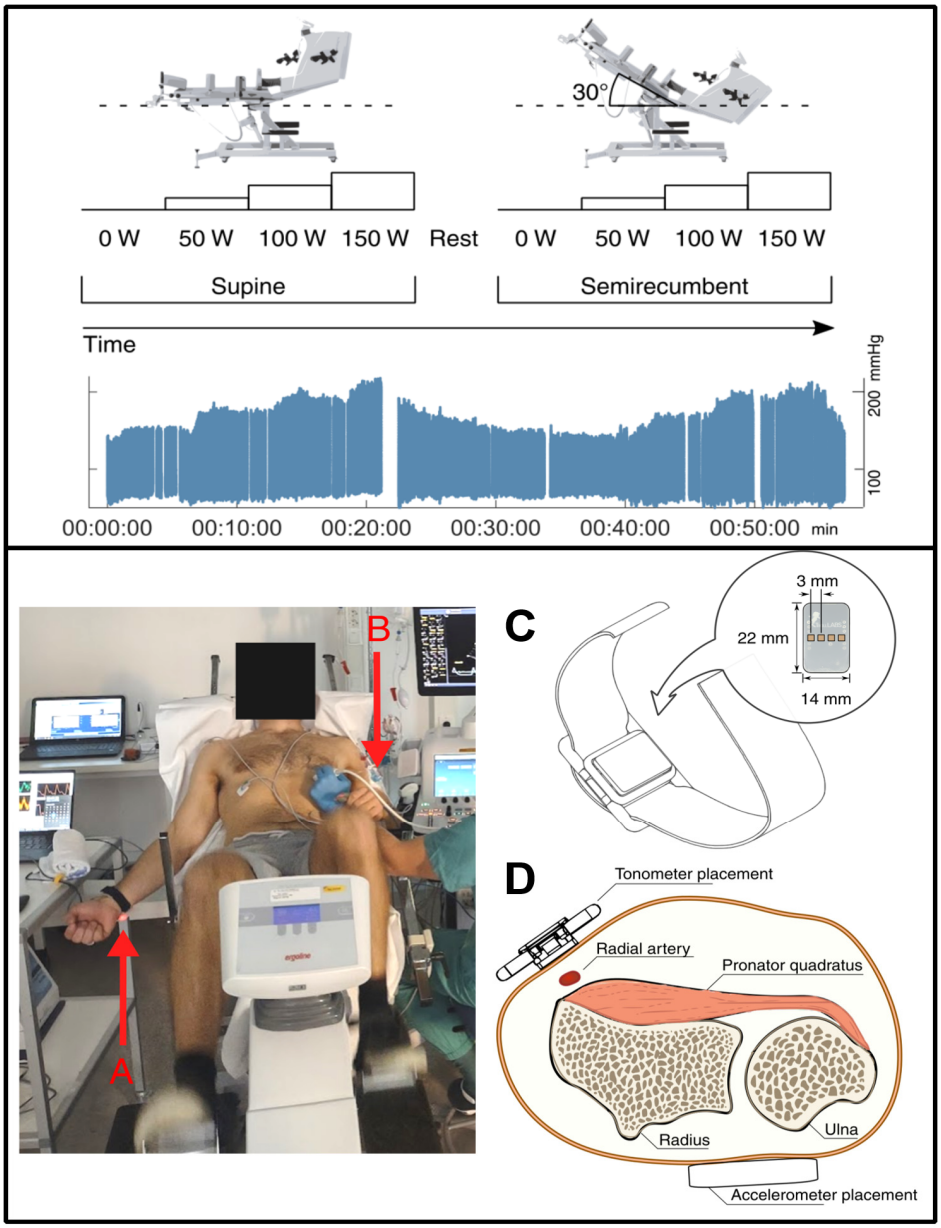

Figure 18. Data collection at St. Olav's hospital. Above: Overview of the experimental protocol with a sample BP tracing from the patient monitor. Missing data are due to technical limitations in the monitor recording software. Below: photo of a participant during semirecumbent sampling. A: location of the tonometer on the participant's right arm. B: location of the BP transducer fixed to the bicep at the midaxillary line. C: sensor schematic. D: sensor location over the radial artery at the distal radius. Illustrations from Steffensen, 2023, photo by written consent.

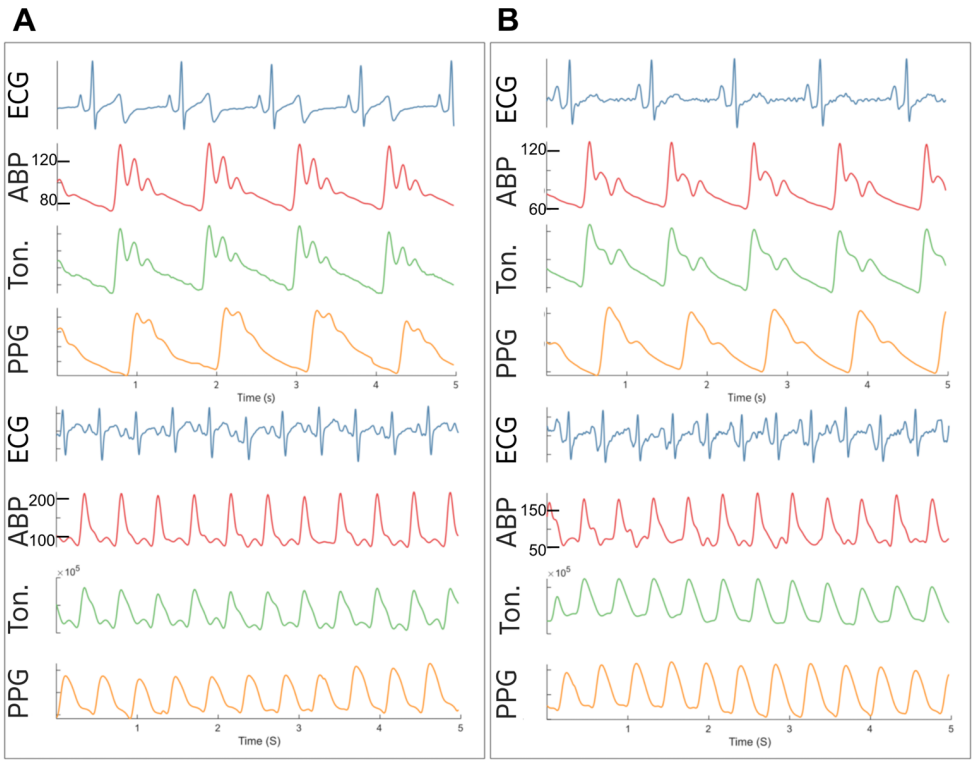

Figure 19. Sample sensor data at rest (top) and during exercise (bottom). A, B: simultaneously recorded waveforms from two female volunteers aged 33 and 31. Top to bottom: ECG, invasively recorded arterial BP in the left radial artery, noninvasive tonometry on the right radial artery, and PPG from the left thumb. Note the strongly amplified second systolic peak in the pulse on the left, which might otherwise be interpreted as an under-damped fluid line but is also reflected in the tonometric waveform as well as the PPG. Under good conditions, the signal recorded with the invasive catheter and non-invasive tonometer will be almost identical. Commonly, it will be damped.

An illustration of the experimental protocol is shown in Figure 18. Details of the study are available in Contribution 3 (Steffensen et al., 2023).

As the participants were healthy volunteers, undertaking the risk associated with any invasive procedure obliged that risk was minimized as much as possible. Inclusion criteria were enforced, and participants screened by the responsible site investigator, a consulting anesthesiologist. Exclusion criteria were age (below 18 or over 50), reduced manual circulation as determined via Allen test and confirmed under ultrasound, and increased thrombogenic risk. As the data collection took place under Covid-19 restrictions in Norway, participants were also required to

provide proof of vaccination, a recent negative Covid test, or were offered to take a rapid antigen test on site before being admitted to the hospital building.

The design of the study as a multi-posture exercise intervention was influenced by the goal of maximizing study value versus risk for the volunteers. The study was set up to allow several projects to benefit. There were two core projects, the first intended to map cardiac power across different exercise levels in healthy volunteers to form a baseline understanding of this metric. This project was anchored at the Clinic of Anesthesia and Intensive Care at St. Olavs and sponsored by the Department of Circulation and Medical Imaging at NTNU. The second core project was data collection for the CV sensor, formulated as an adjunct to the first study.
Several other research projects were simultaneously able to collect measurements alongside using invasive blood pressure data from the same study, thus maximizing the risk / benefit ratio of the study.

Bike exercise studies are typically performed with a ramp to exhaustion design. However, in this study participants were instructed to maintain four distinct power output levels (0, 50, 100, and 150 W, defined as Watts delivered to the exercise bike). This simplified echocardiographic examinations, and moreover provided relatively steady-state conditions allowing an investigation of wrist ballistocardiography (Steffensen et al., 2023).

A weakness of the study was the failure to collect subjective intensity measures such as Borg ratings in the absence of the ability to estimate max intensity by exhaustion. However, a comparatively large amount of data was collected per participant, and the use of invasive BP collected via arterial catheter provides a rare "ground truth" comparison, as opposed to Finapres / NIBP devices.

4.1.3 Effects of increasing heart rate on CV signals

During exercise, as the oxygen demand of the skeletal muscle groups increases, cardiac output must increase to supply oxygen and remove metabolic products. Initially, both HR and SV increase, providing a large increase in CO. Eventually, SV plateaus, and subsequent increases in CO are primarily driven by HR (Laughlin, 1999). The reduced duration of ejection as cardiac

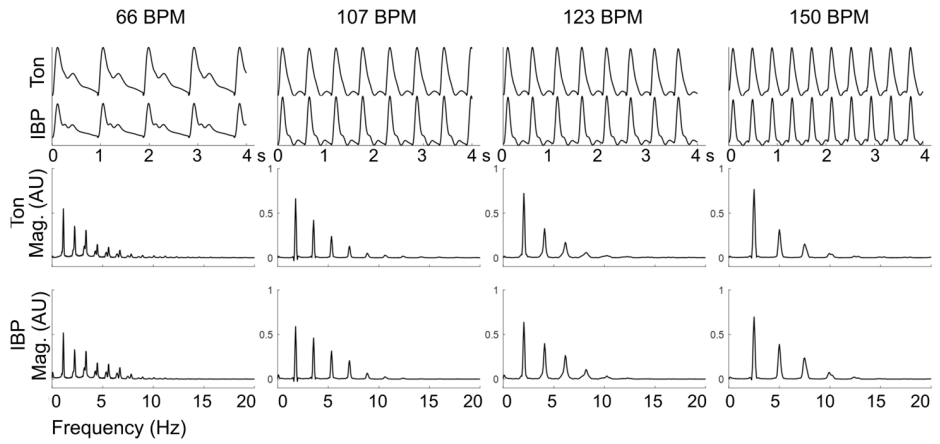

Figure 20. Waveform development with increasing exercise load. Top: waveforms collected from a participant during bike exercise, with increasing heart rate from left to right. BPM: heartbeats per minute, Ton: wearable tonometer data, IBP: invasive blood pressure. Bottom: frequency content of the average waveforms, calculated by taking the fast Fourier transform of the waveform series. Note the decrease in signal complexity. As heart rate increases the reflected wave merges completely with the systolic peak and the resulting waveform gets "spikier", with a simpler frequency content.

cycle time decreases leads to a large increase in pulse pressure, primarily driven by a large increase in SBP as DBP increases very little.

At high HR, the BP waveform becomes increasingly spiky, as wave reflection becomes completely absorbed in the main systolic peak. Figure 20 shows the development of the BP waveform from resting state to moderate intensity exercise. The simplification of the frequency content is also reflected in time-domain geometric indices.

To illustrate the time-domain changes during exercise, we can define a few metrics of particular interest. The first is the radial Augmentation Index (Kohara et al., 2005):

$$rAI_x = \frac{SBP2 - DBP}{SBP1 - DBP} \tag{3}$$

The rAI_x describes the augmentation of the SBP due to the reflected peripheral pulse wave. The above equation calculates the difference between the second, reflected wave (SBP2) and the first systolic peak (SBP1), dividing it by the pulse pressure. rAI_x has been used as a measure of arterial stiffness. Automated rAI_x measurement can be challenging due to the difficulty of reliably detecting the reflected peak. This is particularly problematic during exercise, as we have seen how

the reflected peak is largely absorbed. Here, we average 15-25 tonometry and catheter beats to obtain an average heartbeat. We then attempt to define the location of SBP2 via the zero crossing of the second derivative of the waveform following the main systolic peak.

Figure 21 demonstrates the idea of this procedure. Note that, while a peak may be detectable in the invasive waveform, the tonometer signal does seem to lose the ability to discern the precise location of the relevant inflection with increasing HR. This implementation can certainly be improved upon, however. There is also a valid question to ask about whether or not rAI_x is even a valid metric at elevated HR, or should at least be normalized against HR (Stoner et al., 2014).

The Form Factor is the ratio of the height of the MAP above the DBP to the pulse pressure (Nichols et al., 2011):

$$FF = \frac{MAP - DBP}{SBP - DBP} \tag{4}$$

We estimate the area under the curve (AUC) as the integral of the normalized beat waveform:

$$AUC \approx \sum_{i=1}^{n} z_i \tag{5}$$

To compare the two differently scaled waveforms, z is the beat waveform, y,normalized via z-scoring and then translated to be strictly positive.

$$z = \frac{y - \mu_y}{\sigma_y} + \min(z) \tag{6}$$

Figure 22 shows values for rAI_x, FF, and AUC in averaged heartbeats at each exercise condition. The difference between conditions is illustrative of the reason why exercise conditions challenges assumptions of typical cuffless BP estimation approaches.

There are large differences in time domain morphology, alongside signal frequency content as shown in Figure 19 and Figure 20. Note the generally elevated tonometer values, indicative of the smoother signal. This is likely due to the incomplete applanation that is typical of wearable tonometry. It's also possible that it's due to underdamping of the fluid line (Nichols et al., 2011; Saugel et al., 2020), but this is hard to say without frequency response tests of the system, and as this data was recorded via a commercial

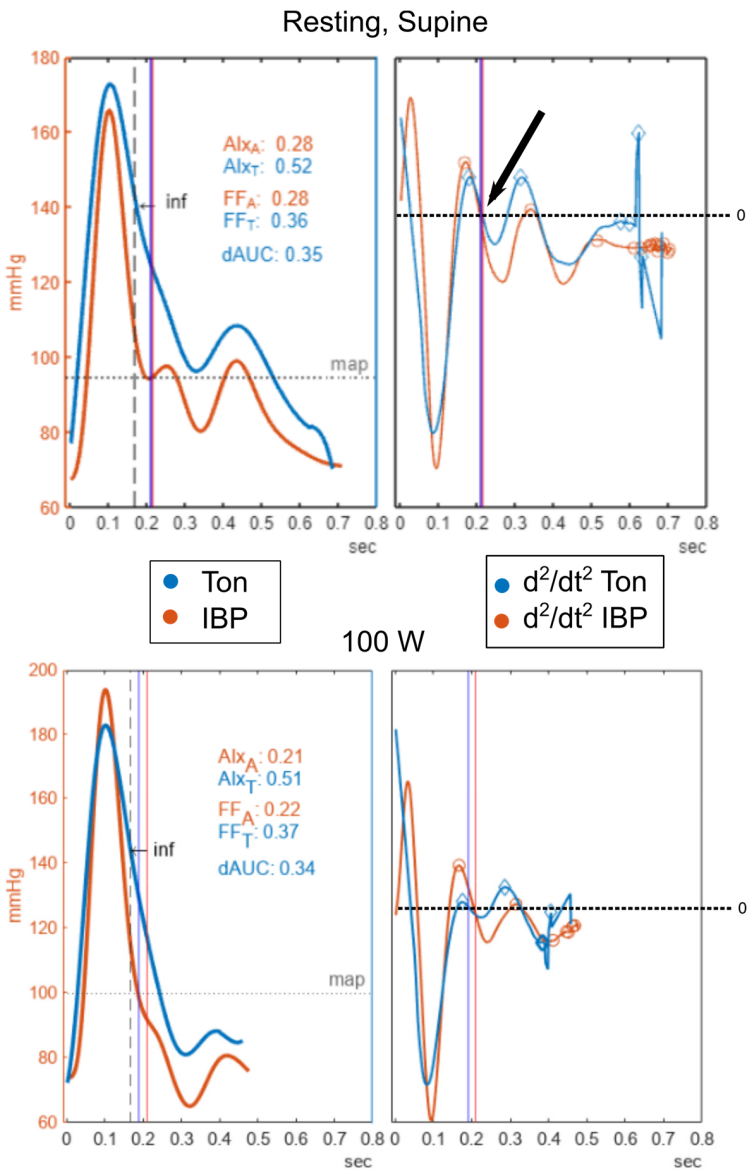

Figure 21. Second systolic peak detection for radial AI determination. Ton: tonometer, IBP: invasive BP.

patient monitor we do not have insight into the conditioning and filtering steps that were performed on the raw transducer output.

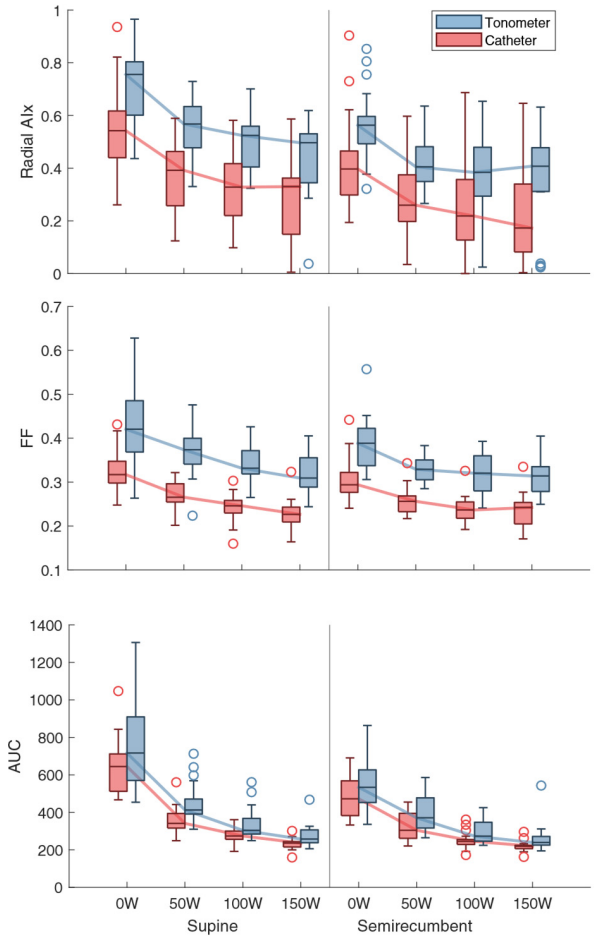

Figure 22. Development of three characteristic shape metrics during exercise. Top: Radial augmentation index (rAIx,) middle: form factor (FF), and bottom: area under the curve (AUC).

4.2 Noninvasive blood pressure estimation during exercise

4.2.1 Black-box estimation

Apart from physics-based modeling approaches, an increasingly popular approach is the so-called black box regression model, wherein there is little or no insight into the inner decision functions of the model. The approach is to collect a dataset containing the target variable, for example SBP

or DBP, alongside concurrently recorded data from some type of sensor, usually waveform data in one of the forms previously discussed. Any number of regression models are then let loose on predictor features extracted from the sensor data. The models range in complexity from the parsimonious and interpretable, e.g. ridge regression, to the highly complex and opaque, e.g. neural networks.

Many different features have been extracted from pulse waveforms and used in this way, with and without any underlying physiological reasoning. Commonly used features include heart rate and PWV-type measures alongside various PWA indices and metrics. Neural networks may also be used to train on sequences of time series data.

For our use, we can broadly divide CV parameter regression models in two categories: the calibrated or intra-individual model (personalized model), or the uncalibrated inter-individual or population model.

In the case of the intra-individual model a ML regression algorithm is trained on both target variable (BP) and estimator variable (e.g., waveform features) data from the same individual as the model is later tested on. These models typically perform better than the inter-individual models and are inherently sensitive to individual differences in cardiovascular dynamics. However, they require access to ground-truth data that is often difficult or impossible to obtain out of the lab. In the case of continuous, calibrated waveform data they require expensive equipment such as the Finapres device or cuff measurements, which are sparse and subject to all the accuracy concerns inherent in commonly available consumer oscillometric devices.

In an ideal BP estimation environment, the estimator should not need to have access to high resolution continuous BP data from the target individual. The ideal wearable BP estimation device ought to function much in the same way as a heart rate monitor. To avoid the need for high quality ground-truth waveform data in our model, we are left with population based models. These models are trained on target and estimator data from as large a number of other individuals as possible. If we are lucky, and have estimator data that does contain some predictive value for our target variable, we can apply the population model to our target individual's estimator data and obtain a reasonable estimate of the target variable.

The limitation of this approach is that by focusing on population trends the model may lose sensitivity to individual-specific variations, resulting in a loss of predictive power. Population models typically need a very large number of individuals to cover enough of the data variance to respond to new individuals. Building these large models requires a large investment in data collection. Additionally, when collecting population data there is a risk of introducing bias by focusing solely on specific demographics for model training data, potentially limiting the validity of the model outside the demographics used for training.

In short, intra-individual models may better capture individual idiosyncrasies or hemodynamic characteristics but require individual training data that is usually impractical to obtain. Population models overcome the need for individual data but can fail to capture individual differences in unseen populations and can fail to generalize. The intra-individual model, although it can have limited generalizability, can still be used to demonstrate whether or not the estimator variables in a collected dataset has predictive power for the target variable, and can motivate further research efforts in gathering larger datasets. A combined approach can be imagined, wherein a population-based model is informed by discontinuous individual features as part of a larger modeling environment.

4.2.2 Neural Network Regression Model

Using data collected during the study, we trained a 1-dimensional CNN multi-input network with a single value regression output layer. The architecture consisted of an input layer with four inputs: a sequence of length 34, and three single-feature inputs.

The CNN inputs were individual beat sequences, segmented, resampled to 30 Hz and zero-padded to an even length of 34 to reduce the dimensionality of the model to a manageable level. In addition, three features were separately calculated and input to the model as separate inputs: beat duration (foot to foot), beat amplitude, and beat width at half prominence of systole. Models were separately trained on tonometer data and thumb PPG to compare performance.

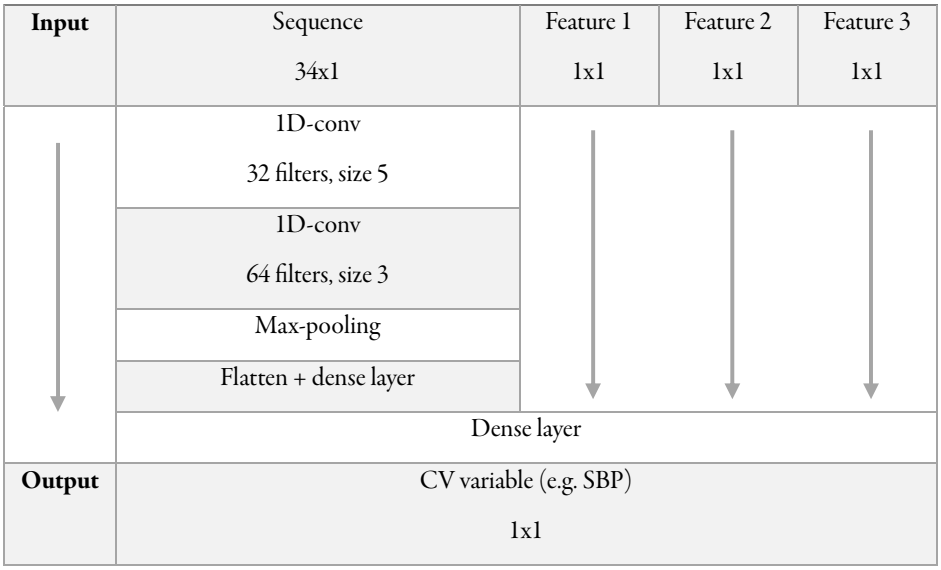

Figure 23. Diagrammatical representation of the CNN structure.

The model and input features were inspired by by Sel et al (2023), although their customized loss function was not used as the reference implementation was deemed to have potential data leakage issues between the training and test data set.

Model input data were beats passing a windowing self-similarity quality indexing check as described in chapter 3. To simplify processing, tonometry was used for the quality check, and PPG beats corresponding to failed tonometry beats were also discarded. For each beat, SBP was set as the peak value of the corresponding arterial BP beat, MAP as the arithmetic mean, and DBP as the minimum value. A total of 118498 beats from 24 participants were used. The mean number of beats per participant was 4973. Separate models were trained for target variables SBP, MAP and DBP. SBP had the highest variance in response to exercise, if the model performance were unacceptable in the "best case" scenario, this would indicate serious weaknesses of the modeling approach.

Models were trained and tested using a leave-one-subject-out (LOSO) scheme, training using data from 23 participants and then testing on the 24th to assess its performance on unseen data.

This was repeated for each of the 24 participants. During the training step, 5 groups from the training set were used at a time for validation in a group hold-out scheme, and model training was stopped when validation loss stopped increasing.

4.3 Results

4.3.1 Performance metrics

Results per participant are presented visually in Figure 25 and table II. To assess the performance of the model, we define the following metrics:

$$MAE = \frac{\sum_{i=1}^{n} |y_i - \hat{y}_i|}{n} \tag{7}$$

The Mean Absolute Error (MAE) is simply the mean of the absolute errors between the true value at a point, y, and the model prediction $\hat{y}$. The MAE is less sensitive to outliers than a related commonly used metric, the Root Mean Square Error (RMSE):

$$RMSE = \sqrt{\frac{\sum_{i=1}^{n} (y_i - \hat{y}_i)^2}{n}} \tag{8}$$

To assess the ability of the model to capture trends in the BP series, we also use a correlation metric. We use Spearman's rank-correlation coefficient:

$$\rho = \frac{cov(R(y), R(\hat{y}))}{\sigma_{R(y)} \sigma_{R(\hat{y})}} \tag{9}$$

Here R(x) are the ranks of vector x, $cov(R(y), R(\hat{y}))$ is their covariance, and $\sigma_{R(y)}$, $\sigma_{R(\hat{y})}$ are the standard deviation of the rank vectors. Using rank correlation can provide a better assessment of nonlinear trends in the underlying data than Pearson's correlation coefficient, which uses the same formula but applied to the raw data instead.

4.3.2 Individual variation

Figure 24 A shows the best and worst participants for SBP according to MAE and ρ. The range in MAE between participants is broad (7.6 to 27.9 mmHg, mean 15.2 mmHg). This could be the result of differences in physiological response to exercise being captured unequally by the model

Table II. Overview of performance metrics for CNN estimation of SBP per participant.

Participant	N beats	MAE	RMSE	ρ	Participant	N beats	MAE	RMSE	ρ
1	4195	18,45	22,34	0,78	**13**	4455	18,98	24,67	0,78
2	4892	8,81	10,9	0,77	**14**	3058	10,61	12,25	0,86
3	1279	11,93	16,26	0,39	**15**	5530	19,06	22,54	0,76
4	5374	11,96	14,51	0,92	**16**	4412	14,9	17,98	0,81
5	5877	26,12	30,71	0,82	**17**	5168	14,46	19,81	0,68
6	5070	26,54	32,45	0,96	**18**	3610	20,19	26,63	0,73
7	2943	12,43	15,88	0,86	**19**	6617	7,60	9,67	0,93
8	6451	12,18	15,64	0,74	**20**	5447	17,74	21,9	0,85
9	6457	16,42	19,39	0,87	**21**	6339	9,89	12,96	0,79
10	5423	8,51	11,21	0,89	**22**	2980	12,34	14,97	0,82
11	6699	27,94	30,90	0,90	**23**	4495	11,36	14,39	0,85
12	3964	9,23	11,86	0,90	**24**	7763	17,01	19,61	0,45
					Σ	118498	15,57	20,19	0,81

because of the small number of participants in the training data set. It might also be explained by differences in data quality between participants. Interestingly, however, there was no clear relationship between number of available beats and any of the performance metrics.

For the participant with the fewest available beats (N = 1279) the model managed to estimate the resting SBP reasonably well, but fails to follow the subsequent rise in SBP, likely due to low availability. This example serves to illustrate the importance of reliable data acquisition as even in a controlled lab environment data quality from tonometry can be poor.

Figure 24 B shows scatterplots of the total collected dataset and the model predictions as well as the residual plot. While there appears to be a good overall correlation between the ground truth and the predictions, the residual plot shows that within participants many participants' predictions are clearly skewed, implying overestimation in the low BP regime and underestimation in the high BP regime. Figure 27 shows the mean error versus distance from mean value.

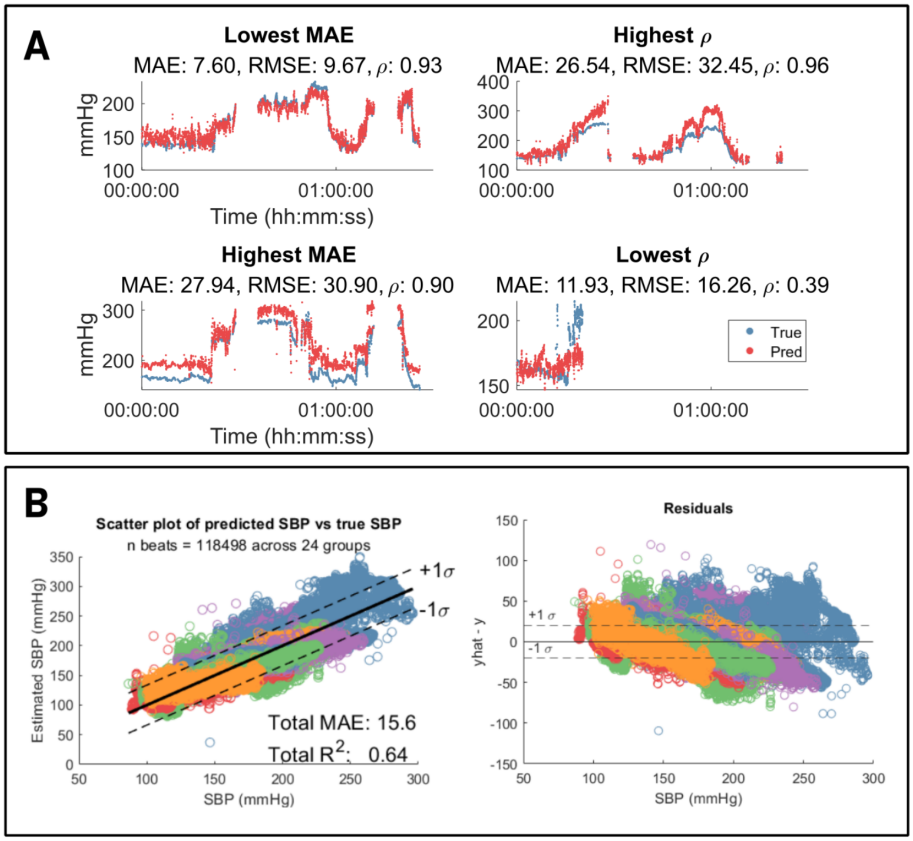

Figure 24. A: Best and worst cases from SBP estimation during acute exercise. Correlation between the estimated trend curves can be in good agreement with the actual ground truth even in the case of the worst absolute error estimation: the highest correlation has one of the worst absolute errors. When correlation is low, the estimation trends towards the mean value of the series, resulting in a lower-than-expected absolute error. B: scatter and residual plots of estimated SBP vs. true SBP. Each point is one beat. Colors represent separate participants. The participant residuals are clearly skewed, although the total data set is zero-centered and broadly symmetric.

While there is variation between individuals as well, the average correlation is reasonably high ($\rho_{Mean} = 0.79$). From visual inspection of the individual trend plots the models seem to have reasonable ability to capture the contour of drastic changes in SBP during exercise.

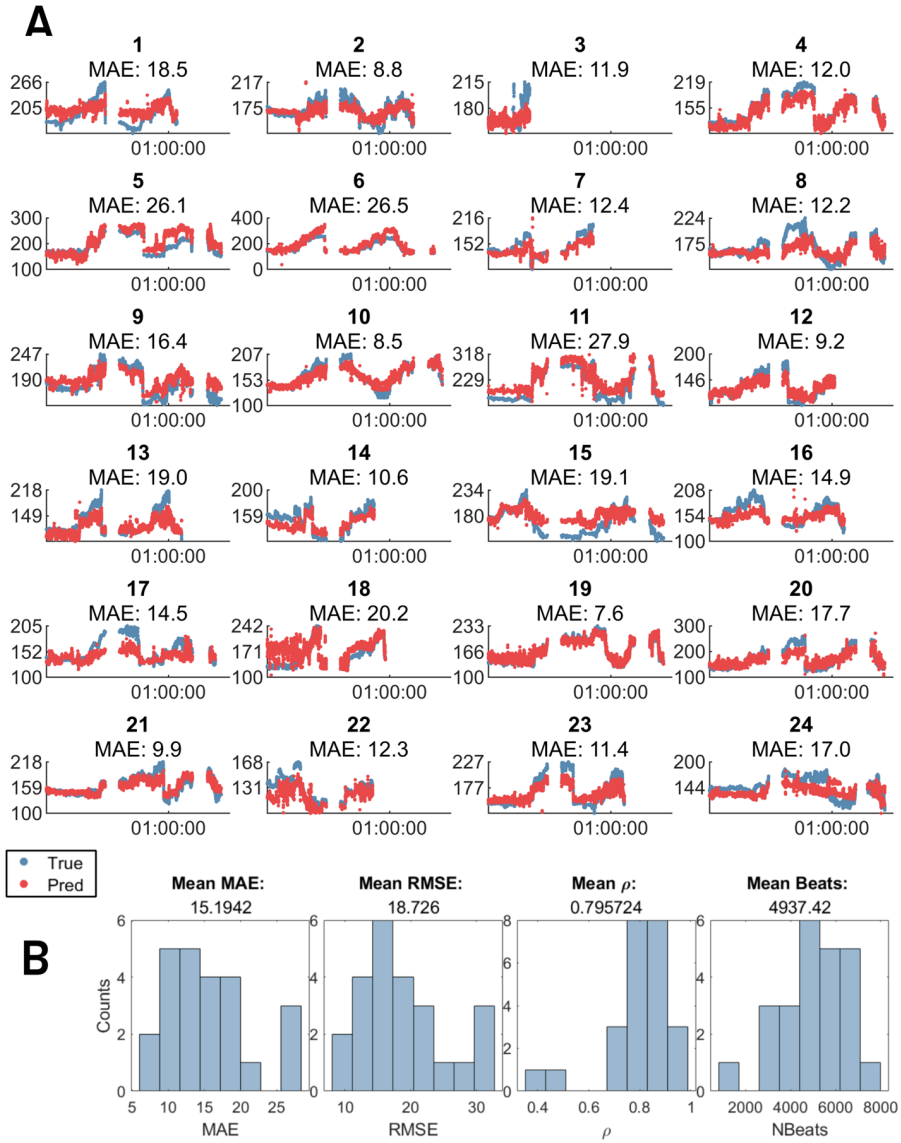

Figure 25. SBP estimation per participant. A: true and predicted SBP timeseries plotted against each other. Vertical axis is mmHg, horizontal axis is time (mm:hh:ss). Missing data points are due to missing measurements or low quality waveforms. There is large variation in data availability over the stages of the protocol. B: histograms of performance metrics. Each count is one participant. SBP: Systolic Blood Pressure, MAE: Mean Absolute Error, RMSE: Root Mean Square Error.

Table IV. Aggregated per-participant performance metrics across SBP, MAP, and DBP between tonometer and PPG.

	MAE		RMSE		ρ	
	Mean	Median	Mean	Median	Mean	Median
SBP						
Ton.	15,19 (5,81)	13,45 (7,73)	18,73 (6,64)	17,12 (8,77)	0,81 (0,13) *	0,83 (0,13)
PPG	15,53 (5,09)	14,60 (5,86)	19,20 (6,41)	18,26 (7,00)	0,73 (0,17)	0,77 (0,17)
MAP						
Ton.	6,20 (2,41) *	5,15 (1,92)	7,70 (2,65)	6,61 (2,07)	0,77 (0,13) *	0,82 (0,14)
PPG	7,05 (2,72)	6,27 (1,65)	8,59 (2,98)	7,64 (2,10)	0,66 (0,20)	0,70 (0,16)
DBP						
Ton.	3,75 (0,85)	3,69 (0,99)	4,70 (0,99)	4,55 (1,14)	0,47 (0,26) **	0,52 (0,43)
PPG	4,14 (1,04)	3,98 (1,51)	5,10 (1,16)	4,78 (1,67)	0,30 (0,28)	0,37 (0,44)

Ton.: tonometer. Numbers in parentheses are standard deviation for mean values and inter-quartile range for median values. *: significant difference between tonometer and PPG derived models at $\alpha < 0.05$ with Bonferroni-Holm correction for repeated measures. **: corrected $\alpha < 0.01$. Two-tailed Wilcoxon test.

4.3.3 SBP, MAP, and DBP: tonometer vs PPG

Table IV compares model performance on SBP, MAP, and DBP for both tonometer and PPG derived features. The values are aggregates from each individual model performance (n = 24 models). As the data has outlying low-performing individual models (Fig. 25 B), both mean and median are reported.

To assess differences between tonometer and PPG models, the two-tailed Wilcoxon signed rank test was used at significance level $\alpha = 0.05$. Tests were MAE and ρ between tonometer and PPG for SBP, MAP, and DBP, resulting in 6 total tests; Bonferroni-Holm correction was applied to the p-values. No hypotheses changed due to correction. Significant differences are noted in Table IV using asterisks.

Overall, the values are broadly comparable, but the tonometer-trained models appear to consistently give slightly better outcomes. Tonometry consistently resulted in models with significantly better correlation to the ground truth data. For MAP, the difference in total estimation error was also significant. Neither model appears to be able to satisfactorily predict DBP, presumably due to the lower total variance in DBP during exercise.

Table V presents the total model error for all predictions. Figure 26 presents residual plots for SBP, MAP, and DBP using tonometer and PPG models.

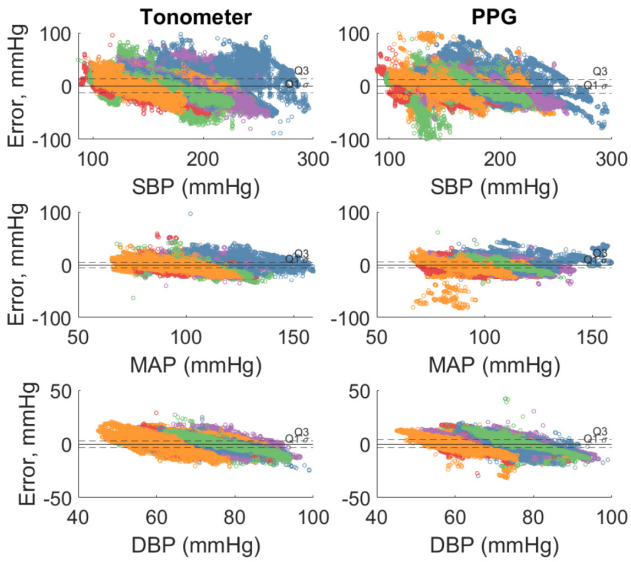

Figure 26. Residual plots for SBP, MAP, and DBP estimates from tonometer and PPG sources.

Table V.	Comparison of total model error.		
Tonometer	SBP	MAP	DBP
MAE	15,6	6,4	3,8
SD	20,1	8,4	4,9
PPG	SBP	MAP	DBP
MAE	15,7	7,2	4,2
SD	20,4	9,4	5,3

The results imply that while the modeling approach does not provide a satisfactory generalization, reasonably effective estimation of SBP and MAP during exercise is possible. Tonometry slightly but significantly outperforms PPG. Poor generalization is likely primarily due to the small sample size of this pilot study, as well as the crude modeling approach.

Without accurate calibration, the ability to track trends and relative changes from baseline could still be quite valuable in situations like post-surgery recovery or to alert at risk individuals of orthostatic drop (postural hypotension). Relative increase in BP from baseline could also be used to track individual response to exercise, providing opportunities for e.g., sports performance monitoring.

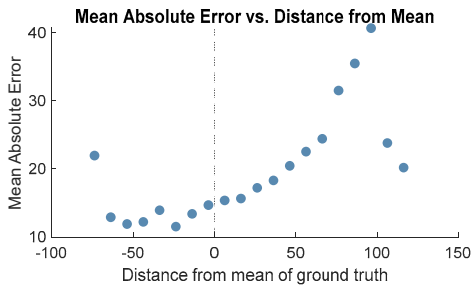

Figure 27. Relationship between prediction error and offset from data mean. Data is all predictions, binned per 10 mmHg distance from mean. Note that the mean is higher than resting SBP.

4.3.4 Relation to similar work, limitations, and outlook

These results should be considered preliminary and primarily illustrative for the potential application of noninvasive waveform data to BP estimation during exercise. Exercise conditions challenge assumptions about cuffless BP estimation. The perturbation from baseline can be very dramatic compared to the reference range (increases of more than 100 mmHg are not unusual in moderate intensity exercise), and it is not clear that models that perform well in rest or low work states will work during higher work states.

Landry et al. (2022) used a combination of ECG and PPG to estimate MAP during a ramp exercise protocol using both time series models and PAT models in a data set of 21 minutes of measurements from 11 participants. While the methodology may not be directly comparable, the reported correlation coefficients around 0.6-0.8 and mean error standard deviation of around 11 mmHg MAP is in line with our results. We observe a mean σ_{Err} = 8.4 mmHg for MAP using tonometer-derived models and 9.4 using PPG-derived features (Table V). Given that our deep learning architecture is relatively simple, a fair hypothesis to explain our lower error is the larger size of our dataset.

Interestingly, Landry et al observe an effect on MAE of the model based on the range of BP changes in the training set. They report worse model performance with inclusion of more extreme values in the training set, by omitting the max intensity training data, the model performs better overall (lower total MAE) but is significantly worse predicting the highest intensity values.
In our results, training on all available data, we observe an increasing MAE with higher BP (Figure

27). This effect could be due to the relatively high rate of low-quality beats in this range in the dataset, lowering the models' predictive ability in this range. Separate models might be needed for exercise BP prediction as compared to resting or long-term prediction.

The time duration of the data available does not allow for a longer-term assessment of model performance over time. Drift and the need for regular calibration are noted problems in cuffless longitudinal BP devices. Perhaps the highest quality data on this problem currently available is the report by Han et al. (2023) where 760 participants wore a PPG device including a BP estimation algorithm (Samsung Galaxy Watch 3 or Active 2) for 30 days. The device estimated SBP and DBP intermittently (on average 1.5 times per day) and was calibrated against a cuff device. Users obtained the cuff measurements themselves using a validated cuff device and calibrated the model by reporting the cuff readings into a smartphone app. Users were instructed to calibrate the device against cuff BP once in a 30-day period. The authors investigated periods with data from at least 7 days before and 7 days after calibration and found an average pre-post calibration error of 6.8 ± 5.6 mmHg. Individuals with hypertensive BP values had significantly higher errors.

The error in estimation is significant, noting that it is clear that even if the calibrated device output estimates within cuffless BP validation guidelines (Stergiou et al., 2023), the device fell out of compliance after about 10-15 days. Still, with improved calibration techniques, this is perhaps the clearest evidence that cuffless BP devices can function practically in a real-world ambulatory setting. It must be noted that this study does not demonstrate the ability to track changes in BP within the same individual, either due to changes in physiology or due to non-static measurement conditions (see commentary by Avolio, 2023).

Validation guidelines involving testing during non-static rest conditions, such as exercise, have only very recently been formulated for cuffless devices (Stergiou et al., 2023). The ESH guidelines lay out the rationale for testing cuffless BP devices during exercise:

> Rationale: [Exercise test] shall be used for cuff-calibrated or demographic-calibrated cuffless BP devices (...). It assesses the ability of the cuffless device to track physiological BP increases (...). It will also show whether the cuffless device can provide accurate BP measurements under some motion (similar to what may be encountered in daily life).

> Submaximal cycling, which has limited risks for subjects, will be employed to induce substantial, short-term but steady (for a couple of minutes) BP increases.

Given the need to understand BP estimation models during exercise conditions, we hope that the preliminary work presented here and the dataset that is hopefully to be made publicly available may contribute to improved reliability of these devices, and perhaps towards enabling truly continuous BP measurement, opening opportunities in research and clinical practice.

The limitations of this study lie in the small sample size, motivating larger studies with more diverse demographics, and in the processing and modeling approach. In particular, the exclusion of PPG beats associated with low-quality tonometry beats potentially excludes viable PPG beats, which might have improved PPG model performance. On the other hand, it does provide a fair assessment of two equally sized feature sets.

A future publication should compare different modeling approaches and model architectures, particularly more explainable models, and should investigate metrics derived by combining multiple sensors. Each sensor was treated separately in this analysis. With the addition of additional sensors, particularly the ability to track PTT during exercise, the shape of the relationship between each variable might be valuable on its own as a marker of CVD risk (Liu et al., 2014).

To address these limitations and to build on the initial findings presented, a more detailed paper is being planned. Although the complete paper is beyond the present thesis, an abstract outline has been prepared as Contribution 4 based on the results presented here.

5 Conclusions and future work

5.1 Addressing the Primary Research Objective

The Primary Research Objective was stated as:

> **Primary Research Objective**
> Develop wearable technologies that allow for ubiquitous and non-invasive cardiovascular monitoring towards enabling close-to beat-to-beat blood pressure monitoring via iterative development, benchtop test rigs, and human trials.

To address the Primary Research Objective, we defined three Research Tasks:

Research Task 1. To develop and use lab test rigs to benchmark devices for wearable CV monitoring, focusing on tonometer-derived pulse wave analysis and wearable ballistocardiography.

Research Task 2. To develop devices measuring physiologically relevant variables to probe central cardiac events distally.

Research Task 3. To test these devices under a broad range of physiological states in healthy volunteers against ground truth invasive measurements.

Addressing Research Task 1, Contribution 2 (Embedded Inductive Sensors...) demonstrates our wrist phantom, encompassing a sensorised radial artery compressible against a 3D-printed radius bone. By building in a novel braided coil, we showed how we can accurately record the diameter change of the artery in response to a controlled pressure pulse.

Addressing Research Task 2, in Contribution 1 (Windows to the Sole...), we have presented a novel implementation of pneumatic sensors and advanced signal processing to enable wearable force BCG sensing in a potentially out-of-lab environment. We were able to use the BCG to estimate central AVO and calculate PTT, thus addressing Research Task 2. This study further included a lab test rig in the form of a modified bathroom weigh scale, implementing known techniques from the literature to benchmark our sensor's performance, further contributing to Research Task 1.

Research Task 3 has been addressed in the study described in Chapter 4, Contribution 3 (Wrist ballistocardiography...), and the planned Contribution 4 (Cuffless estimation...), describing an invasive human trial. We have shown, to our knowledge for the first time, that the acceleration BCG can be recorded at the wrist during exercise, pushing this technology into new areas. Using the BCG we calculated PTT during exercise, which decreased as expected with increasing HR and BP. Using the tonometer waveform data, we trained deep learning models to estimate BP against clinical reference invasive BP during exercise, to our knowledge for the first time. We thus contribute to an increasingly important field of study in the context of cuffless BP monitoring.

Together, the contributions generated in addressing the Research Tasks have resulted in a valuable contribution towards the Research Objective of enabling high resolution unobtrusive and ubiquitous cuffless BP monitoring.

5.2 Addressing the Secondary Research Objective

The Secondary Research Objective was formulated to support activities in pursuit of the Primary Research Objective:

> **Secondary Research Objective**
> To achieve the primary objective, generate insights into wearable sensor design and development techniques as they apply to cardiovascular monitoring in noisy situations, including prototyping and experimental techniques relevant to sensor design.

The associated Research Tasks were:

Research Task 4. To develop methods for simulating and benchmarking relevant artifacts of the cardiovascular system

Research Task 5. Develop and apply signal processing methods to obtain usable results in high noise scenarios

Research Task 6. Contribute to an understanding of prototyping methods in the concept selection phase of sensor product development.

Research Task 4 is addressed by Contribution 5 (Ultrasound Phantom), presenting a patent application for our vascular simulation phantom. Methods learned from the development of the technology in Contribution 5 contributed directly to Contribution 2 (Embedded Inductive Sensors…), in which we directly simulate pulsating BP in a radial artery phantom, thus addressing the Research Task and contributing to Research Task 1.

Addressing Research Task 5, signal processing methods for dealing with very noisy data were demonstrated in Contribution 1 (Windows to the Sole…) and Contribution 3 (Wrist ballistocardiography…), where advanced methods such as EEMD are applied together with more standard methods such as bandpass filtering, segmentation, and averaging to address low SNR data. Research Task 5 thus contributed to addressing Research Task 2.
Contribution 7 (Playing the Pipes…) presents an application of machine learning including support vector machines and deep learning / transfer learning to acoustic timeseries data. Techniques learned in Contribution 7 directly applied to the results presented in Chapter 5 and outlined in Contribution 4 (Cuffless estimation…), thus contributing to the goal of Research Task 3.

Finally, Contribution 6 (TrollBOT) and Contribution 7 (Playing the Pipes…) address Research Task 6 by sharing lessons from addressing commonly encountered challenges in applied sensor problems such as sensor placement, data processing considerations, wireless communication in early product development contexts, and sharp learning curves.

The tasks addressed in undertaking the Secondary Research Objective have thus contributed to enabling the contributions addressing the Primary Research Objective, which was the goal of the Secondary Objective.

5.3 Outlook and implications

The August 2022 consensus statement of the European Society of Hypertension (ESH) Working Group on Blood Pressure Monitoring and Cardiovascular Variability warned that "cuffless BP devices have specific accuracy issues", rendering established validation protocols for cuff BP

devices inadequate (Stergiou et al., 2022). As of this writing, the ESH has just published its recommendations for the validation of such devices (Stergiou et al., 2023). Testing during exercise is prescribed as one of six possible tests.

These recommendations clearly distinguish between continuous and intermittent measurement devices. Yet, the development of clear recommendations for cuffless BP devices, testing standards, and acceptance criteria demonstrates the maturation of this field. Looking back, the challenges of BP estimation during exercise and the prescription of exercise tests for these devices calls urgent attention to the lack of high-quality data on wearable BP estimation during dynamic exercise. By the continuing work of my collaborators in presenting our results in this area, and ideally to be able to share our dataset openly, it is to be hoped that we can contribute in some slight way to a clearer understanding of this field.

5.4 Directions for future work

I would pose the following suggestions as promising avenues of future work:

1. Effectiveness of cuffless BP estimation devices during moderate to high intensity exercise and other significant CV perturbations is underexplored. To develop robust calibration methods, large, openly available data sets from a diverse demographic is required. These should ideally contain commonly used sensor types, e.g., PPG, tonometry, and ECG, alongside a continuous BP measurement. Invasive measurements, while ideal, are often impractical, difficult, and expensive to obtain. Continuous volume-clamp BP data can be an acceptable substitute.

2. The use of ballistocardiography as a marker of central cardiac activity, particularly onset of rapid ejection, could be a valuable tool for longitudinal monitoring of post-surgery convalescence. Combined with ECG, systolic timing intervals can be recorded beat-by-beat alongside peripheral pulse wave velocity, providing both cardiac and vascular metrics continuously, providing venues for monitoring cardiovascular coupling, onset of sepsis et c.

3. Cardiac vibration monitoring is currently focused on chest vibrations recorded via sternum-mounted devices. Underexplored opportunities remain in wearable applications outside the chest-mounted device. In particular, the smart insole / smart shoe appears undeveloped in the context of ballistocardiography, pulse transit time, and pulse wave analysis.

5.5 Final reflections

Engineers working on questions relating to cardiovascular functionality need to maintain an awareness of fundamental principles of the circulatory system, fundamental sensor technologies – their applications, strengths, and limitations – as well as methods of application: diagnostic classification, parameter estimation, and trend tracking. The engineer working in this field also must maintain a critical view of the field with a view to judge not only what is technically feasible, but also what is worth doing.

CV monitoring is a field that has rarely stood still in the past century. New technology displaces the most promising of the old approaches, only for developments in other fields to make the old ideas relevant again in a different context. If I am to offer any advice to others who would look to this thesis for direction, all I can offer is to maintain an open mind and to not dismiss anything out of hand.

6 Bibliography

Alastruey, J., Charlton, P. H., Bikia, V., Paliakaite, B., Hametner, B., Bruno, R. M., Mulder, M. P., Vennin, S., Piskin, S., Khir, A. W., Guala, A., Mayer, C. C., Mynard, J., Hughes, A. D., Segers, P., & Westerhof, B. E. (2023). Arterial pulse wave modeling and analysis for vascular-age studies: A review from VascAgeNet. *American Journal of Physiology-Heart and Circulatory Physiology*, *325*(1), H1–H29. https://doi.org/10.1152/ajpheart.00705.2022

Alexandre Laurin & Jona Joachim. (2017). *BP_annotate* (2.2.0) [MATLAB; MATLAB]. École Polytechnique; MATLAB Central File Exchange. https://se.mathworks.com/matlabcentral/fileexchange/60172-bp_annotate

Allen, J. (2007). Photoplethysmography and its application in clinical physiological measurement. *Physiological Measurement*, *28*(3), R1. https://doi.org/10.1088/0967-3334/28/3/R01

Ashouri, H., Hersek, S., & Inan, O. T. (2018). Universal Pre-Ejection Period Estimation Using Seismocardiography: Quantifying the Effects of Sensor Placement and Regression Algorithms. *IEEE Sensors Journal*, *18*(4), 1665–1674. https://doi.org/10.1109/JSEN.2017.2787628

Auflem, M. (2023). *Development of Medical Training Equipment through Prototyping, Wayfaring, and Triple Loop Learning: Industrial Research at Laerdal Medical* [Doctoral thesis, NTNU]. NTNU Open. https://ntnuopen.ntnu.no/ntnu-xmlui/handle/11250/3072023

Avolio, A. (2023). The reality and serendipity of cuffless blood pressure monitoring. *Hypertension Research*, *46*(6), Article 6. https://doi.org/10.1038/s41440-023-01269-z

Barvik, D., Cerny, M., Penhaker, M., & Noury, N. (2022). Noninvasive Continuous Blood Pressure Estimation From Pulse Transit Time: A Review of the Calibration Models. *IEEE Reviews in Biomedical Engineering*, *15*, 138–151. https://doi.org/10.1109/RBME.2021.3109643

Borzage, M., Heidari, K., Chavez, T., Seri, I., Wood, J. C., & Blüml, S. (2017). Measuring Stroke Volume: Impedance Cardiography vs Phase-Contrast Magnetic Resonance Imaging. *American Journal of Critical Care*, *26*(5), 408–415. https://doi.org/10.4037/ajcc2017488

Bouzid, Z., Al-Zaiti, S. S., Bond, R., & Sejdić, E. (2022). Remote and wearable ECG devices with diagnostic abilities in adults: A state-of-the-science scoping review. *Heart Rhythm*, *19*(7), 1192–1201. https://doi.org/10.1016/j.hrthm.2022.02.030

Brede, J. R., Lafrenz, T., Krüger, A. J., Søvik, E., Steffensen, T. L., Kriesi, C., Steinert, M., & Klepstad, P. (2019). Resuscitative endovascular balloon occlusion of the aorta (REBOA) in non-traumatic out-of-hospital cardiac arrest: Evaluation of an educational programme. *BMJ Open*, *9*(5), e027980. https://doi.org/10.1136/bmjopen-2018-027980

Brickwood, K.-J., Watson, G., O'Brien, J., & Williams, A. D. (2019). Consumer-Based Wearable Activity Trackers Increase Physical Activity Participation: Systematic Review and Meta-Analysis. *JMIR MHealth and UHealth*, *7*(4), e11819. https://doi.org/10.2196/11819

Campo, D., Khettab, H., Yu, R., Genain, N., Edouard, P., Buard, N., & Boutouyrie, P. (2017). Measurement of Aortic Pulse Wave Velocity With a Connected Bathroom Scale. *American Journal of Hypertension*, *30*(9), 876–883. https://doi.org/10.1093/ajh/hpx059

Cecelja, M., & Chowienczyk, P. (2009). Dissociation of Aortic Pulse Wave Velocity With Risk Factors for Cardiovascular Disease Other Than Hypertension. *Hypertension*, *54*(6), 1328–1336. https://doi.org/10.1161/HYPERTENSIONAHA.109.137653

Chandrasekhar, A., Yavarimanesh, M., Natarajan, K., Hahn, J.-O., & Mukkamala, R. (2020). PPG Sensor Contact Pressure Should Be Taken Into Account for Cuff-Less Blood Pressure Measurement. *IEEE Transactions on Biomedical Engineering*, *67*(11), 3134–3140. https://doi.org/10.1109/TBME.2020.2976989

Charlton, P. H., Bonnici, T., Tarassenko, L., Alastruey, J., Clifton, D. A., Beale, R., & Watkinson, P. J. (2017). Extraction of respiratory signals from the electrocardiogram and photoplethysmogram: Technical and physiological determinants. *Physiological Measurement*, *38*(5), 669–690. https://doi.org/10.1088/1361-6579/aa670e

Charlton, P. H., Bonnici, T., Tarassenko, L., Clifton, D. A., Beale, R., & Watkinson, P. J. (2016). An assessment of algorithms to estimate respiratory rate from the electrocardiogram and photoplethysmogram. *Physiological Measurement*, *37*(4), 610–626. https://doi.org/10.1088/0967-3334/37/4/610

Charlton, P. H., Kyriacou, P. A., Mant, J., Marozas, V., Chowienczyk, P., & Alastruey, J. (2022). Wearable Photoplethysmography for Cardiovascular Monitoring. *Proceedings of the IEEE*, *110*(3), 355–381. https://doi.org/10.1109/JPROC.2022.3149785

Charlton, P. H., & Marozas, V. (2022). 12—Wearable photoplethysmography devices. In J. Allen & P. Kyriacou (Eds.), *Photoplethysmography* (pp. 401–439). Academic Press. https://doi.org/10.1016/B978-0-12-823374-0.00011-6

Chen, C. H., Nevo, E., Fetics, B., Pak, P. H., Yin, F. C., Maughan, W. L., & Kass, D. A. (1997). Estimation of central aortic pressure waveform by mathematical transformation of radial tonometry pressure. Validation of generalized transfer function. *Circulation*, *95*(7), 1827–1836. https://doi.org/10.1161/01.cir.95.7.1827

Chen, W., Kobayashi, T., Ichikawa, S., Takeuchi, Y., & Togawa, T. (2000). Continuous estimation of systolic blood pressure using the pulse arrival time and intermittent calibration. *Medical and Biological Engineering and Computing*, *38*(5), 569–574. https://doi.org/10.1007/BF02345755

Choudhury, M. I., Singh, P., Juneja, R., Tuli, S., Deepak, K. K., Prasad, A., & Roy, S. (2018). A Novel Modular Tonometry-Based Device to Measure Pulse Pressure Waveforms in Radial Artery. *Journal of Medical Devices*, *12*(011011). https://doi.org/10.1115/1.4039010

Davies, J. I., & Struthers, A. D. (2003). Pulse wave analysis and pulse wave velocity: A critical review of their strengths and weaknesses. *Journal of Hypertension*, *21*(3), 463.

Djupedal, H., Nøstdahl, T., Hisdal, J., Landsverk, S. A., & Høiseth, L. Ø. (2022). Effects of experimental hypovolemia and pain on pre-ejection period and pulse transit time in healthy volunteers. *Physiological Reports*, *10*(12), e15355. https://doi.org/10.14814/phy2.15355

Enayati, M. (2019). *Data-driven methods for analyzing ballistocardiograms in longitudinal cardiovascular monitoring* [Thesis, University of Missouri--Columbia]. https://mospace.umsystem.edu/xmlui/handle/10355/72208

Etemadi, M., & Inan, O. T. (2018). Wearable ballistocardiogram and seismocardiogram systems for health and performance. *Journal of Applied Physiology*, *124*(2), 452–461. https://doi.org/10.1152/japplphysiol.00298.2017

Fetics, B., Nevo, E., Chen, C. H., & Kass, D. A. (1999). Parametric model derivation of transfer function for noninvasive estimation of aortic pressure by radial tonometry. *IEEE Transactions on Bio-Medical Engineering*, *46*(6), 698–706. https://doi.org/10.1109/10.764946

Fine, J., Branan, K. L., Rodriguez, A. J., Boonya-ananta, T., Ajmal, Ramella-Roman, J. C., McShane, M. J., & Coté, G. L. (2021). Sources of Inaccuracy in Photoplethysmography for Continuous Cardiovascular Monitoring. *Biosensors*, *11*(4), Article 4. https://doi.org/10.3390/bios11040126

Finnegan, E., Davidson, S., Harford, M., Jorge, J., Watkinson, P., Young, D., Tarassenko, L., & Villarroel, M. (2021). Pulse arrival time as a surrogate of blood pressure. *Scientific Reports*, *11*(1), 22767. https://doi.org/10.1038/s41598-021-01358-4

Fraden, J. (2016). *Handbook of Modern Sensors: Physics, Designs, and Applications*. Springer International Publishing. https://doi.org/10.1007/978-3-319-19303-8

Fu, Y., Zhao, J., Dong, Y., & Wang, X. (2020). Dry Electrodes for Human Bioelectrical Signal Monitoring. *Sensors*, *20*(13), Article 13. https://doi.org/10.3390/s20133651

Gallagher, D., Adji, A., & O'Rourke, M. F. (2004). Validation of the transfer function technique for generating central from peripheral upper limb pressure waveform. *American Journal of Hypertension*, *17*(11), 1059–1067. https://doi.org/10.1016/j.amjhyper.2004.05.027

Ganti, V. G., Carek, A. M., Nevius, B. N., Heller, J. A., Etemadi, M., & Inan, O. T. (2021). Wearable Cuff-Less Blood Pressure Estimation at Home via Pulse Transit Time. *IEEE Journal of Biomedical and Health Informatics*, *25*(6), 1926–1937. https://doi.org/10.1109/JBHI.2020.3021532

Gao, M., Rose, W. C., Fetics, B., Kass, D. A., Chen, C.-H., & Mukkamala, R. (2016). A Simple Adaptive Transfer Function for Deriving the Central Blood Pressure Waveform from a Radial Blood Pressure Waveform. *Scientific Reports*, *6*(1), 33230. https://doi.org/10.1038/srep33230

Geddes, L. A. (2013). *Handbook of Blood Pressure Measurement*. Springer Science & Business Media.

Geddes, L. A., Voelz, M. H., Babbs, C. F., Bourland, J. D., & Tacker, W. A. (1981). Pulse Transit Time as an Indicator of Arterial Blood Pressure. *Psychophysiology*, *18*(1), 71–74. https://doi.org/10.1111/j.1469-8986.1981.tb01545.x

Gemperle, F., Kasabach, C., Stivoric, J., Bauer, M., & Martin, R. (1998). Design for wearability. *Digest of Papers. Second International Symposium on Wearable Computers (Cat. No.98EX215)*, 116–122. https://doi.org/10.1109/ISWC.1998.729537

Gilliam, F. R., Ciesielski, R., Shahinyan, K., Shakya, P., Cunsolo, J., Panchal, J. M., Król-Józaga, B., Król, M., Kierul, O., Bridges, C., Shen, C., Waldman, C. E., Ring, M., Szepieniec, T., Barnacka, A., & Bhavnani, S. P. (2022). In-ear infrasonic hemodynography with a digital health device for cardiovascular monitoring using the human audiome. *Npj Digital Medicine*, *5*(1), Article 1. https://doi.org/10.1038/s41746-022-00725-3

Gjerde, S. G., Steffensen, T. L., Vestad, H. N., & Steinert, M. (2022). Windows to the Sole: Prototyping Soft Sensors for Wearable Ballistocardiography. *2022 IEEE-EMBS International Conference on Wearable and Implantable Body Sensor Networks (BSN)*, 1–4. https://doi.org/10.1109/BSN56160.2022.9928472

Han, M., Lee, Y.-R., Park, T., Ihm, S.-H., Pyun, W. B., Burkard, T., Cho, M.-C., Camafort, M., Yang, E., Stergiou, G. S., Lee, H. Y., & Seo, J.-M. (2023). Feasibility and measurement stability of smartwatch-based cuffless blood pressure monitoring: A real-world prospective observational study. *Hypertension Research*, *46*(4), Article 4. https://doi.org/10.1038/s41440-023-01215-z

Heimark, S., Eitzen, I., Vianello, I., Bøtker-Rasmussen, K. G., Mamen, A., Hoel Rindal, O. M., Waldum-Grevbo, B., Sandbakk, Ø., & Seeberg, T. M. (2022). Blood Pressure Response

and Pulse Arrival Time During Exercise Testing in Well-Trained Individuals. *Frontiers in Physiology*, *13*. https://www.frontiersin.org/articles/10.3389/fphys.2022.863855

Hoffmann, B., Dehkordi, P., Khosrow-Khavar, F., Goswami, N., Blaber, A. P., & Tavakolian, K. (2022). Mechanical deconditioning of the heart due to long-term bed rest as observed on seismocardiogram morphology. *Npj Microgravity*, *8*(1), Article 1. https://doi.org/10.1038/s41526-022-00206-7

Hu, H., Huang, H., Li, M., Gao, X., Yin, L., Qi, R., Wu, R. S., Chen, X., Ma, Y., Shi, K., Li, C., Maus, T. M., Huang, B., Lu, C., Lin, M., Zhou, S., Lou, Z., Gu, Y., Chen, Y., … Xu, S. (2023). A wearable cardiac ultrasound imager. *Nature*, *613*(7945), Article 7945. https://doi.org/10.1038/s41586-022-05498-z

Huhn, S., Axt, M., Gunga, H.-C., Maggioni, M. A., Munga, S., Obor, D., Sié, A., Boudo, V., Bunker, A., Sauerborn, R., Bärnighausen, T., & Barteit, S. (2022). The Impact of Wearable Technologies in Health Research: Scoping Review. *JMIR MHealth and UHealth*, *10*(1), e34384. https://doi.org/10.2196/34384

IEEE Standard for Wearable Cuffless Blood Pressure Measuring Devices. (2014). *IEEE Std 1708-2014*, 1–38. https://doi.org/10.1109/IEEESTD.2014.6882122

Inan, O. T., Etemadi, M., Paloma, A., Giovangrandi, L., & Kovacs, G. T. A. (2009). Non-invasive cardiac output trending during exercise recovery on a bathroom-scale-based ballistocardiograph. *Physiological Measurement*, *30*(3), 261. https://doi.org/10.1088/0967-3334/30/3/003

Inan, O. T., Migeotte, P.-F., Park, K.-S., Etemadi, M., Tavakolian, K., Casanella, R., Zanetti, J., Tank, J., Funtova, I., Prisk, G. K., & Di Rienzo, M. (2015). Ballistocardiography and Seismocardiography: A Review of Recent Advances. *IEEE Journal of Biomedical and Health Informatics*, *19*(4), 1414–1427. https://doi.org/10.1109/JBHI.2014.2361732

Isakadze, N., & Martin, S. S. (2020). How useful is the smartwatch ECG? *Trends in Cardiovascular Medicine*, *30*(7), 442–448. https://doi.org/10.1016/j.tcm.2019.10.010

Julien, C. (2006). The enigma of Mayer waves: Facts and models. *Cardiovascular Research*, *70*(1), 12–21. https://doi.org/10.1016/j.cardiores.2005.11.008

Jung, H., Kimball, J. P., Receveur, T., Agdeppa, E. D., & Inan, O. T. (2021). Accurate Ballistocardiogram Based Heart Rate Estimation Using an Array of Load Cells in a Hospital Bed. *IEEE Journal of Biomedical and Health Informatics*, *25*(9), 3373–3383. https://doi.org/10.1109/JBHI.2021.3066885

Jung, H., Kimball, J. P., Receveur, T., Gazi, A. H., Agdeppa, E. D., & Inan, O. T. (2022). Estimation of Tidal Volume Using Load Cells on a Hospital Bed. *IEEE Journal of Biomedical and Health Informatics*, *26*(7), 3330–3341. https://doi.org/10.1109/JBHI.2022.3141209

Kaisti, M., Panula, T., Leppänen, J., Punkkinen, R., Jafari Tadi, M., Vasankari, T., Jaakkola, S., Kiviniemi, T., Airaksinen, J., Kostiainen, P., Meriheinä, U., Koivisto, T., & Pänkäälä, M. (2019). Clinical assessment of a non-invasive wearable MEMS pressure sensor array for monitoring of arterial pulse waveform, heart rate and detection of atrial fibrillation. *Npj Digital Medicine*, *2*(1), Article 1. https://doi.org/10.1038/s41746-019-0117-x

Kamga, P., Mostafa, R., & Zafar, S. (2022). The Use of Wearable ECG Devices in the Clinical Setting: A Review. *Current Emergency and Hospital Medicine Reports*, *10*(3), 67–72. https://doi.org/10.1007/s40138-022-00248-x

Karamanoglu, M., O'Rourke, M. F., Avolio, A. P., & Kelly, R. P. (1993). An analysis of the relationship between central aortic and peripheral upper limb pressure waves in man. *European Heart Journal*, *14*(2), 160–167. https://doi.org/10.1093/eurheartj/14.2.160

Kim, C.-S., Carek, A. M., Mukkamala, R., Inan, O. T., & Hahn, J.-O. (2015). Ballistocardiogram as Proximal Timing Reference for Pulse Transit Time Measurement: Potential for Cuffless Blood Pressure Monitoring. *IEEE Transactions on Biomedical Engineering*, *62*(11), 2657–2664. https://doi.org/10.1109/TBME.2015.2440291

Kireev, D., Sel, K., Ibrahim, B., Kumar, N., Akbari, A., Jafari, R., & Akinwande, D. (2022). Continuous cuffless monitoring of arterial blood pressure via graphene bioimpedance tattoos. *Nature Nanotechnology*, *17*(8), Article 8. https://doi.org/10.1038/s41565-022-01145-w

Kitt, J., Fox, R., Tucker, K. L., & McManus, R. J. (2019). New Approaches in Hypertension Management: A Review of Current and Developing Technologies and Their Potential

Impact on Hypertension Care. *Current Hypertension Reports*, *21*(6), 44. https://doi.org/10.1007/s11906-019-0949-4

Kohara, K., Tabara, Y., Oshiumi, A., Miyawaki, Y., Kobayashi, T., & Miki, T. (2005). Radial augmentation index: A useful and easily obtainable parameter for vascular aging. *American Journal of Hypertension*, *18*(S1), 11S-14S. https://doi.org/10.1016/j.amjhyper.2004.10.010

Krogh, M. R., Halvorsen, P. S., Grymyr, O.-J. H. N., Bergsland, J., Elle, O. J., Fosse, E., & W. Remme, E. (2021). Continuous Estimation of Acute Changes in Preload Using Epicardially Attached Accelerometers. *IEEE Transactions on Biomedical Engineering*, *68*(7), 2067–2075. https://doi.org/10.1109/TBME.2020.3020358

Kurylyak, Y., Lamonaca, F., & Grimaldi, D. (2013). A Neural Network-based method for continuous blood pressure estimation from a PPG signal. *2013 IEEE International Instrumentation and Measurement Technology Conference (I2MTC)*, 280–283. https://doi.org/10.1109/I2MTC.2013.6555424

Kyriacou, P. A., & Chatterjee, S. (2022). 2—The origin of photoplethysmography. In J. Allen & P. Kyriacou (Eds.), *Photoplethysmography* (pp. 17–43). Academic Press. https://doi.org/10.1016/B978-0-12-823374-0.00004-9

Landry, C., Hedge, E. T., Hughson, R. L., Peterson, S. D., & Arami, A. (2022). Cuffless Blood Pressure Estimation During Moderate- and Heavy-Intensity Exercise Using Wearable ECG and PPG. *IEEE Journal of Biomedical and Health Informatics*, *26*(12), 5942–5952. https://doi.org/10.1109/JBHI.2022.3207947

Laughlin, M. H. (1999). Cardiovascular response to exercise. *Advances in Physiology Education*, *277*(6), S244. https://doi.org/10.1152/advances.1999.277.6.S244

Leitner, J., Chiang, P.-H., & Dey, S. (2022). Personalized Blood Pressure Estimation Using Photoplethysmography: A Transfer Learning Approach. *IEEE Journal of Biomedical and Health Informatics*, *26*(1), 218–228. https://doi.org/10.1109/JBHI.2021.3085526

Lin, W.-Y., Chou, W.-C., Chang, P.-C., Chou, C.-C., Wen, M.-S., Ho, M.-Y., Lee, W.-C., Hsieh, M.-J., Lin, C.-C., Tsai, T.-H., & Lee, M.-Y. (2018). Identification of Location Specific Feature Points in a Cardiac Cycle Using a Novel Seismocardiogram Spectrum System.

IEEE Journal of Biomedical and Health Informatics, *22*(2), 442–449. https://doi.org/10.1109/JBHI.2016.2620496

Liu, Q., Yan, B. P., Yu, C.-M., Zhang, Y.-T., & Poon, C. C. Y. (2014). Attenuation of Systolic Blood Pressure and Pulse Transit Time Hysteresis During Exercise and Recovery in Cardiovascular Patients. *IEEE Transactions on Biomedical Engineering*, *61*(2), 346–352. https://doi.org/10.1109/TBME.2013.2286998

Lu, L., Zhang, J., Xie, Y., Gao, F., Xu, S., Wu, X., & Ye, Z. (2020). Wearable Health Devices in Health Care: Narrative Systematic Review. *JMIR MHealth and UHealth*, *8*(11), e18907. https://doi.org/10.2196/18907

Lydon, K., Su, B. Y., Rosales, L., Enayati, M., Ho, K. C., Rantz, M., & Skubic, M. (2015). Robust heartbeat detection from in-home ballistocardiogram signals of older adults using a bed sensor. *2015 37th Annual International Conference of the IEEE Engineering in Medicine and Biology Society (EMBC)*, 7175–7179. https://doi.org/10.1109/EMBC.2015.7320047

Ma, L.-Y., & Soin, N. (2022). Recent Progress in Printed Physical Sensing Electronics for Wearable Health-Monitoring Devices: A Review. *IEEE Sensors Journal*, *22*(5), 3844–3859. https://doi.org/10.1109/JSEN.2022.3142328

Maheshwari, K., Nathanson, B. H., Munson, S. H., Khangulov, V., Stevens, M., Badani, H., Khanna, A. K., & Sessler, D. I. (2018). The relationship between ICU hypotension and in-hospital mortality and morbidity in septic patients. *Intensive Care Medicine*, *44*(6), 857–867. https://doi.org/10.1007/s00134-018-5218-5

Malmivuo, J., & Plonsey, R. (1995). *Bioelectromagnetism: Principles and Applications of Bioelectric and Biomagnetic Fields*. Oxford University Press.

Marazzi, N. M., Guidoboni, G., Zaid, M., Sala, L., Ahmad, S., Despins, L., Popescu, M., Skubic, M., & Keller, J. (2022). Combining Physiology-Based Modeling and Evolutionary Algorithms for Personalized, Noninvasive Cardiovascular Assessment Based on Electrocardiography and Ballistocardiography. *Frontiers in Physiology*, *12*. https://www.frontiersin.org/articles/10.3389/fphys.2021.739035

Martin, S. L.-O., Carek, A. M., Kim, C.-S., Ashouri, H., Inan, O. T., Hahn, J.-O., & Mukkamala, R. (2016). Weighing Scale-Based Pulse Transit Time is a Superior Marker of Blood Pressure than Conventional Pulse Arrival Time. *Scientific Reports*, *6*, 39273. https://doi.org/10.1038/srep39273

Mieloszyk, R., Twede, H., Lester, J., Wander, J., Basu, S., Cohn, G., Smith, G., Morris, D., Gupta, S., Tan, D., Villar, N., Wolf, M., Malladi, S., Mickelson, M., Ryan, L., Kim, L., Kepple, J., Kirchner, S., Wampler, E., … Saponas, T. S. (2022). A Comparison of Wearable Tonometry, Photoplethysmography, and Electrocardiography for Cuffless Measurement of Blood Pressure in an Ambulatory Setting. *IEEE Journal of Biomedical and Health Informatics*, *26*(7), 2864–2875. https://doi.org/10.1109/JBHI.2022.3153259

Miyai, N., Arita, M., Miyashita, K., Morioka, I., Shiraishi, T., & Nishio, I. (2002). Blood Pressure Response to Heart Rate During Exercise Test and Risk of Future Hypertension. *Hypertension*, *39*(3), 761–766. https://doi.org/10.1161/hy0302.105777

Mukkamala, R., Hahn, J.-O., Inan, O. T., Mestha, L. K., Kim, C.-S., Töreyin, H., & Kyal, S. (2015). Toward Ubiquitous Blood Pressure Monitoring via Pulse Transit Time: Theory and Practice. *IEEE Transactions on Biomedical Engineering*, *62*(8), 1879–1901. https://doi.org/10.1109/TBME.2015.2441951

Mukkamala, R., Stergiou, G. S., & Avolio, A. P. (2022). Cuffless Blood Pressure Measurement. *Annual Review of Biomedical Engineering*, *24*(1), 203–230. https://doi.org/10.1146/annurev-bioeng-110220-014644

Nichols, W. W., O'Rourke, M. F., & Vlachopoulos, C. (2011). *McDonald's Blood Flow in Arteries. Theoretical, Experimental and Clinical Principles* (6th ed.). Hodder Arnold.

Nowara, E. M., McDuff, D., & Veeraraghavan, A. (2020). *A Meta-Analysis of the Impact of Skin Tone and Gender on Non-Contact Photoplethysmography Measurements*. 284–285. https://openaccess.thecvf.com/content_CVPRW_2020/html/w19/Nowara_A_Meta-Analysis_of_the_Impact_of_Skin_Tone_and_Gender_CVPRW_2020_paper.html

Orphanidou, C., Bonnici, T., Charlton, P., Clifton, D., Vallance, D., & Tarassenko, L. (2015). Signal-Quality Indices for the Electrocardiogram and Photoplethysmogram:

Derivation and Applications to Wireless Monitoring. *IEEE Journal of Biomedical and Health Informatics*, *19*(3), 832–838. https://doi.org/10.1109/JBHI.2014.2338351

Ortega, R., Connor, C., Kotova, F., Deng, W., & Lacerra, C. (2017). Use of Pressure Transducers. *New England Journal of Medicine*, *376*(14), e26. https://doi.org/10.1056/NEJMvcm1513613

Pan, J., & Tompkins, W. J. (1985). A Real-Time QRS Detection Algorithm. *IEEE Transactions on Biomedical Engineering*, *BME-32*(3), 230–236. https://doi.org/10.1109/TBME.1985.325532

Park, J.-H., Jang, D.-G., Park, J. W., & Youm, S.-K. (2015). Wearable Sensing of In-Ear Pressure for Heart Rate Monitoring with a Piezoelectric Sensor. *Sensors*, *15*(9), Article 9. https://doi.org/10.3390/s150923402

Piwek, L., Ellis, D. A., Andrews, S., & Joinson, A. (2016). The Rise of Consumer Health Wearables: Promises and Barriers. *PLOS Medicine*, *13*(2), e1001953. https://doi.org/10.1371/journal.pmed.1001953

Rosales, L., Su, B. Y., Skubic, M., & Ho, K. C. (2017). Heart rate monitoring using hydraulic bed sensor ballistocardiogram 1. *Journal of Ambient Intelligence and Smart Environments*, *9*(2), 193–207. https://doi.org/10.3233/AIS-170423

Sana, F., Isselbacher, E. M., Singh, J. P., Heist, E. K., Pathik, B., & Armoundas, A. A. (2020). Wearable Devices for Ambulatory Cardiac Monitoring: JACC State-of-the-Art Review. *Journal of the American College of Cardiology*, *75*(13), 1582–1592. https://doi.org/10.1016/j.jacc.2020.01.046

Saugel, B., Kouz, K., Meidert, A. S., Schulte-Uentrop, L., & Romagnoli, S. (2020). How to measure blood pressure using an arterial catheter: A systematic 5-step approach. *Critical Care*, *24*(1), 172. https://doi.org/10.1186/s13054-020-02859-w

Sel, K., Osman, D., Huerta, N., Edgar, A., Pettigrew, R. I., & Jafari, R. (2023). Continuous cuffless blood pressure monitoring with a wearable ring bioimpedance device. *Npj Digital Medicine*, *6*(1), Article 1. https://doi.org/10.1038/s41746-023-00796-w

Sessler, D. I., & Saugel, B. (2019). Beyond 'failure to rescue': The time has come for continuous ward monitoring. *British Journal of Anaesthesia*, *122*(3), 304–306. https://doi.org/10.1016/j.bja.2018.12.003

Shandhi, M. M. H., Bartlett, W. H., Heller, J. A., Etemadi, M., Young, A., Plötz, T., & Inan, O. T. (2021). Estimation of Instantaneous Oxygen Uptake During Exercise and Daily Activities Using a Wearable Cardio-Electromechanical and Environmental Sensor. *IEEE Journal of Biomedical and Health Informatics*, *25*(3), 634–646. https://doi.org/10.1109/JBHI.2020.3009903

Shandhi, M. M. H., Fan, J., Heller, J., Etemadi, M., Klein, L., & Inan, O. (2022). Estimation of Changes in Intracardiac Hemodynamics Using Wearable Seismocardiography and Machine Learning in Patients with Heart Failure: A Feasibility Study. *IEEE Transactions on Biomedical Engineering*, 1–1. https://doi.org/10.1109/TBME.2022.3147066

Sharma, P., Imtiaz, S. A., & Rodriguez-Villegas, E. (2019). Acoustic Sensing as a Novel Wearable Approach for Cardiac Monitoring at the Wrist. *Scientific Reports*, *9*(1), Article 1. https://doi.org/10.1038/s41598-019-55599-5

Sharma, P., & Rodriguez-Villegas, E. (2021). Acoustic Sensing as a Novel Wearable Approach for Heart Rate Variability Monitoring at the Wrist. *IEEE Transactions on Instrumentation and Measurement*, *70*, 1–12. https://doi.org/10.1109/TIM.2021.3088422

Sharman, J. E., Lim, R., Qasem, A. M., Coombes, J. S., Burgess, M. I., Franco, J., Garrahy, P., Wilkinson, I. B., & Marwick, T. H. (2006). Validation of a Generalized Transfer Function to Noninvasively Derive Central Blood Pressure During Exercise. *Hypertension*, *47*(6), 1203–1208. https://doi.org/10.1161/01.HYP.0000223013.60612.72

Shih, Y.-T., Cheng, H.-M., Sung, S.-H., Hu, W.-C., & Chen, C.-H. (2014). Application of the N-Point Moving Average Method for Brachial Pressure Waveform–Derived Estimation of Central Aortic Systolic Pressure. *Hypertension*, *63*(4), 865–870. https://doi.org/10.1161/HYPERTENSIONAHA.113.02229

Shimura, K., Hori, M., Dohi, T., & Takao, H. (2018). The Calibration Method for Blood Pressure Pulse Wave Measurement Based on Arterial Tonometry Method. *2018 40th Annual*

International Conference of the IEEE Engineering in Medicine and Biology Society (EMBC), 1–4. https://doi.org/10.1109/EMBC.2018.8513054

Shin, S., Mousavi, A. S., Lyle, S., Jang, E., Yousefian, P., Mukkamala, R., Jang, D.-G., Kwon, U. K., Kim, Y. H., & Hahn, J.-O. (2022). Posture-Dependent Variability in Wrist Ballistocardiogram-Photoplethysmogram Pulse Transit Time: Implication to Cuff-Less Blood Pressure Tracking. *IEEE Transactions on Biomedical Engineering*, *69*(1), 347–355. https://doi.org/10.1109/TBME.2021.3094200

Shin, S., Yousefian, P., Mousavi, A. S., Kim, C.-S., Mukkamala, R., Jang, D.-G., Ko, B.-H., Lee, J., Kwon, U.-K., Kim, Y. H., & Hahn, J.-O. (2021). A Unified Approach to Wearable Ballistocardiogram Gating and Wave Localization. *IEEE Transactions on Biomedical Engineering*, *68*(4), 1115–1122. https://doi.org/10.1109/TBME.2020.3010864

Singh, P., Choudhury, M. I., Roy, S., & Prasad, A. (2017). Computational study to investigate effect of tonometer geometry and patient-specific variability on radial artery tonometry. *Journal of Biomechanics*, *58*, 105–113. https://doi.org/10.1016/j.jbiomech.2017.04.023

Sjöman, H. (2019). *Insights for Prototyping for the Industrial Internet—Iterative Prototyping Loops of Connected Sensor Platforms* [Doctoral thesis, NTNU]. https://ntnuopen.ntnu.no/ntnu-xmlui/handle/11250/2611194

Solberg, F. S., Kohtala, S., Vestad, H., & Steinert, M. (2019). A Combined Photoplethysmography and Force Sensor Prototype for Improved Pulse Waveform Analysis. *2019 IEEE SENSORS*, 1–4. https://doi.org/10.1109/SENSORS43011.2019.8956487

Sørensen, K., Schmidt, S. E., Jensen, A. S., Søgaard, P., & Struijk, J. J. (2018). Definition of Fiducial Points in the Normal Seismocardiogram. *Scientific Reports*, *8*(1), 15455. https://doi.org/10.1038/s41598-018-33675-6

Starr, I. (1955). Studies made by simulating systole at necropsy. VI. Estimation of cardiac stroke volume from the ballistocardiogram. *Journal of Applied Physiology*, *8*(3), 315–329. https://doi.org/10.1152/jappl.1955.8.3.315

Starr, I., Rawson, A. J., Schroeder, H. A., & Joseph, N. R. (1939). Studies on the estimation of cardiac ouptut in man, and of abnormalities in cardiac function, from the heart's recoil

and the blood's impacts; the ballistocardiogram. *American Journal of Physiology-Legacy Content*, *127*(1), 1–28. https://doi.org/10.1152/ajplegacy.1939.127.1.1

Steffensen, T. L., Bartnes, B., Fuglstad, M. L., Auflem, M., & Steinert, M. (Submitted). Playing the pipes: Acoustic sensing and machine learning for performance feedback during endotracheal intubation simulation. *Frontiers in Robotics and AI*.

Steffensen, T. L., Schjerven, F. E., Flade, H. M., Kirkeby-Garstad, I., Ingeström, E., Solberg, F. S., & Steinert, M. (2023). Wrist ballistocardiography and invasively recorded blood pressure in healthy volunteers during reclining bike exercise. *Frontiers in Physiology*, *14*. https://www.frontiersin.org/articles/10.3389/fphys.2023.1189732

Stergiou, G. S., Avolio, A. P., Palatini, P., Kyriakoulis, K. G., Schutte, A. E., Mieke, S., Kollias, A., Parati, G., Asmar, R., Pantazis, N., Stamoulopoulos, A., Asayama, K., Castiglioni, P., De La Sierra, A., Hahn, J.-O., Kario, K., McManus, R. J., Myers, M., Ohkubo, T., … Mukkamala, R. (2023). European Society of Hypertension recommendations for the validation of cuffless blood pressure measuring devices: European Society of Hypertension Working Group on Blood Pressure Monitoring and Cardiovascular Variability. *Journal of Hypertension*. https://doi.org/10.1097/hjh.0000000000003483

Stergiou, G. S., Kollias, A., Zeniodi, M., Karpettas, N., & Ntineri, A. (2014). Home Blood Pressure Monitoring: Primary Role in Hypertension Management. *Current Hypertension Reports*, *16*(8), 462. https://doi.org/10.1007/s11906-014-0462-8

Stergiou, G. S., Mukkamala, R., Avolio, A., Kyriakoulis, K. G., Mieke, S., Murray, A., Parati, G., Schutte, A. E., Sharman, J. E., Asmar, R., McManus, R. J., Asayama, K., De La Sierra, A., Head, G., Kario, K., Kollias, A., Myers, M., Niiranen, T., Ohkubo, T., … Palatini, P. (2022). Cuffless blood pressure measuring devices: Review and statement by the European Society of Hypertension Working Group on Blood Pressure Monitoring and Cardiovascular Variability. *Journal of Hypertension*, *40*(8), 1449. https://doi.org/10.1097/HJH.0000000000003224

Stok, W. J., Westerhof, B. E., Guelen, I., & Karemaker, J. M. (2011). Aortic pressure wave reconstruction during exercise is improved by adaptive filtering: A pilot study. *Medical*

& Biological Engineering & Computing, *49*(8), 909–916. https://doi.org/10.1007/s11517-011-0795-2

Stok, W. J., Westerhof, B. E., & Karemaker, J. M. (2006). Changes in finger-aorta pressure transfer function during and after exercise. *Journal of Applied Physiology*, *101*(4), 1207–1214. https://doi.org/10.1152/japplphysiol.00876.2005

Stoner, L., Faulkner, J., Lowe, A., Lambrick, D. M., Young, J. M., Love, R., & Rowlands, D. S. (2014). Should the Augmentation Index be Normalized to Heart Rate? *Journal of Atherosclerosis and Thrombosis*, *21*(1), 11–16. https://doi.org/10.5551/jat.20008

Su, B. Y., Enayati, M., Ho, K. C., Skubic, M., Despins, L., Keller, J., Popescu, M., Guidoboni, G., & Rantz, M. (2019). Monitoring the Relative Blood Pressure Using a Hydraulic Bed Sensor System. *IEEE Transactions on Biomedical Engineering*, *66*(3), 740–748. https://doi.org/10.1109/TBME.2018.2855639

Thanassoulis, G., Lyass, A., Benjamin, E. J., Larson, M. G., Vita, J. A., Levy, D., Hamburg, N. M., Widlansky, M. E., O'Donnell, C. J., Mitchell, G. F., & Vasan, R. S. (2012). Relations of Exercise Blood Pressure Response to Cardiovascular Risk Factors and Vascular Function in the Framingham Heart Study. *Circulation*, *125*(23), 2836–2843. https://doi.org/10.1161/CIRCULATIONAHA.111.063933

Vestad, H. N. (2022). *On Fuzzy Front End Prototyping and Testing of Complex Sensor Problems* [Doctoral thesis, NTNU]. https://ntnuopen.ntnu.no/ntnu-xmlui/handle/11250/2987684

Wang, C., Chen, X., Wang, L., Makihata, M., Liu, H.-C., Zhou, T., & Zhao, X. (2022). Bioadhesive ultrasound for long-term continuous imaging of diverse organs. *Science*, *377*(6605), 517–523. https://doi.org/10.1126/science.abo2542

Wang, H., Naghavi, M., Allen, C., Barber, R. M., Bhutta, Z. A., Carter, A., Casey, D. C., Charlson, F. J., Chen, A. Z., Coates, M. M., Coggeshall, M., Dandona, L., Dicker, D. J., Erskine, H. E., Ferrari, A. J., Fitzmaurice, C., Foreman, K., Forouzanfar, M. H., Fraser, M. S., … Murray, C. J. L. (2016). Global, regional, and national life expectancy, all-cause mortality, and cause-specific mortality for 249 causes of death, 1980–2015: A systematic

analysis for the Global Burden of Disease Study 2015. *The Lancet*, *388*(10053), 1459–1544. https://doi.org/10.1016/S0140-6736(16)31012-1

Wang, W., Mohseni, P., Kilgore, K. L., & Najafizadeh, L. (2022). Cuff-Less Blood Pressure Estimation From Photoplethysmography via Visibility Graph and Transfer Learning. *IEEE Journal of Biomedical and Health Informatics*, *26*(5), 2075–2085. https://doi.org/10.1109/JBHI.2021.3128383

Wheeler, C. M., Patel, S., Waldman, C. E., Panchal, J., Sidhu, R. S., Krol, M., Ye, R., Szepieniec, T., Shakya, P., Gupta, S., Shahinyan, K., Barnacka, A., Engstrom, H., Southard, K., Daniel, M., Stinis, C., Romero, S., Bridges, C., & Bhavnani, S. (2021). Abstract 11669: "Hearing the Heart" - Validation of a Novel Digital Health Earbud Technology to Measure Cardiac Time Intervals Through Infrasonic Hemodynography. *Circulation*, *144*(Suppl_1), A11669–A11669. https://doi.org/10.1161/circ.144.suppl_1.11669

Wiens, A. D., Johnson, A., & Inan, O. T. (2017). Wearable Sensing of Cardiac Timing Intervals From Cardiogenic Limb Vibration Signals. *IEEE Sensors Journal*, *17*(5), 1463–1470. https://doi.org/10.1109/JSEN.2016.2643780

Williams, B., Lacy, P. S., Yan, P., Hwee, C.-N., Liang, C., & Ting, C.-M. (2011). Development and Validation of a Novel Method to Derive Central Aortic Systolic Pressure From the Radial Pressure Waveform Using an N-Point Moving Average Method. *Journal of the American College of Cardiology*, *57*(8), 951–961. https://doi.org/10.1016/j.jacc.2010.09.054

Wu, Z., & Huang, N. E. (2011). ENSEMBLE EMPIRICAL MODE DECOMPOSITION: A NOISE-ASSISTED DATA ANALYSIS METHOD. *Advances in Adaptive Data Analysis*. https://doi.org/10.1142/S1793536909000047

Xiao, H., Butlin, M., Qasem, A., Tan, I., Li, D., & Avolio, A. P. (2018). N-Point Moving Average: A Special Generalized Transfer Function Method for Estimation of Central Aortic Blood Pressure. *IEEE Transactions on Biomedical Engineering*, *65*(6), 1226–1234. https://doi.org/10.1109/TBME.2017.2710622

Yao, Y., Shandhi, M. M. H., Hahn, J.-O., Inan, O. T., Mukkamala, R., & Xu, L. (2022). *What Filter Passband Should be Applied to the Ballistocardiogram?* (SSRN Scholarly Paper 4142412). https://doi.org/10.2139/ssrn.4142412

Yousefian, P., Shin, S., Mousavi, A., Kim, C.-S., Mukkamala, R., Jang, D.-G., Ko, B.-H., Lee, J., Kwon, U. K., Kim, Y. H., & Hahn, J.-O. (2019). The Potential of Wearable Limb Ballistocardiogram in Blood Pressure Monitoring via Pulse Transit Time. *Scientific Reports*, *9*(1), 10666. https://doi.org/10.1038/s41598-019-46936-9

Yousefian, P., Shin, S., Mousavi, A. S., Tivay, A., Kim, C.-S., Mukkamala, R., Jang, D.-G., Ko, B. H., Lee, J., Kwon, U.-K., Kim, Y. H., & Hahn, J.-O. (2020). Pulse Transit Time-Pulse Wave Analysis Fusion Based on Wearable Wrist Ballistocardiogram for Cuff-Less Blood Pressure Trend Tracking. *IEEE Access*, *8*, 138077–138087. https://doi.org/10.1109/ACCESS.2020.3012384

Zeagler, C. (2017). Where to wear it: Functional, technical, and social considerations in on-body location for wearable technology 20 years of designing for wearability. *Proceedings of the 2017 ACM International Symposium on Wearable Computers*, 150–157. https://doi.org/10.1145/3123021.3123042

Zhang, G., Gao, M., Xu, D., Olivier, N. B., & Mukkamala, R. (2011). Pulse arrival time is not an adequate surrogate for pulse transit time as a marker of blood pressure. *Journal of Applied Physiology*, *111*(6), 1681–1686. https://doi.org/10.1152/japplphysiol.00980.2011

Appendix: Original Contributions

C1. Windows to the Sole: Prototyping Soft Sensors for Wearable Ballistocardiography

2022 IEEE-EMBS International Conference on Wearable and Implantable Body Sensor Networks (BSN)

Simon Gåseby Gjerde, Torjus Lines Steffensen, Håvard Vestad, and Martin Steinert

Windows to the Sole: Prototyping Soft Sensors for Wearable Ballistocardiography

Simon Gjerde[1], Torjus Steffensen[2], Håvard Vestad[1], and Martin Steinert[1]

[1] Department of Mechanical and Industrial Engineering,
Norwegian University of Science and Technology, Trondheim, Norway

[2] Department of Circulation and Medical Imaging,
Norwegian University of Science and Technology, Trondheim, Norway

Abstract— **Continuous measurement of cardiovascular parameters is important for monitoring cardiovascular health. Ballistocardiography is a noninvasive method of recording cardiovascular events. Here, we present a sensor system prototype for recording of the full-body ballistocardiogram in a wearable. An array of soft bladders in each sole are filled with water and connected to barometric pressure sensors. We demonstrate the use of the prototype to estimate the pulse transit time against continuous blood pressure in a validation experiment (n=14). Participants wore the sensor shoes while standing on a reference weight-scale. Simultaneous recordings were taken of the sole pressure arrays, finger-clip photoplethysmography, and continuous blood pressure via the volume-clamp method. Measurements were taken at rest, during cold-pressor intervention for 60 seconds, and 3 minutes following end of intervention. The waveform of the ballistocardiograms captured by the proposed sensor system corresponded well to the simultaneously collected waveforms from the reference weight-scale. Preliminary results from pulse-transit time estimates show inverse correlation to vasoconstriction-induced blood pressure increase, demonstrating the viability of the measurement. By demonstrating the use of the wearable system to compute a hemodynamic variable of interest to cardiovascular disease monitoring, we show the promise of shoes as a viable wearable sensor interface for cardiovascular monitoring.**

Keywords—wearable, ballistocardiography, prototype, pulse transit time

I. Introduction

Cardiovascular disease is a significant global healthcare burden. Continuous measurement of cardiovascular parameters through wearable sensors is of interest to facilitate early detection and to mitigate consequences. Ballistocardiography is the recording of the ballistic forces generated by the ejection of blood from the ventricle during the onset of systole. First rigorously investigated in the first half of the 20th century, as a non-invasive cardiovascular measurement the ballistocardiogram (BCG) has seen a modest resurgence as a convenient method of recording heart- and respiratory rates [1]. In combination with the photoplethysmogram (PPG), attempts have been made to define a robust estimate of the pulse wave velocity (PWV), a marker of arterial stiffness partially correlated with blood pressure, using BCG via multi-messenger time delay [2], [3].

Partly to deal with the notoriously noisy character of BCG signals, typical measurement scenarios have often relied on stationary measurements, for example via bathroom weighing-scales [4]. These "full-body" BCG setups rely on measuring force, for example via strain gauges or electret films. This has the advantage of a comparatively high signal-to-noise ratio (SNR). There is, however, a healthcare monitoring motivation for integrating BCG-based measurements in wearable devices, to which end attention has been focused on wrist- and earbud-based approaches built on accelerometry [2], [5]. These have the benefit of convenience and mobility but suffer a loss of signal quality in return. Here, we propose a "best of both worlds" solution: by integrating a series of high-sensitivity liquid pressure sensors in the sole of a shoe, we demonstrate that the BCG can be reliably recorded with reasonable quality. To exemplify a use case and verify the results, we estimate the pulse travel time (PTT) and compare it with concurrently recorded blood pressure. The PTT is estimated by combining the shoes with a commercial fingertip reflectance PPG sensor and using ensemble-averaged waveforms. To assess the ability of the sensors to record changes in hemodynamic state, 15 instrumented volunteers underwent a cold pressor test.

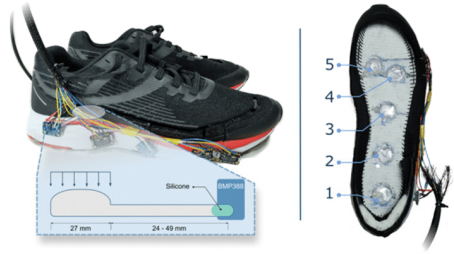

Fig. 1. Left: illustration of the sensor geometry and the shoe prototype used in this study. Right: the layout of the sensor array in each sole. In use, the array is covered by the insole.

II. Method

A. Device design

The prototype sensor device consists of a pair of off-the-shelf running shoes fitted with a special sole, containing an array of soft sensor units as shown in Fig. 1. A soft bladder filled with water is connected via a flexible tube to an atmospheric MEMS pressure sensor (BMP388, Bosch Sensortec GmbH, Germany) selected for its sample rate, precision, small size and previous familiarity in physiological measurement scenarios [6]. The bladders serve as a compliant interface between the sensing unit and the body and are further covered by the insole. The pressure sensor IC is de-lidded and a thin layer of silicone (Ecoflex 30, Smooth-On, USA) is applied in the end of the tube, creating a waterproof interface

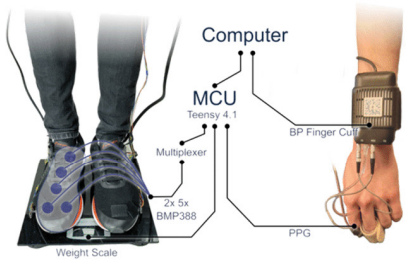

Fig. 2. Instrumentation during the experimental protocol. The soles, weigh scale, and finger PPG were sampled concurrently on the same MCU, and recorded to the same PC as the non-invasive continous blood pressure, which was recorded continuously throughout the experiment.

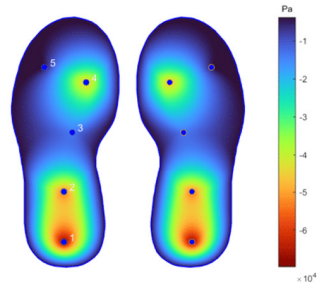

Fig. 3. Pressure heatmap interpolated over the soles during recording, showing relative pressure intensity. The sensors have been calibrated by subtracting an unloaded baseline.

to the sensor. The BMP388 sensors are connected via an I2C multiplexer to an MCU (Teensy 4.1, PJRC, USA).

The water-filled bladders have a diameter of 27 mm and an approximate surface area of 1550 mm^2. The bags are made from thermoplastic sheets (polyethylene and polyamide) cut into circles of two different diameters, 27 and 37 mm. The two sheets are then thermally welded together. Four to eight folds are introduced in the largest plastic sheet to achieve the same circumference on both of the sheets. This introduces a natural dome shape, simplifying the process of filling the bladder cavity. The hand-made nature of the sensors leads to some amount of inconsistency, but nominally each unit had a practical working range from 0 – 4 kg per 5.2 mm^2.

B. *Experimental protocol*

Fifteen participants (Table 1) were recruited for a verification study to assess the performance of the smart sole during a cold pressor test. Data collection was approved by the Norwegian Center for Research Data under reference 250185. All participants gave written consent.

TABLE I. PARTICIPANT DEMOGRAPHICS

	Female	***Male***
Gender	7	8
Age, years	23.5 (22-26)	25.5 (23-29)
Height, cm	171 (162-175)	182.5 (170.5-193)
Weight, kg	67 (53-93)	80 (64 – 86)
Shoe size, EU	39 (36-40)	44.5 (42.5 – 45)

Alongside the smart shoes, participants were equipped with a PPG sensor (PulseSensor, World Famous Electronics, USA) on their left index finger. Continuous blood pressure was recorded with a finger-clamp device (NIBP Nano INL382, ADInstruments, New Zealand). Participants stood on a modified bathroom weigh scale [7] serving as a reference signal throughout the measurement. Fig. 2 shows the experimental configuration schematically.

After reaching resting heart rate, reference measurements were taken, and the right hand was then immersed in an ice bath kept at 4° C up to the wrist and kept submerged for 1 minute. The resting measurement was repeated after 3 minutes. Data was processed using Python and Matlab r2022a (The Mathworks, Massachusetts, USA).

C. *Data processing and analysis*

One participant was discarded due to technical malfunction of the sampling MCU. The PPG, BCG shoes, and BCG scale were sampled simultaneously at 180 Hz. Blood pressure was sampled at 200 Hz on the same PC and logged to the same reference clock. The MCU and BP measurements were thus able to be synchronized post hoc. The PPG signal was bandpass filtered between 1 -15 Hz. A corresponding PPG signal was used by removing the corresponding samples from the PPG. The systolic blood pressure trend was smoothed with a third-order Savitsky-Golay filter.

The pressure and scale strain signals were segmented using the PPG signal. The PPG was annotated using a simple peak-finding method by locating local peaks with a spacing of at least 0.5s. The segments were checked automatically by comparing segment size for each segment, and the median segment size with segment sizes differing by more than 5% from the median were discarded. The annotation was verified manually by visual inspection. Segments were then defined as the time period of 0.5 seconds before and after the peak.

D. *Pulse transit time calculation*

To determine the pulse transit time, we wanted to identify the first systolic complex in the BCG, prior to the initial major deflection. The motivation for selecting this point was to determine the onset of rapid ejection. To this end, ensemble averages of 10-30 seconds were decomposed using ensemble empirical mode decomposition (EEMD)[8]. EEMD is a data-adaptive noise-assisted data analysis method that aims to decompose a set of data into physically meaningful “intrinsic mode functions”. Here, we used 100 ensembles, salted with white gaussian noise with an amplitude of 0.5 times the standard deviation of the ensemble mean. Fig. 6 shows a comparison between the ensemble average and IMF 2, and an illustration of the timing points used to estimate the pulse transit time. PTT was defined as the time delay between the peak of the upward deflection prior to the major downward deflection in the ballistocardiogram, immediately preceding the onset of systole in the PPG, and the maximal point of the second derivative of the PPG as the indicator of distal systolic onset. Fig. 6 further shows the variation in pulse transit time (PTT) and systolic blood pressure during rest, intervention, and three minutes post intervention.

III. RESULTS

Fig. 3 shows the pressure distribution under the sole during recording, illustrating the difference in load on the sensor

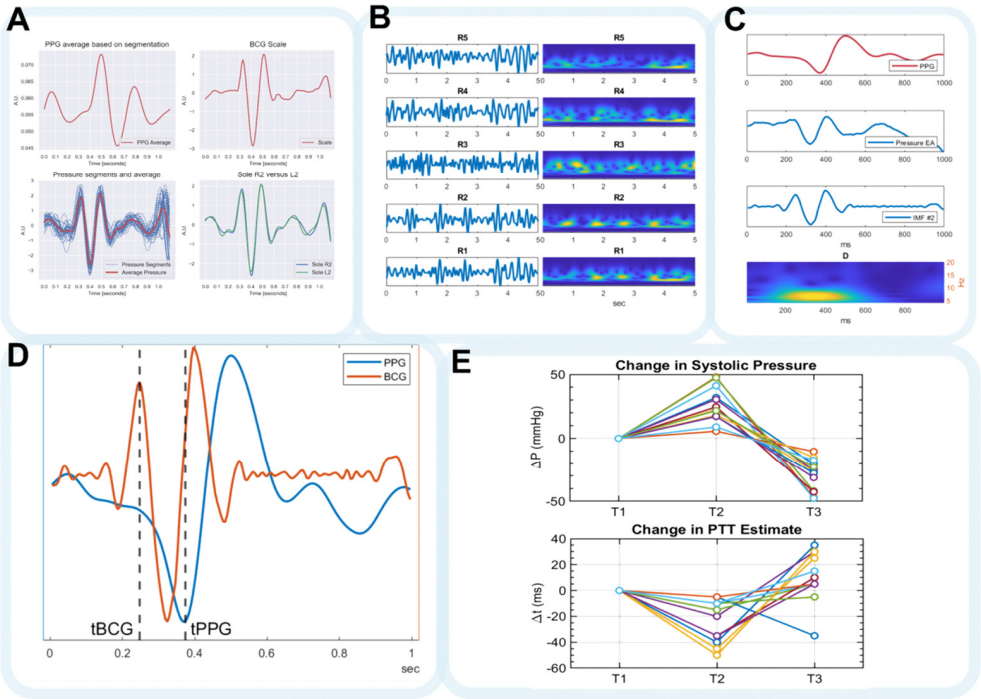

Fig. 4. A: comparison of pressure waveforms from a 23-year-old female. Counterclockwise from top left: ensemble average PPG, 1 s ensembles of pressure waveforms from sensor R2, the same sensor locations on left and right foot, and the reference weigh scale signal. B: recordings from sensor locations 1-5 on one shoe, showing signal quality across the sole. Left: time series, bandpass-filtered between 4 and 12 Hz. Right: wavelet scalogram time-frequency representations (analytic morlet) showing energy distribution over time. C: comparison between (top) unfiltered ensemble average waveform, (center) an EEMD mode, and (bottom) its time-frequency representation. D: PTT estimation from BCG early systolic upward deflection to beginning of PPG systolic upstroke defined as local maximum of the second PPG derivative. E: change in PTT and systolic blood pressure for a subset of participants. T1: rest, T2: cold pressor, T3: 3 minutes post intervention.

units. The results are summarized in Fig. 4. Fig. 4(A) shows representative pressure averages from both soles as well as from a modified home bathroom weigh scale recorded from a 23-year-old female. The shape of the ensemble averaged curves are in good agreement between the weigh scale reference and the sole sensors. Comparing the ensemble average from the left and right foot, no major differences are immediately noticeable. Sensor locations 1 and 2 on the right and left foot gave the most reliable BCG waveforms in all measurement periods with sensor position 3 having varying results. Positions 4 and 5 gave no usable results in terms of measuring BCG. Figure 5 shows the results from the estimation of PTT for 4 participants. In all 4 participants the PTT and blood pressure demonstrate an inverse correlation, although with differing strengths of correlation.

IV. Discussion

The smart soles seem able to record the ballistocardiogram with acceptable resolution. The waveform from the reference weigh scale and the shoes are in good agreement. Sensors in position one and two, corresponding to underneath the heel, seem to consistently perform the best in terms of signal to noise ratio, which makes intuitive sense given the heel is the most direct line between the trunk and the ground reaction force. There were no obvious differences between feet. Although the derived measurements have significant uncertainty, the PTT estimates seem to behave inversely to the systolic blood pressure during the cold pressor test as expected, indicating that the BCG measured in this way might indeed be used for pulse wave velocity estimation.

The present study has some weaknesses. The participants had little variation in age and weight. It is therefore possible that some complications might arise in a broader population. Additionally, time constraints prevented us from allowing participants access to differently sized shoes. No correction for difference in shoe size has been attempted.

The design of the shoes also has some inherent limitations. The bladders, while quite sensitive, are prone to leaking during moderate activity. Beyond more robust construction, the necessary volume and viscosity of the fluid may be investigated, considering the limited degree of necessary deformation. Conceptualizing and troubleshooting sensors for cardiovascular monitoring is inherently complex [6], [9], and will certainly benefit from further iteration.

Only two of the five sensor positions on each foot consistently capture usable ballistocardiograms. If the only goal is ballistocardiography, two sensor placements per foot may suffice. The full array of sensors does however allow for intriguing possibilities in a combined sensor network for gait analysis followed by BCG-based PWV estimation during brief periods of lower activity.

V. Conclusion

We have presented a prototype design for a network of soft sensors integrated into a standard shoe sole for non-invasive cardiographic monitoring. By utilizing fluid-filled bladders in combination with atmospheric pressure sensors the ballistocardiogram can be recorded from each foot at discrete locations. As the sensor array consists of discrete points, foot pressure distribution analysis is also possible. PPG-BCG based pulse transit time estimation showed agreement with previous work during a cold pressor test across multiple participants, strengthening the argument that shoe integration is a viable method of implementing wearable ballistocardiography. Further testing in real world scenarios is needed to evaluate and improve performance outside of controlled laboratory settings, and the sensor units need refining to improve reliability and sensitivity. Investigating the possibilities of measuring the BCG during intermittent physical activity.

VI. References

[1] O. T. Inan *et al.*, "Ballistocardiography and seismocardiography: a review of recent advances," *IEEE J. Biomed. Health Inform.*, vol. 19, no. 4, pp. 1414–1427, Jul. 2015, doi: 10.1109/JBHI.2014.2361732.

[2] P. Yousefian *et al.*, "The Potential of Wearable Limb Ballistocardiogram in Blood Pressure Monitoring via Pulse Transit Time," *Sci. Rep.*, vol. 9, no. 1, p. 10666, Jul. 2019, doi: 10.1038/s41598-019-46936-9.

[3] S. Shin *et al.*, "Posture-Dependent Variability in Wrist Ballistocardiogram-Photoplethysmogram Pulse Transit Time: Implication to Cuff-Less Blood Pressure Tracking," *IEEE Trans. Biomed. Eng.*, vol. 69, no. 1, pp. 347–355, Jan. 2022, doi: 10.1109/TBME.2021.3094200.

[4] S. L.-O. Martin *et al.*, "Weighing Scale-Based Pulse Transit Time is a Superior Marker of Blood Pressure than Conventional Pulse Arrival Time," *Sci. Rep.*, vol. 6, p. 39273, Dec. 2016, doi: 10.1038/srep39273.

[5] M. Etemadi and O. T. Inan, "Wearable ballistocardiogram and seismocardiogram systems for health and performance," *J. Appl. Physiol.*, vol. 124, no. 2, pp. 452–461, Feb. 2018, doi: 10.1152/japplphysiol.00298.2017.

[6] F. S. Solberg, S. Kohtala, H. Vestad, and M. Steinert, "A Combined Photoplethysmography and Force Sensor Prototype for Improved Pulse Waveform Analysis," in *2019 IEEE SENSORS*, Oct. 2019, pp. 1–4. doi: 10.1109/SENSORS43011.2019.8956487.

[7] O. T. Inan, M. Etemadi, R. M. Wiard, L. Giovangrandi, and G. T. A. Kovacs, "Robust ballistocardiogram acquisition for home monitoring," *Physiol. Meas.*, vol. 30, no. 2, pp. 169–185, Jan. 2009, doi: 10.1088/0967-3334/30/2/005.

[8] Y. Song, H. Ni, X. Zhou, W. Zhao, and T. Wang, "Extracting Features for Cardiovascular Disease Classification Based on Ballistocardiography," in *2015 IEEE 12th Intl Conf on Ubiquitous Intelligence and Computing and 2015 IEEE 12th Intl Conf on Autonomic and Trusted Computing and 2015 IEEE 15th Intl Conf on Scalable Computing and Communications and Its Associated Workshops (UIC-ATC-ScalCom)*, Aug. 2015, pp. 1230–1235. doi: 10.1109/UIC-ATC-ScalCom-CBDCom-IoP.2015.223.

[9] T. L. Steffensen, M. Auflem, H. N. Vestad, and M. Steinert, "Embedded Soft Inductive Sensors to Measure Arterial Expansion of Tubular Diameters in Vascular Phantoms," *IEEE Sens. J.*, vol. 22, no. 7, pp. 7240–7247, Apr. 2022, doi: 10.1109/JSEN.2022.3155071.

C2. Embedded Soft Inductive Sensors to Measure Arterial Expansion of Tubular Diameters in Vascular Phantoms

IEEE Sensors Journal, 2022

Torjus Lines Steffensen, Carlo Kriesi, Martin Steinert, Thomas Lafrenz, Jostein Rødseth Brede, and Marius Auflem

Embedded Soft Inductive Sensors to Measure Arterial Expansion of Tubular Diameters in Vascular Phantoms

Torjus L. Steffensen, Marius Auflem, Håvard N. Vestad, *Member, IEEE*, and Martin Steinert

***Abstract*—Measuring diameter change in flexible tubular structures embedded in opaque material is challenging. In this article, we present a soft braided coil embedded in an elastomer tube as a method to continuously measure such a change in diameter. By measuring the inductance change in the braided coil, we estimate the instantaneous diameter with a simple inductance model. In applying this method, we demonstrate that diameter waves in a vascular phantom, a model of a radial artery embedded in a viscoelastic wrist structure, can be recorded continuously. Four sensors were made, and their ability to measure physiologically relevant simulated pulse waves was assessed. Several pressure pulse profiles were generated using a precision digital pump. Inductance of the coil was measured simultaneously as the change in diameter was recorded using an optical laser/mirror deflection measurement. One sensor was then embedded in a vascular phantom model of the human wrist. The diameter of the simulated radial artery was recorded via ultrasound and estimated from coil inductance measurements. The diameter estimates from the inductance model corresponded well with the comparator in both experimental setups. We demonstrate that our method is a viable alternative to ultrasound in recording diameter waves in artery models. This opens opportunities in empirical investigations of physiologically interesting fluid-structure interaction. This method can provide new ability to measure diameter changes in tubular systems where access is obstructed.**

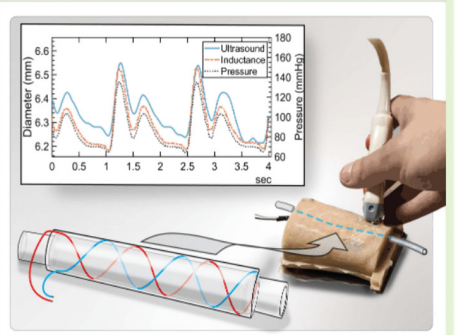

***Index Terms*—In vitro experimentation, inductance, soft electronics, measurement methods.**

I. Introduction

MEASURING pressure propagation in soft tubular structures is of interest in the field of arterial mechanics, where pulse wave propagation can be studied to make conclusions about arterial function [1]–[3]. Many tissues including arteries are viscoelastic [4], making accurate mathematical modeling challenging. Therefore, empirical in vitro experiments are frequently employed [5], [6]. The relationship between fluid forces acting on the wall structure and the resulting change in geometry from the induced strains is one topic of interest. The propagation of the strain energy through the vessel wall can be visualized as waves of expanding and contracting vessel diameter. In vitro models are often considered as freely suspended tubes, for sake of simplicity and observation. However, in cases where the interaction between the model vessel and the surrounding tissue is of interest, this is not feasible. In the case of radial tonometry, a technology that is seeing interest for applications in wearable blood pressure monitoring [7]–[9], the interaction between the vessel wall, the underlying bone, and the tissue between the vessel and skin surface are all important. This can be achieved by placing the vessel model inside tissue-mimicking material, obstructing view of the tube [10].

There are few methods to continuously measure a varying diameter in a soft tube inside an opaque material. Here, we propose a soft braided coil cast inside an elastomer tube wall as such a method. To allow for radial expansion from pressurizing the tube, the sensor consists of a high pitch helical coil. The coil is routed back and forth over the length of the tube section, resulting in a weaved braid pattern, as opposed to a sequentially stacked coil (Fig. 1).

A change in the tube's diameter also changes the diameter of the coil, which in turn alters its inductance. This principle has previously been applied in sensing actuation lengths in

Manuscript received January 22, 2022; revised February 23, 2022; accepted February 23, 2022. Date of publication February 25, 2022; date of current version March 31, 2022. The work of Marius Auflem was supported by the Research Council of Norway under Grant 290404. The associate editor coordinating the review of this article and approving it for publication was Dr. Edward Sazonov. *(Corresponding author: Torjus L. Steffensen.)*

Torjus L. Steffensen is with the Department of Circulation and Medical Imaging, Norwegian University of Science and Technology, 7025 Trondheim, Norway (e-mail: torjus.l.steffensen@ ntnu.no).

Marius Auflem, Håvard N. Vestad, and Martin Steinert are with the Department of Mechanical and Industrial Engineering, Norwegian University of Science and Technology, 7025 Trondheim, Norway.

Digital Object Identifier 10.1109/JSEN.2022.3155071

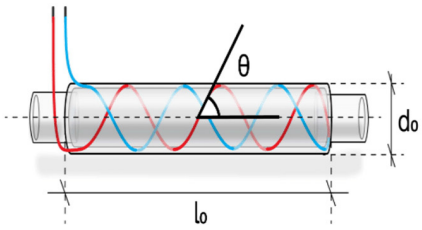

Fig. 1. Geometry of the sensor tube, showing the braided coil structure and connecting pressure tubes.

pneumatic actuators (McKibben muscles) [11], [12]. Similar flexible coils have also been used to determine angular change from the induced current resulting from the change in magnetic field caused by bending the coil [13]. Here, we focus on small, sub-millimeter changes in diameter caused by differences in internal pressure.

A. Detection Principle

With a fixed wire length, a braid pattern causes axial contraction of the helical structure from altered braid angles as the diameter increases. As the wire is routed in the same rotational direction around the tube the electromagnetic properties of the solenoid and current direction are preserved. We can then estimate the relationship between the cross-sectional area of the coil and the inductance L as in a long solenoid [11]:

$$L = \frac{\mu N^2 A}{l} \tag{1}$$

where N is the number of effective coil windings, μ is the magnetic permeability of the core (for air, we set μ approximately equal to vacuum permeability μ_0), and A is the cross-sectional area of the "solenoid". For a winding angle of 20° the model is roughly linear to the full extent of expansion and compression as limited by the braid [11]. In this work we operate well within this range.

The accuracy of the long solenoid model in braided soft actuators has been compared to more sophisticated inductance models [11], and while accuracy decreases with deformation size, for small deformations the error is small.

For a braided tube of length l, relaxed diameter D_0 and wire winding angle θ with respect to the long axis of the braid, assuming constant coil length and a circular cross section the length of the coil helix b is given by

$$b = \frac{l_e}{\cos(\theta)} \tag{2}$$

where l_e is the length of the fully relaxed tube. The number of turns each helix of the braid makes around the axis of the cylinder n is given by:

$$n = \frac{b \sin(\theta_0)}{\pi D_0} \tag{3}$$

TABLE I
TUBE DIMENSIONS

Tube no.	D_0	l_e	θ_0
1	6.2 mm	90 mm	25°
2	6.8 mm	58 mm	23°
3	5.3 mm	100 mm	18°
4	7.2 mm	75 mm	25°

Equation (3) along with the number of helices in the sensor gives us a value for the effective number of coil windings N [11], [14]. To determine a change in tube radius r from an associated change in inductance, we expand (1):

$$\Delta L = (L - L_0) = \frac{\mu N^2 \pi (r^2 - r_0^2)}{l} \tag{4}$$

Which is equivalent to:

$$r = \sqrt{\frac{(L - L_0) l}{\mu N^2 \pi} + r_0^2} \tag{5}$$

In a material with a positive Poisson's ratio the change in diameter necessarily also results in a contraction along the length of the tube. In the case of small deformations in a long thin tube, where $l \gg D$, we assume that the change in cylinder length is negligible in relation to the change in diameter and treat l as constant. The resulting relationship is nonlinear, but locally behaves approximately linearly for small deformations [12].

B. Sensor Fabrication

We made sensors by winding flexible silicone shielded wire onto a dowel. The resulting braids were then molded in Ecoflex 00-10 (Smooth-On, USA) by pouring and continuous rotation. Ecoflex 00-10 is a very soft elastomer, with a reported static Young's modulus of 0.05 MPa at 10% strain [15]. Removing the dowel, the resulting structure is a braided flexible wire embedded in a silicone tube of roughly uniform thickness.

We made four sensors to compare their behavior and to account for differences in coil characteristics due to the artisanal nature of the manufacturing process (Table I).

II. EXPERIMENTS & METHODS

A. Pressure Expansion

We conducted an experiment to assess the change in sensor induction due to expansion under pressure (Fig. 2). The sensor tube was fixed horizontally to an inclined plane, and the ends of the tube were fixed to prevent angular deformation during expansion and contraction.

The ends of the wire braids in the tube sensor were connected to a parallel capacitor, forming an LC oscillator circuit. This circuit was connected to an induction-to-digital converter (LDC1612, Texas Instruments, Texas, USA). The LDC1612 operates by applying a drive current to an LC circuit

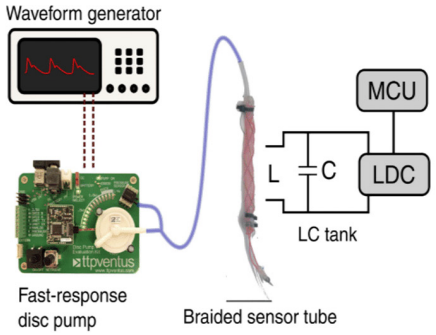

Fig. 2. Schematic illustration of the experimental setup.

and measuring the resulting primary oscillation frequency f_0. In our configuration the LDC was connected to an external 40 MHz reference oscillator, which is used to determine f_0. Given that the parallel capacitance C is known, this allows for the determination of the inductance L through the relationship

$$f_0 = \frac{1}{2\pi\sqrt{LC}} \tag{6}$$

Each of the four tubes was in turn connected to a precision digital control disc pump (XP-S2-028, TTP Ventus, UK). The other end of the tube was clamped shut, resulting in a controllable internal pressure when the pump was active. A differential pressure sensor (TSC 015PD, Honeywell International, USA) gauged the air pressure inside the tube against ambient atmosphere.

As the diameter of the tube changes in response to the pressure variation, as does the diameter of the coil, resulting in an increase in L. Thus f_0 varies over the course of the load cycle, allowing a calculation of L from (6).

The disc pump was controlled with an arbitrary waveform generator (UTG2025A, UNI-T, China). Inductance and pressure were recorded at three different load states (Table II). First, after setting up the experiment, one minute of inductance readings was recorded to establish L_0 for each tube in the unloaded state. Second, a 0.5 Hz square wave pressure cycle was applied to the tube for a period of 4 minutes. Pressure was then allowed to equalize to ambient pressure. Lastly an arterial pulse pressure waveform was applied for 1 minute. The wave profile was recorded from the proper palmar digital artery at the middle phalanx of the left middle finger using a volume-clamp apparatus (NIBP Nano INL382, ADInstruments, Dunedin, New Zealand).

Data was collected on a Windows PC and processed in MATLAB r2021a (The Mathworks, Massachusetts, USA).

B. Response Validation

To record the change in tube diameter, the tube was fixed to an angled plate and restricted in a single point with cyanoacrylate glue, allowing it to expand and retract with the center of the tube moving normally to the angled plate.

TABLE II
EXPERIMENTAL PROTOCOL

Load type	Cycle Frequency	Pressure range	Duration
Zero load	n/a	Ambient	1 minute
Square wave	0.5 Hz	30 - 90 mmHg	4 minutes
Arterial wave	1 Hz	40 – 100 mmHg	1 minute

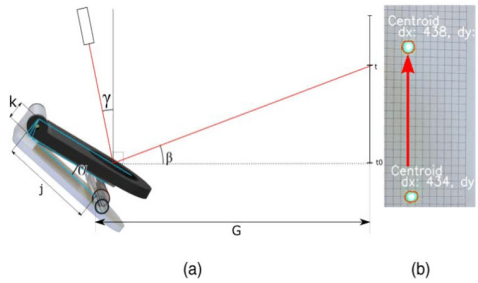

Fig. 3. (a) Schematic of laser measurement geometry used to measure expansion and contraction of the tubes. (b) Illustration of the laser dot tracking. Not to scale.

A mirror, rotating freely on a hinge, was placed resting on top of the tube. The expansion of the tube then resulted in a small angular change of the mirror, proportional to the increase in diameter of the tube (Fig. 3). A laser was focused on the mirror at an angle, and the resulting laser dot was recorded moving against a reference scale placed at a distance to amplify the movement [16].

The diameter of the tube could then be determined from the motion of the laser dot through a trigonometric relationship:

$$r \cong \tan\left(\frac{\tan^{-1}\left(\frac{t_1}{G}\right)+\gamma+2\alpha_0}{4}\right) \times\left(j+k\tan\left(\frac{\tan^{-1}\left(\frac{t_1}{G}\right)+\gamma+2\alpha_0}{4}\right)\right) \tag{7}$$

where r is the radius, t is the height of the laser dot on the target relative to the height of the mirror, k is the vertical distance from the hinge point to the baseplate where the tube is fixed (8.5mm), j is the lateral distance from hinge point to fixation point of tube (40mm), G is the horizontal distance between mirror and target (9980mm), and α_0 is the angle of the mirror hinge where the resulting angle between mirror and the horizontal plane is 45 degrees (7.5 degrees). γ is the angular deviation of the laser from the vertical axis. This is tuned with an adjustment screw on the laser to hit the target regardless of the different diameters of the tubes. γ is calculated using (7) and a caliper measurement of the diameter of the tube.

We recorded the movement of the laser dot with a digital camera at a resolution of 3840×2160 pixels. Frame to frame position was determined using open-source video analysis

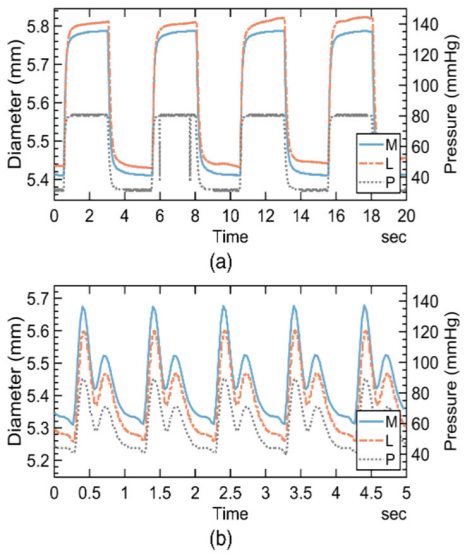

Fig. 4. Change in tube diameter from applied internal pressure, measured via mirror deflection, and estimated from inductance. M: diameter measured via mirror deflection, L: diameter estimate from inductance measurement, P: internal tube pressure. (a) 0.5 Hz square wave. (b) 1 Hz radial pulse wave.

tools (OpenCV) and referenced against the background scale. The result is a time series of the tube diameter with a time step resolution of 30 samples per second and a geometric resolution of 3.56 pixels per mm of laser movement (Fig. 4).

Equation (7) is simplified and does not account for vertical movement of the mirror. These effects result in a vertical displacement of the laser dot less than the total diameter change of the tube, which is negligible in comparison to the displacement of the dot due to angular change.

C. Drift Measurement

We observed significant sensor drift during long recordings. To assess the scale of drift in ambient conditions and the influence of temperature we placed a tube sensor on a vibration isolated table exposed to ambient atmosphere over 24 hours and applied a 0.5 Hz square-wave pressure load cycle. Inductance was measured from the coil alongside ambient temperature with a BMP388 atmospheric pressure and temperature sensor (Bosch Sensortec, Germany) in the immediate vicinity of the tube (Fig. 5). Drift was confirmed and appeared to behave approximately linearly in the first regime (zero to sixteen hours), before a temperature impulse caused a dramatic upwards spike. We believe this impulse to have been caused by the sun shining on our lab, a hypothesis supported by in situ meteorological observations.

For the first 7 hours, the temperature sensor reported rising temperatures with a seemingly logistic growth. A likely

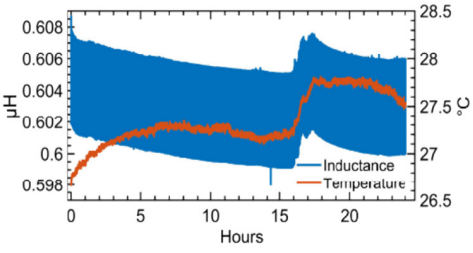

Fig. 5. Inductance recorded over a 24-hour 0.5 Hz load cycle in ambient conditions. Drift appears to behave linearly in the first 15 hours.

explanation is internal temperature increase in the temperature sensor itself once powered. In time the temperature sensor reaches equilibrium and disperses the same amount of heat as it produces to the surroundings, after which the temperature data seems to correspond well with the drift of the inductance sensor. Afterwards, the response of the inductance measurement to the temperature spike suggests the drift is dominated by thermal effects. This sensitivity to small changes in temperature must be considered in applications.

We performed a linear regression on the component of the drift occurring before the temperature impulse took place, resulting in a slope of -1.48×10^{-10} H/hour.

D. Application in a Radial Artery Phantom

To assess the usability of these sensors in a vascular phantom we embedded one of the previously tested braided tube sensors in a wrist model. The wrist was cast in silicone elastomer (Ecoflex, Smooth-On, USA) in a mold produced via fused filament fabrication (FFF). The mold was modeled from a high-resolution scan of the human wrist. We also placed an FFF-printed radius and ulna bone from the same anatomical model into the cast to provide internal structure. The embedded tube had an inner diameter of 3 mm, matching a realistic range for the human radial artery[17] (Fig. 6).

We pressurized the tube system as before, but this time flushed it with water instead of air to allow ultrasound imaging. The pump compressed a small amount of air in the upstream tubing, acting as a piston on the internal water reservoir. The water was mainly static, although the pressure difference in the air piston resulted in minor oscillatory back-and-forth flow. We did not expect exchanging water for air to have a significant effect on the inductance in the coil, as the magnetic permeability of water is similar to that of air [18].

We investigated the flushed and pressurized phantom under ultrasound (Vivid E95, GE Healthcare) to compare the change in diameter of the embedded tube to that estimated from the inductance. We applied the same arterial pulse pressure profile. Due to the surrounding tissue now resisting compression, we had to apply a higher pressure to see the same range of diameter motion. The load varied between 70 – 135 mmHg, as measured in the air piston. This corresponds well to a realistic blood pressure range [4].

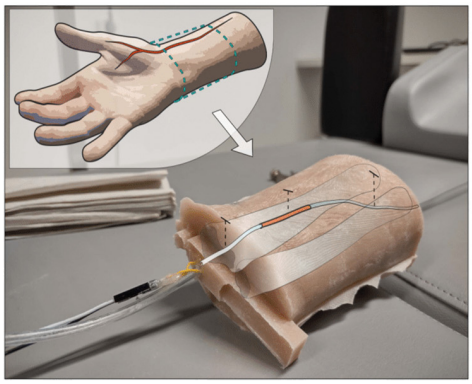

Fig. 6. Illustration of the wrist phantom with the placement of the radius, ulna, and sensor tube superimposed. The phantom simulates a section of the right wrist, with bone, blood vessel, and mediating tissue.

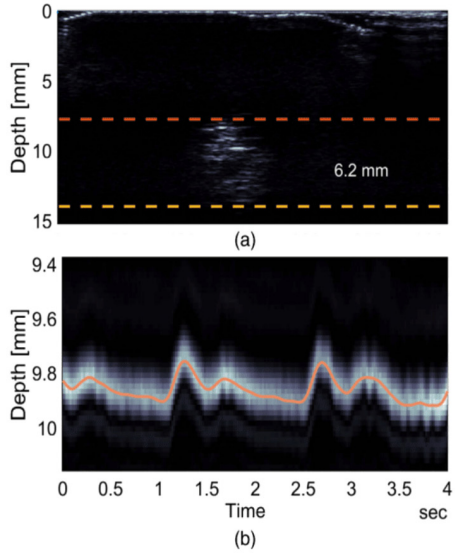

Fig. 7. (a) B-mode ultrasound of the wrist phantom, approximately 5 cm distal to the styloid process. Note that no effort was made to induce echogenicity in the phantom, resulting in a poorly defined image. (b) M-mode recording illustrating the pulsatile movement of the "lumen". A centerline trace of the tube wall has been superimposed.

It is important to note that the material in the phantom has significantly different acoustic properties from those of human tissue. This difference must be accounted for when using equipment calibrated for real tissue. Most importantly for this application, the speed of sound differs, which will affect the calculated depth scale of the ultrasound machine. A rough compensation can be done by correcting for the difference in local speed of sound, also referred to as the propagation velocity:

$$z_{corr} = z\frac{C_{EF}}{C_T} \tag{8}$$

where z_{corr} is the corrected depth z, and C_t and C_{EF} are the propagation velocities in soft tissue and Ecoflex polymer respectively. As C varies between tissues, C_t is commonly taken to be the average value of several common types of soft tissue, approximately 1.54 m/s [19]. Together with the propagation velocity in the silicone material, 0.97 m/s [20], a correction factor of 0.63 is obtained. The propagation velocity in the phantom tissue is slower than the expected value for human tissue. The uncorrected depth therefore assumes a greater distance has been traveled by the reflected sound wave. If not corrected the estimated depth values will be erroneously large.

We measured the relaxed diameter a priori and confirmed this measurement under ultrasound B-mode to confirm good correspondence. In the M-mode configuration, a sequence of single ultrasound scan lines is collected and presented to illustrate the spatial movement of structures in the scan line over time. By recording the motion of the wall of the artery, a "diameter wave" can be obtained (Fig. 7). By combining the motion of a point in the tube wall with the initial, or smallest, diameter, the diameter of the vessel over time can be reconstructed. (Fig. 8) shows the diameter of the embedded soft tube determined in this way, alongside the diameter of the tube estimated using the same nominal starting diameter and the inductance measurement.

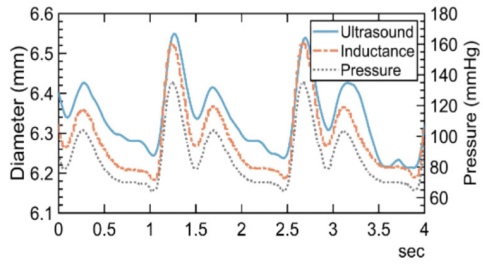

Fig. 8. Diameter calculated from phantom lumen wall movement from ultrasound plotted with the estimate from inductance. The profile of the pressure trace is consistent over the three cycles shown. At around 3 seconds a peak is shifted in the ultrasound trace. This is not reflected in the pressure or inductance curves, implying that it is an artifact introduced in the ultrasound recording.

III. Results and Discussion

Over the course of contraction and expansion, the sensor tube system experiences some hysteresis, as can be expected from the viscoelastic properties of the structural material (Fig. 9). Within the isolated loading and unloading regimes, a linear fit can still be made to estimate sensor sensitivity. Linear regression models were fitted on monotonically increasing tube expansion series using a robust fit method implemented in MATLAB's fitlm function. The results presented strong linear fits to the data (R^2 between 0.994 and 0.997). Apparent sensitivities corresponding to the regression

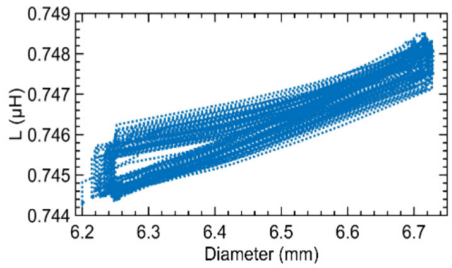

Fig. 9. Superposition of inductance and diameter traces measured over 4 minutes of cyclic loading, showing hysteresis as well as drift.

TABLE III
REGRESSION ESTIMATES OF BEST LINEAR FIT

Tube no.	Closest linear fit	Corresponding apparent sensitivity, 10^{-7} H/mm
1	$r = 6.58 \times 10^{-7} L - 46.08$	7.12
2	$r = 3.97 \times 10^{-7} L - 18.60$	4.89
3	$r = 4.96 \times 10^{-7} L - 20.15$	4.27
4	$r = 7.02 \times 10^{-7} L - 42.77$	6.20

model are presented in Table III. The sensitivity range agrees broadly with previous work [11]. The mean absolute error of the inductance estimate compared to the laser measurement ranged from 0.02 to 0.06 mm. This result is associated with some uncertainty, which is discussed later.

Sensor resolution in our setup is determined by the output of the LDC1612 converter, which has a total resolution of 28 bits. In practice, effective resolution is limited by the electromagnetic properties of the sensor element in the LC circuit and by the sample rate. As the LDC can essentially be viewed as a frequency-to-digital converter, the LSB is measured in Hz, and is determined primarily by the reference count of the converter and the variation of the signal frequency. We observed a typical frequency variation in our target signal of around 0.5%, which with a reference clock timed at 40 MHz and a sample rate of 300 Hz corresponds to 11 bits of effective resolution over the range of interest [21]. For the same configuration, reducing the sample rate to 100 Hz results in an increase in effective resolution to 12 bits as the reference count increases.

A. Error Sources

There are benefits and drawbacks to using LDCs compared to a benchtop LCR meter. Perhaps the clearest benefits are sampling rate, which can reach several thousand Hz under some circumstances, high portability, and low cost of implementation. But because the measured value of the LDC is the oscillation frequency of an LC circuit, it is necessary for the designer to have precise control of their coil characteristics. As tables I and III show, the sensitivity of the coil varies significantly with coil dimensions. As loosely wound, high-pitch coils such as the ones we have used here typically have small self-inductance values, the oscillation frequency is typically high without a very small parallel capacitance, as can be seen from (6). In our experiments, the sensor frequencies were between 6-8 MHz in this configuration. Lowering the parallel capacitance or adding inductors in series can bring the frequency range down, but this increases noise outside of the manufacturer's recommended capacitance range as the effects of parasitic capacitance in the coil become more noticeable [22] and reduces effective signal resolution. Skin effects also become significant at these frequency ranges, which may contribute some error to the estimates we derive from the inductance values. Skin effect is not accounted for in our model.

The parallel capacitor in our LC circuit was placed at the end of the connecting wires from the coil, rather than immediately outside the coil, which is the recommended configuration [21]. This may have contributed to a greater parasitic capacitance, resulting in an unstable source of error in the calculation of inductance from the oscillation frequency. In future applications the influence of the coil placement in relation to the measurement electronics should be considered.

Other sources of error relate to the uncertainty in our coil parameters. Much of this uncertainty is due to the hand-made nature of the coils. The winding angle, for example, may differ slightly over the length of the coil, as may the thickness of the polymer layer under the conductive material. The ends of the coil are also nonuniform because of the fabrication process. Improving this process so that coil geometry is more uniform would reduce this uncertainty in future applications.

Determining the diameter expansion of the tube using the laser and mirror setup is dependent on a geometric relationship which is subject to several simplifying assumptions and precision measurements. There is some uncertainty associated with the absolute values determined in this way. The pixel resolution of the laser measurement puts a lower bound on the absolute certainty of the measurement. The resolution of the video, at 0.278 mm per pixel, with an average of 255 pixels of laser travel corresponding to approximately 0.5 mm of expansion range results in a theoretical measurement resolution around 2 μm using the laser mirror setup. Errors due to simplifying assumptions in calculating the geometric relationship and imprecisions in the experimental setup are certainly larger than this resolution limit.

Significant drift was observed over the course of several-minute long recordings. The drift appeared to behave in a broadly linear manner, suggesting it could be compensated for. The sensitivity of the system to small changes in temperature poses some challenges to practical use. Temperature-sensitive elements in our experimental setup include the coil itself, the parallel capacitor, and the reference clock. The coil was not separated thermally from the measurement circuitry in our experiment, but as this more closely reflects the likely realities of a real-world application, the observed behavior may be more informative for the application designer. Perhaps most importantly, handling of the sensor might adversely affect the measurement. Regular calibration of the estimate value should be done against a known reference value.

B. Application Validation

Ultrasound recording over time is challenging. Even when recording structures that are relatively motionless, the probe must be kept perfectly still. Robot-assisted systems do exist, but are rare, and in most real cases ultrasound recordings will be done by hand [23]. The quality of the recording is therefore dependent on the skill of the operator. The practical consequence of this is that without skilled operators, many otherwise high-quality recordings may not be stable over time. In our data, the shape of the inductance measurement corresponds more closely to that of the internal pressure than the trace from the ultrasound, especially in the third cycle of the M-mode trace (Fig. 8). A likely explanation for this is instability of the ultrasound probe in relation to the "artery" over the time of the recording. In some situations, measurement of structural diameter from coil inductance could be a more reliable measure of internal geometry than operator-guided ultrasound in continuous recordings.

IV. Conclusion

We have presented the manufacture and application of soft sensor tubes consisting of braided wire coils wound inside a soft silicone rubber sleeve. As part of an LC tank together with an inductance-to-digital converter, these sensors can detect small changes in their diameter caused by differences in internal pressure with high fidelity. The sensor was sampled at 300 Hz and corresponded well with comparator measurements of the tube diameter collected optically and with ultrasound. The sample rate of the inductance measurement was higher than those easily achievable with the comparator methods, implying that the sensor might be useful in applications with high requirements for temporal resolution, such as pressure wave analysis.

While the sensor exhibits drift and hysteresis that could be prohibitive to very high precision measurements, presumably because of thermal and viscoelastic effects, the resolution was satisfactory for deformations in the tenths of a millimeter range. Linear drift seemed to be in correspondence to temperature changes in the ambient atmosphere, indicating that temperature compensation could be necessary in a practical application.

Soft braided coils embedded in flexible polymer can be used to estimate small deformations of embedded tubular structures using self-inductance, presenting an alternative to ultrasound in vascular phantoms. Possible applications include transient flow-through pressure impulse monitoring, pipe inspection, or mold channel cleaning.

In future work we want to recreate the results presented here using compliant conductors to avoid the composite effects of the coil structure on the mechanical properties of the tube. We intend to apply this well-performing measurement method to investigate numerical models of pressure coupling in the wrist for noninvasive wearable blood pressure sensors.

References

[1] D. Agnoletti *et al.*, "Pulse pressure amplification, pressure waveform calibration and clinical applications," *Atherosclerosis*, vol. 224, no. 1, pp. 108–112, Sep. 2012, doi: 10.1016/j.atherosclerosis.2012.06.055.

[2] M.-M. Laurila *et al.*, "Evaluation of printed P(VDF-TrFE) pressure sensor signal quality in arterial pulse wave measurement," *IEEE Sensors J.*, vol. 19, no. 23, pp. 11072–11080, Dec. 2019, doi: 10.1109/JSEN.2019.2934943.

[3] W. W. Nichols, M. F. O'Rourke, and C. Vlachopoulos, "Pressure pulse waveform analysis," in *McDonald's Blood Flow in Arteries. Theoretical, Experimental and Clinical Principles*, 6th ed. London, U.K.: Hodder Arnold, 2011.

[4] W. W. Nichols, M. F. O'Rourke, and C. Vlachopoulos, *McDonald's Blood Flow in Arteries. Theoretical, Experimental and Clinical Principles*, 6th ed. London, U.K.: Hodder Arnold, 2011.

[5] Y. Ma, J. Choi, A. Hourlier-Fargette, Y. Xue, H. U. Chung, and J. Y. Lee, "Relation between blood pressure and pulse wave velocity for human arteries," *Proc. Nat. Acad. Sci. USA*, vol. 115, no. 44, pp. 11144–11149, 2018, doi: 10.1073/pnas.1814392115.

[6] S. G. Yazdi, P. H. Geoghegan, P. D. Docherty, M. Jermy, and A. Khanafer, "A review of arterial phantom fabrication methods for flow measurement using PIV techniques," *Ann. Biomed. Eng.*, vol. 46, no. 11, pp. 1697–1721, Nov. 2018, doi: 10.1007/s10439-018-2085-8.

[7] F. S. Solberg, S. Kohtala, H. Vestad, and M. Steinert, "A combined photoplethysmography and force sensor prototype for improved pulse waveform analysis," in *Proc. IEEE SENSORS*, Oct. 2019, pp. 1–4, doi: 10.1109/SENSORS43011.2019.8956487.

[8] M. Kaisti *et al.*, "Clinical assessment of a non-invasive wearable MEMS pressure sensor array for monitoring of arterial pulse waveform, heart rate and detection of atrial fibrillation," *NPJ Digit. Med.*, vol. 2, no. 1, May 2019, doi: 10.1038/s41746-019-0117-x.

[9] S. Chen, J. Qi, S. Fan, Z. Qiao, J. C. Yeo, and C. T. Lim, "Flexible wearable sensors for cardiovascular health monitoring," *Adv. Healthcare Mater.*, vol. 10, no. 17, Sep. 2021, Art. no. 2100116, doi: 10.1002/adhm.202100116.

[10] G. Jo, T.-H. Yang, J.-H. Koo, M.-H. Jun, and Y.-M. Kim, "A transfer function model development for reconstructing radial pulse pressure waveforms using non-invasively measured pulses by a robotic tonometry system," *Sensors*, vol. 21, no. 20, p. 6837, Oct. 2021, doi: 10.3390/s21206837.

[11] W. Felt, K. Y. Chin, and C. D. Remy, "Contraction sensing with smart braid McKibben muscles," *IEEE/ASME Trans. Mechatronics*, vol. 21, no. 3, pp. 1201–1209, Jun. 2016, doi: 10.1109/TMECH.2015.2493782.

[12] W. Felt and C. D. Remy, "Smart braid: Air muscles that measure force and displacement," in *Proc. IEEE/RSJ Int. Conf. Intell. Robots Syst.*, Sep. 2014, pp. 2821–2826, doi: 10.1109/IROS.2014.6942949.

[13] A. V. Prituja, H. Banerjee, and H. Ren, "Electromagnetically enhanced soft and flexible bend sensor: A quantitative analysis with different cores," *IEEE Sensors J.*, vol. 18, no. 9, pp. 3580–3589, May 2018, doi: 10.1109/JSEN.2018.2817211.

[14] W. Felt and C. David Remy, "A closed-form kinematic model for fiber-reinforced elastomeric enclosures," *J. Mech. Robot.*, vol. 10, no. 1, Nov. 2017, doi: 10.1115/1.4038220.

[15] J. Vaicekauskaite, P. Mazurek, S. Vudayagiri, and A. L. Skov, "Mapping the mechanical and electrical properties of commercial silicone elastomer formulations for stretchable transducers," *J. Mater. Chem. C*, vol. 8, no. 4, pp. 1273–1279, Jan. 2020, doi: 10.1039/C9TC05072H.

[16] T. Ha, J. Ma, J. Blindheim, T. Welo, G. Ringen, and J. Wang, "In-line springback measurement for tube bending using a laser system," *Proc. Manuf.*, vol. 47, pp. 766–773, 2020, doi: 10.1016/j.promfg.2020.04.233.

[17] H. V. Riekkinen, K. O. Karkola, and A. Kankainen, "The radial artery is larger than the ulnar," *Ann. Thoracic Surgery*, vol. 75, no. 3, pp. 882–884, Mar. 2003, doi: 10.1016/S0003-4975(02)04557-5.

[18] B. D. Cullity and C. D. Graham, *Introduction to Magnetic Materials*, 2nd ed. New York, NY, USA: Wiley, 2009.

[19] M. K. Feldman, S. Katyal, and M. S. Blackwood, "U.S. artifacts," *Radio Graph.*, vol. 29, no. 4, pp. 1179–1189, Jul. 2009, doi: 10.1148/rg.294085199.

[20] A. Cafarelli, P. Miloro, A. Verbeni, M. Carbone, and A. Menciassi, "Speed of sound in rubber-based materials for ultrasonic phantoms," *J. Ultrasound*, vol. 19, no. 4, pp. 251–256, Apr. 2016, doi: 10.1007/s40477-016-0204-7.

[21] C. Oberhauser, *Optimizing L Measurement Resolution for the LDC161x and LDC1101*. Dallas, TX, USA: Texas Instruments, Feb. 2016.

[22] *Sensor Design for Inductive Sensing Applications Using LDC. Rev C*. Texas Instruments, Dallas, TX, USA, May 2021.

[23] R. Monfaredi, "Robot-assisted ultrasound imaging: Overview and development of a parallel telerobotic system," *Minimally Invasive Therapy Allied Technol.*, vol. 24, no. 1, pp. 54–62, 2015, doi: 10.3109/13645706.2014.992908.

Torjus L. Steffensen was born in Bergen, Norway, in 1993. He received the M.Sc. degree in mechanical engineering from the Norwegian University of Science and Technology (NTNU) in 2019, where he is currently pursuing the Ph.D. degree in medical technology with the TrollLABS.

His research interests include soft sensors, wearable longitudinal health monitoring, and data processing methods for physiology time series data.

Håvard N. Vestad (Member, IEEE) was born in Bergen, Norway, in 1993. He received the M.Sc. degree in mechanical engineering from the Norwegian University of Science and Technology in 2018, where he is currently pursuing the Ph.D. degree with the Prototyping Laboratory TrollLABS.

His research interests include soft robotics and sensors, prototyping methodology, and early prototyping concept development for complex sensor problems.

Martin Steinert was born in Dresden, Germany. He received the B.A., M.A., and Ph.D. (Dr.Rer.Pol) degrees from the University of Fribourg, Switzerland, majoring in technology management.

He has been an Assistant Professor at the University of Fribourg, Switzerland, and a Visiting Scholar at the MIT and Stanford University before changing full-time to Stanford University as the Deputy Director of the Center for Design Research (CDR), and an Assistant Professor (Acting) of Mechanical Engineering with Stanford University. Since 2013, he has been a Full Professor of Engineering Design at the Department of Mechanical and Industrial Engineering (MTP), Norwegian University of Science and Technology (NTNU). He is a Professor of the NTNU. As of August 2021, he has more than 200 publications. His research interests focus on the fuzzy front end of new product development and design: optimizing the intersection of engineering design thinking and new product development, mechatronics/sensors, and computer sciences (especially machine learning). A special focus is on conceptual development and alpha prototype generation of high-performance requirements, as well as on experimental tools and setups.

Dr. Steinert has been a member of the Norwegian Academy of Technological Sciences (NTVA) since 2015. He has several prizes in both teaching and research.

Marius Auflem was born in Stavanger, Norway, in 1992. He received the M.Sc. degree in mechanical engineering from the Norwegian University of Science of Technology (NTNU) in 2018.

He currently works as an Industrial Ph.D. candidate at the TrollLABS, NTNU, together with Laerdal Medical. His research interests include medical simulation technology, soft robotics, and prototyping in the early stages of product development.

C3. Wrist ballistocardiography and invasively recorded blood pressure in healthy volunteers during reclining bike exercise

Frontiers in Physiology, 2023

Torjus Lines Steffensen, Filip Emil Schjerven, Hans Martin Flade, Idar Kirkeby-Garstad, Emma Ingeström, Fredrik Samdal Solberg, and Martin Steinert

frontiers | Frontiers in Physiology

TYPE Original Research
PUBLISHED 12 May 2023
DOI 10.3389/fphys.2023.1189732

OPEN ACCESS

EDITED BY
Lee Stoner,
University of North Carolina at Chapel Hill, United States

REVIEWED BY
Alex Pomeroy,
University of North Carolina at Chapel Hill, United States
Martin Bahls,
Universitätsmedizin Greifswald, Germany

*CORRESPONDENCE
Torjus L. Steffensen,
torjus.l.steffensen@ntnu.no

RECEIVED 19 March 2023
ACCEPTED 04 May 2023
PUBLISHED 12 May 2023

CITATION
Steffensen TL, Schjerven FE, Flade HM, Kirkeby-Garstad I, Ingeström E, Solberg FS and Steinert M (2023), Wrist ballistocardiography and invasively recorded blood pressure in healthy volunteers during reclining bike exercise. *Front. Physiol.* 14:1189732. doi: 10.3389/fphys.2023.1189732

Wrist ballistocardiography and invasively recorded blood pressure in healthy volunteers during reclining bike exercise

Torjus L. Steffensen[1]*, Filip E. Schjerven[2], Hans M. Flade[1,3], Idar Kirkeby-Garstad[1,3], Emma Ingeström[1], Fredrik S. Solberg[4] and Martin Steinert[5]

[1]Department of Circulation and Medical Imaging, Norwegian University of Science and Technology, Trondheim, Norway, [2]Department of Computer Science, Norwegian University of Science and Technology, Trondheim, Norway, [3]St. Olav's University Hospital, Trondheim, Norway, [4]Department of Mechanical Engineering, Stanford University, Palo Alto, CA, United States, [5]Department of Mechanical Engineering, Norwegian University of Science and Technology, Trondheim, Norway

Objective: Ballistocardiogram (BCG) features are of interest in wearable cardiovascular monitoring of cardiac performance. We assess feasibility of wrist acceleration BCG during exercise for estimating pulse transit time (PTT), enabling broader cardiovascular response studies during acute exercise and improved monitoring in individuals at risk for cardiovascular disease (CVD). We also examine the relationship between PTT, blood pressure (BP), and stroke volume (SV) during exercise and posture interventions.

Methods: 25 participants underwent a bike exercise protocol with four incremental workloads (0 W, 50 W, 100 W, and 150 W) in supine and semirecumbent postures. BCG, invasive radial artery BP, tonometry, photoplethysmography (PPG) and echocardiography were recorded. Ensemble averages of BCG signals determined aortic valve opening (AVO) timings, combined with peripheral pulse wave arrival times to calculate PTT. We tested for significance using Wilcoxon signed-rank test.

Results: BCG was successfully recorded at the wrist during exercise. PTT exhibited a moderate negative correlation with systolic BP ($\rho_{Sup} = -0.65$, $\rho_{SR} = -0.57$, $\rho_{All} = -0.54$). PTT differences between supine and semirecumbent conditions were significant at 0 W and 50 W ($p < 0.001$), less at 100 W ($p = 0.0135$) and 150 W ($p = 0.031$). SBP and DBP were lower in semirecumbent posture ($p < 0.01$), while HR was slightly higher. Echocardiography confirmed association of BCG features with AVO and indicated a positive relationship between BCG amplitude and SV ($\rho = 0.74$).

Significance: Wrist BCG may allow convenient PTT and possibly SV tracking during exercise, enabling studies of cardiovascular response to acute exercise and convenient monitoring of cardiovascular performance.

KEYWORDS

cardiovascular monitoring, exercise physiology, cardiovascular physiology, ballistocardiography, postural effects, wearable sensors, blood pressure, noninvasive monitoring

1 Introduction

Cardiovascular responses to physical exercise, particularly acute blood pressure (BP) response, are risk markers for development of hypertension and overall cardiovascular events (Miyai et al., 2002; Thanassoulis et al., 2012). Changes in pulse transit time (PTT), a correlate of arterial stiffness, between exercise and recovery have been linked to cardiovascular disease (CVD) risk factors (Liu et al., 2014), suggesting a convenient tracking exercise PTT trends could facilitate early detection or out-of-clinic monitoring of CVD patients. PTT has also garnered research interest for its potential application in cuffless BP trend tracking (Geddes et al., 1981; Kim et al., 2015; Finnegan et al., 2021). Conventional PTT recording compares the delay between a central cardiac event and the arrival of the associated waveform at a distal site; a robust method of measuring PTT by distal measurements alone would enable highly convenient monitoring of arterial stiffness.

Wearable ballistocardiography is one approach to achieve this. The ballistocardiogram (BCG) results from the mechanical force transmitted through the body with the movement of blood through the heart and major arteries (Gordon, 1877; Starr et al., 1939). The primary component of the BCG, a complex of three distinctive, energetic deflections denoted I, J, and K, is associated with systole (Rappaport, 1956; Inan et al., 2015; Tavakolian et al., 2022). Recent BCG measurement developments aim for ubiquitous longitudinal cardiovascular monitoring, for example, heart rate (HR) monitoring (Jung et al., 2021; Czapanskiy et al., 2022). Amplitude and peak width of the IJK components have been associated with stroke volume (SV) and ejection duration (Starr, 1955; Inan et al., 2015; 2009b; Ashouri et al., 2016; Quesada et al., 2021). BCG morphological variation between individuals has limited its use, but mechanistic modeling of the waveform's complex origins is ongoing (Marazzi et al., 2022; Zaid et al., 2022).

Distally recorded BCG can be used to obtain a reasonable marker of aortic valve opening (AVO) by detecting the initial deflection of the I-wave, which occurs soon after the onset of rapid ejection. When combined with a distal marker of pulse wave arrival, such as photoplethysmography (PPG) or tonometry, this allows PTT calculation at a single distal location, enabling convenient recording with wearable sensors on distal limbs (Campo et al., 2017; Shin et al., 2022). Although a few applications of instrumented shoes have attempted to record the full-body force BCG (Liu et al., 2017; Gjerde et al., 2022), wearable ballistocardiography typically relies on accelerometry. Wrist-based accelerometers have shown the capability of detecting AVO at rest (Wiens et al., 2017), but the underlying physical mechanisms behind BCG morphology in the wrist are poorly understood (Kim et al., 2016; Yousefian et al., 2019; Shin et al., 2022).

There is limited research on wearable ballistocardiography during dynamic exercise. Morphology changes were noted in chest vibrations recorded during mild physical activity (Shandhi et al., 2021), and several studies have looked at BCG immediately post exercise (Inan et al., 2009a; Ashouri et al., 2016). Obtaining usable signals amidst severe motion artifacts presents a major challenge. However, as intensity increases, SV rises alongside HR, boosting cardiac output before plateauing with further increases driven by HR (Laughlin, 1999). We hypothesize that the systolic complex during physical activity may become more pronounced and distinguishable from motion artifacts associated with wrist BCG, given a reasonably stationary arm posture.

To enable new modalities of convenient wearable cardiovascular monitoring, our study aims to demonstrate the feasibility of wrist BCG measurements at comparatively high exercise intensity levels and to derive physiologically meaningful measures from them. We hypothesize that wrist BCG, segmented by tonometry, can be used as an AVO marker during exercise. We also investigate the relationship between BCG-PPG PTT and BP, as well as wrist BCG amplitude relative to left ventricle SV, during bike exercise with posture interventions.

We collected wrist accelerometry and radial artery arterial BP in healthy volunteers during a reclining bike exercise protocol. To address the low signal-to-noise (SNR) ratio of the wrist signal and the spectral instability of the systolic complex associated with AVO, we employed ensemble averaging and ensemble empirical mode decomposition (EEMD) to track the systolic complex of the BCG (Wu and Huang, 2011). We calculated BCG-PPG PTT and systolic BCG peak prominence across four discrete exercise levels in supine and semi-recumbent postures. Additionally, Doppler echocardiography of blood flow velocity in the left ventricle outflow tract (LVOT) confirmed the association of the wrist BCG signal with AVO and indicated a positive SV relationship with wrist BCG amplitude for a subset of participants with usable SV data. By examining wrist accelerometry and radial artery arterial BP during a reclining bike exercise protocol, we contribute to the understanding of wearable ballistocardiography and its potential applications in cardiovascular monitoring.

2 Materials and methods

2.1 Study protocol

2.1.1 Participants

The study protocol was reviewed and preapproved by the Regional Committee for Medical Ethics Central Norway, application number 62226. The use of an experimental medical device was approved by the Norwegian Medicines Agency (reference 21/06743). The study was registered with ClinicalTrials.gov with identifier NCT05008133.

Twenty-five healthy volunteers aged between 21–43 were recruited via public advertisement in Trondheim, Norway. Exclusion criteria were reduced manual circulation, diabetes, known cardiovascular disease or increased thrombogenic risk. Screening was conducted by a trained anesthesiologist and all participants provided written informed consent. A summary of participant demographics is presented in Table 1.

2.1.2 Device placement

The investigational device consisted of a wristband-mounted sensor unit, composed of a microcontroller, accelerometer, galvanic skin response electrodes and an array of pressure sensors for radial tonometry. Data from the device was recorded to PC via wired serial communication. The investigational device was fitted to the participant's wrist on the dominant arm (Figure 1). The arm

10.3389/fphys.2023.1189732

TABLE 1 Participant demographics.

	All (n = 25)	Males (n = 12)	Females (n = 13)
Age, years	32 (21–43)	28 (21–39)	37 (26–43)
Height, cm	174 (154–193)	179 (173–193)	163 (154–177)
Weight, kg	70 (52–92)	78 (70–92)	62 (52–82)
BMI	23.5 (18–27)	24.0 (22–26)	22.9 (18–27)
Handedness			
Right	24 (96%)	13 (100%)	12 (92%)
Left	1 (4%)	—	1 (8%)
bSBP, mmHg	124 (103–147)	129 (112–147)	120 (103–137)
bDBP, mmHg	81 (55–106)	82 (70–106)	81 (55–95)

Values are median with absolute ranges in brackets. BMI: body mass index, bSBP: brachial systolic blood pressure, bDBP: brachial diastolic blood pressure.

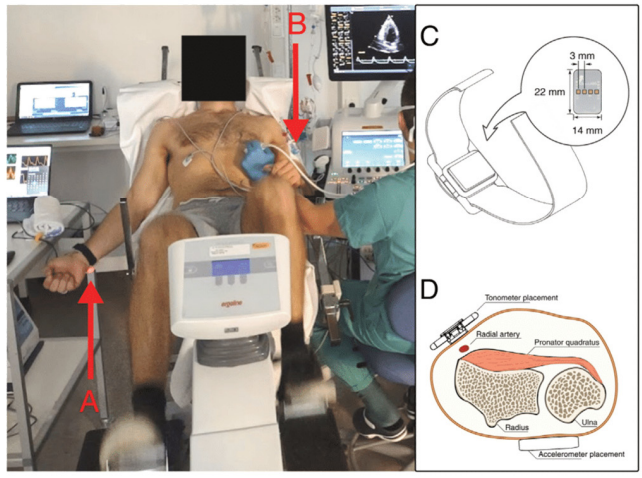

FIGURE 1
Left: Setup during semirecumbent sampling. **(A)** The investigational device is visible on the participant's right wrist. **(B)** The pressure transducer is fixed to the upper non-dominant arm, which is rested on the handle of the recumbent bike. Photo by written consent. Right: the investigational device. **(C)** Illustration of the tonometer wristband. **(D)** Sensor placement on the dominant arm.

hanged freely during exercise and relaxed on a bedside table during rest. Data from the sensors were recorded to a PC via wired serial communication.

2.1.3 Acceleration ballistocardiography

A 3-axis MEMS accelerometer (LISD3H, STMicroelectronics, Switzerland) embedded in the investigational device was used to record acceleration in the dominant wrist. The accelerometer was located on the posterior of the wrist, like a large wristwatch (Figure 1). The investigational device's output was recorded to PC via wired serial communication.

2.1.4 Tonometry

A wearable tonometer integrated in the same wristband was placed above the radial artery immediately below the wrist of participants' dominant hand. The device consisted of a linear array of silicone polymer-covered MEMS pressure sensors (BMP390, Bosch Sensortec Gmbh, Germany) to increase the viable placement area (Solberg et al., 2019).

2.1.5 Photoplethysmography

The photoplethysmogram is obtained by measuring the intensity of specific wavelengths of reflected light in the vascular

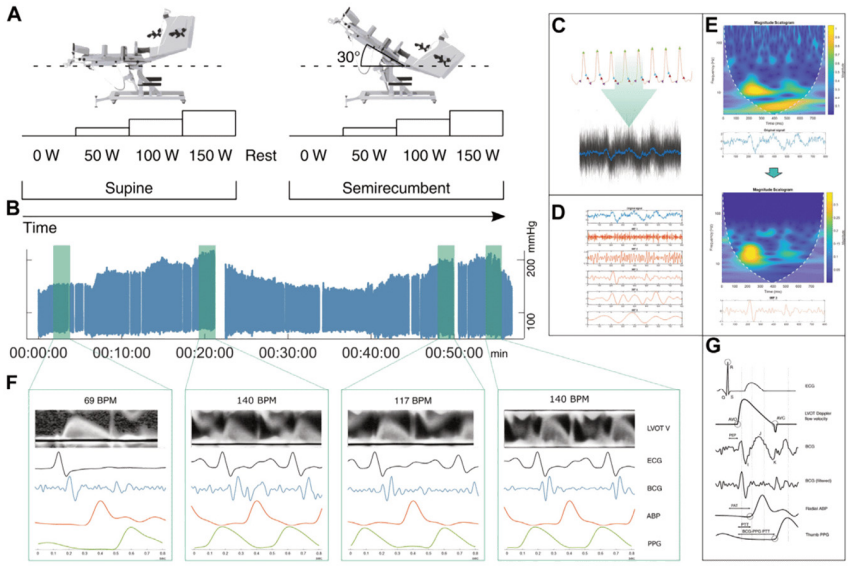

FIGURE 2
Graphical overview of data collection and data processing pipeline. **(A)** Schematic representation of exercise protocol. Each participant exercised freely at four different load levels from 0 to 150 Watts as defined by work delivered to the reclining ergometer bike, set via programmable dynamic resistance at 60 RPM. The ramping protocol was repeated for supine and semirecumbent posture with a rest and recovery period between. Rest took place in the semirecumbent posture. **(B)** Plot of ABP for one participant over the full session, roughly vertically aligned with the respective load states. **(C)** Raw accelerometer data is segmented into individual beats using systolic peaks as reference. Several segments form an ensemble average. **(D)** The average signal is decomposed via EEMD. **(E)** Time-frequency representation of the ensemble average and one of the IMFs. Top: The original signal. Bottom: Processed signal, emphasizing energy in the 10–30 Hz band. A temporally localized energetic feature appears to be isolated around the 200 ms mark. **(F)** Ensemble averaged signals between various exercise conditions, showing differences in wave morphology. Plotting the filtered BCG average against the ensemble averaged LVOT doppler flow images, ECG, and ABP, shows the correspondence of the identified high frequency BCG complex with the onset of rapid ejection. **(G)** Schematic diagram of the timing between signal features, illustrating the relationship between pre-ejection period (PEP), pulse arrival time (PAT), and pulse transit time (PTT). ABP: arterial blood pressure in radial artery, AVO: aortic valve opening, AOC: aortic valve closure, BCG: ballistocardiogram, ECG: electrocardiogram, EEMD: ensemble empirical mode decomposition, IMF: intrinsic mode function, LVOT-V: Left ventricle outflow tract velocity.

bed of well-perfused tissues. Transmission thumb PPG was recorded via the patient monitor and recorded to PC.

2.1.6 Doppler echocardiography

Continuous wave Doppler imaging was used to record local flow velocity in the left ventricle outflow tract (LVOT) (Vivid e95, GE Vingmed, Norway). Together with flow velocity, LVOT diameter was recorded to allow estimation of left ventricle stroke volume via the velocity-time integral.

2.1.7 Electrocardiography

3-lead ECG was recorded via the ultrasound machine.

2.1.8 Arterial blood pressure

Arterial blood pressure was recorded in the radial artery via arterial line transducer (Meritrans DTXPlus, Merit Medical Systems, United States). The radial artery of the non-dominant arm was cannulated following standard clinical procedure under ultrasound guidance. The transducer was fixed on the upper arm at the midaxillary line and zeroed to atmospheric pressure. The transducer output was input to the patient monitor (Intellivue MX800, Philips, Netherlands) and recorded to PC from the monitor at a recorded output data rate of 125 Hz. The transducer was re-zeroed between postural changes.

2.2 Data collection and preprocessing

2.2.1 Sampling protocol

The sampling sequence consisted of two sets of ergometer exercise at four intensity levels. The first set was performed with the participant lying supine, followed by a resting period of about 15 min. The ergometer was then tilted back to a semi-recumbent position, with the participant reclining at a 30° angle. The arterial line was re-zeroed between postures. Exercise intensity was measured in Watts delivered to the ergometer and controlled via programmable dynamic resistance. The exercise levels were 0, 50, 100, and 150 W, tilted in four increments. The experimental protocol and the test environment are shown in Figure 2. Participants were instructed to maintain as close to 60 RPM as

possible, which they could self-monitor via an integrated display. Participants exercised freely at each resistance level until HR and BP stabilized before measurements were taken. The pre-measurement period was at least 2 min followed by at least 2 min of measurements.

2.2.2 Timing signal

To allow synchronization of disparate signals, an electronic timing signal was generated by a PC running a custom MATLAB script. This signal was recorded across the recording PC, the ultrasound machine, and the investigational device. All signals were resampled to a common frequency and synchronized using the timing signal using R (R Core Team, Austria). The BP and PPG signals were recorded at 125 Hz, the ECG was recorded at 500 Hz, the tonometer at 200 Hz, and the accelerometer was sampled at 900 Hz.

2.2.3 Segmentation and ensemble averaging

BCG recorded from the wrist is noisier and more morphologically smooth than the full-body scale BCG, complicating identifying pertinent features in the signal. A common method to improve the signal to noise ratio is to take the ensemble average of multiple signal periods (Wiens et al., 2017). Figure 2 illustrates the processing pipeline from raw accelerometry data as described below.

Data from each sampling state was segmented using the systolic peak of the tonometry signal as a reference. To retain the systolic complex of the BCG and the foot of the following PPG signal, each segment was defined as 400 ms before and after the systolic peak of the accompanying radial pulse wave. Segmenting the signals to a known time range rather than from systole to systole simplified further analysis by having a common length of the signal vectors. To identify the BCG, the accelerometer axis corresponding to the head-foot axis was selected.

2.2.4 Signal decomposition

For each sampling condition, the mean of the segmented beats was calculated. This ensemble average was then decomposed using EEMD. EEMD is a noise-assisted data-adaptive method which has proven to be effective at decomposing noisy biological signals with unstable spectral components, such as BCG signals (Enayati, 2019). It decomposes a signal into so-called intrinsic mode functions (IMF), forming a basis from which the original signal can be reconstructed. The EEMD prioritizes signal features that are AM-FM modulated, implying retention of physically significant modes.

To assess performance of the EEMD, we compute wavelet scalograms to visualize the localization of signal power across the frequency spectrum. The wavelet transform is especially suited to identifying local transients in the time domain, and is suited for BCG analysis (Malik and Boger, 2021). Figure 2E shows scalograms from the ensemble average of unfiltered accelerometer traces from one participant, as well as a selected IMF of the same signal. The original signal appears to contain two major components, one in the 10–30 Hz region tightly localized in time, and a larger scale, more smeared-out component in the 1–10 Hz band. The higher frequency components are isolated in IMF #3, consisting of a significant complex of deflections between 200–300 ms (100–200 ms prior to the radial systolic peak). Identifying this as the systolic complex, a later, smaller complex can be seen about 250 ms later, tentatively identified as the diastolic complex. We identify the higher-frequency component isolated in IMF #3 as the complex associated with AVO in the work by Wiens et al. (2017); Figure 3 further shows scalograms of acceleration ensemble averages across the exercise protocol, alongside the decomposed signal and the root-mean-square (RMS) envelope of the filtered signal's power.

2.2.5 Determining PTT and BCG amplitude

Pulse transit time was determined as the time between the onset of the systolic complex in the ballistocardiogram and the foot of the following PPG systole as determined using the intersecting tangents method. The reference point signifying the onset of the BCG systole was defined as the peak immediately preceding the first major negative deflection in the EEMD-filtered BCG. The amplitude was determined as the prominence of the largest peak within 120 ms of the onset of BCG systole.

Figure 3 shows the ensemble averages of BCG and simultaneously recorded ECG, radial artery BP, and LVOT velocity. Time-frequency scalograms show signal magnitude concentrations in the time window between the ECG R-peak and the foot of the pressure pulse wave in the radial artery. In comparison to the LVOT Doppler velocity curves, the onset of the signal complex occurs soon after the onset of rapid ejection.

Doppler flow velocity recordings were automatically traced using a custom MATLAB script. Tracings were manually inspected and corrected when necessary. By integrating the flow velocity from onset of ejection to valve closing, SV can be calculated by multiplying the resulting velocity time integral by the area of the LVOT. SV estimates were obtained by multiplying the velocity time integral by the LVOT diameter as measured in the ultrasound B-mode view.

2.2.6 Hypothesis testing

Hypothesis testing was conducted using the two-sided Wilcoxon signed-rank test for paired data. The test calculates a test statistic describing the likelihood of the null hypothesis that the difference between two paired samples is from a distribution whose mean is zero. In each test case, observations from each participant in one condition were paired with the same participants' measurements in the comparison condition. In case of missing observations, the participant was excluded. The significance criteria for rejecting the null hypothesis of no difference between sample populations was set to $a = 0.05$. Correlation strengths between variables was compared using the cocor R package with dependent groups at $a = 0.05$ (Diedenhofen and Musch, 2015). Post-hoc comparison of group effects but not interaction effects was supported by a non-parametric factorial analysis using the Aligned Rank Transform (Supplementary Table S1; Wobbrock et al., 2011).

3 Results

Aggregate results are shown in Table 2 and Figure 4. Values are reported as mean with range except where otherwise noted.

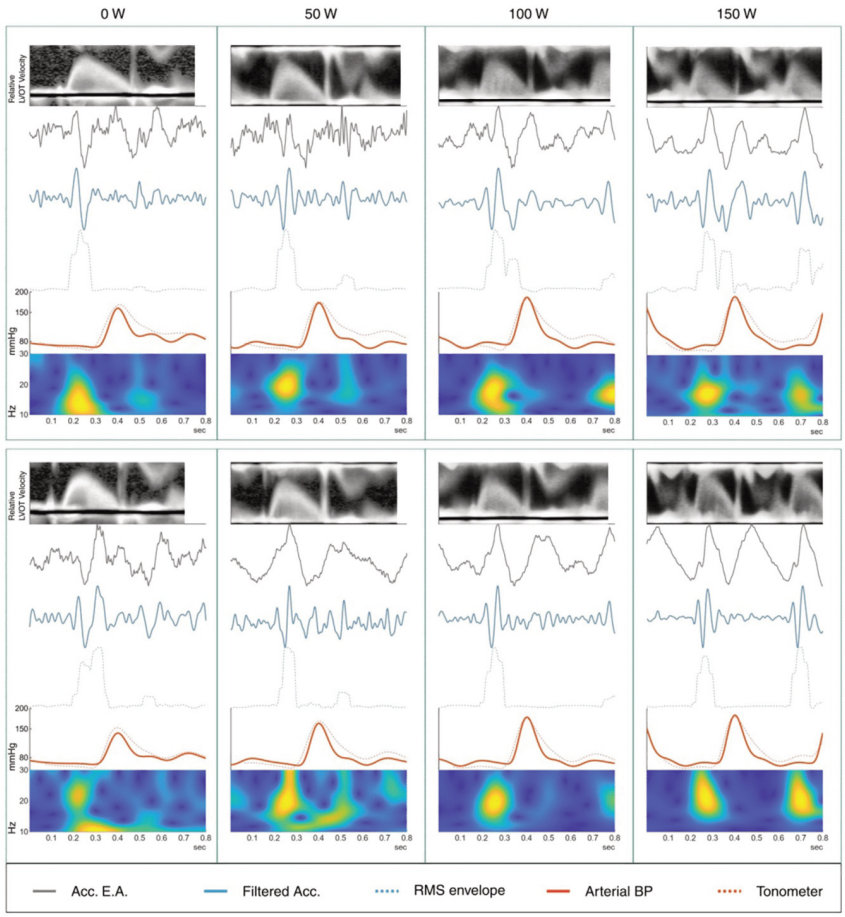

FIGURE 3
Ensemble averages from a male participant across all 8 exercise conditions. Top row is supine; bottom row is semirecumbent. At top, the averaged left ventricle outflow tract (LVOT) flow velocity shows onset of rapid ejection around 0.15–0.2 s followed by the "click" of the aortic valve closing at approximately 0.3–0.45 s. Below, the raw ensemble average of the accelerometer, followed by the filtered accelerometer signal with RMS envelope of the signal energy. Averaged arterial blood pressure (ABP) in the radial artery is shown together with the average tonometer signal, scaled to the magnitude of the ABP signal. Bottom: analytic morlet scalogram of the ensemble averaged accelerometer signals between 10 and 30 Hz. The sharp feature in the scalograms between 0.2 and 0.3 s seems to be clearly represented in the filtered BCG and is tentatively associated with rapid ejection from the ventricle.

3.1 Blood pressure during exercise

Systolic blood pressure increased with exercise load in both postures. Excluding two participants who interrupted the supine 150 W condition, the median increase from rest to 150 W was 62 (31.3–116.1) mmHg in the supine condition *versus* 60.7 (37.5–112.8) mmHg in the semirecumbent condition. Diastolic pressures varied less, with a median increase of 1.2 (−18.7–16.3) mmHg in supine *versus* 6.3 (−9.3–22.2) mmHg semirecumbent (Table 2). Systolic, diastolic, and mean arterial blood pressure was consistently lower in the semirecumbent posture than in the supine posture (Figure 4).

3.2 Heart rate

Heart rate increased linearly with exercise load, with similar increases between supine and semirecumbent conditions. Heart rate was slightly higher in the semirecumbent posture, but the difference was not consistently significant (Figure 4).

TABLE 2 Summary of results.

Intensity	0 W		50 W		100 W		150 W	
Posture	Supine	S.R.	Supine	S.R.	Supine	S.R.	Supine	S.R.
HR, bpm	69.0 ± 12.0	79.1 ± 15.4	101.2 ± 13.9	104.0 ± 16.4	123.0 ± 18.0	130.1 ± 20.8	144.0 ± 19.3	151.8 ± 20.6
SBP, mmHg	145.3 ± 15.8	129.6 ±19.1	170.5 ± 22.0	154.3 ± 20.6	194.1 ± 26.3	179.8 ± 23.4	207.7 ± 27.0	200.9 ± 29.5
DBP, mmHg	71.8 ± 7.4	65.2 ± 7.4	70.3 ± 5.7	63.4 ± 6.1	73.2 ± 6.0	66.8 ± 5.7	75.0 ± 6.9	69.2 ± 5.6
MAP, mmHg	95.2 ± 8.9	83.4 ± 9.6	93.7 ± 8.9	83.5 ± 8.7	101.7 ± 14.2	93.4 ± 12.7	111.3 ± 13.9	107.7 ± 16.5
PTT, ms	286.2 ± 25.2	263.1 ±23.6	260.0 ± 21.5	246.0 ± 30.3	237.8 ± 21.1	227.3 ± 23.2	219.6 ± 26.1	209.1 ± 27.8
Amp, μG	29.5 ± 15.2	31.7 ± 20.4	65.4 ± 37.8	52.3 ± 27.2	78.8 ± 35.8	88.6 ± 39.5	82.2 ± 38.0	98.2 ± 37.8

Data are mean ± one standard deviation. Amp, systolic amplitude of filtered BCG, signal; DBP, diastolic blood pressure in radial artery; HR, heart rate; MAP, mean arterial pressure in radial artery; PTT, BCG-PPG, pulse transit time; SBP, systolic blood pressure in radial artery; S.R., Semirecumbent. blood pressure values are in the radial artery via arterial line.

3.3 BCG-PPG PTT

PTT decreased with exercise load in both supine and semirecumbent states (Table 2; Figure 4). Semirecumbent PTT was significantly lower than supine throughout, although the difference became less clear with increasing workload ($p < 0.001$ for 0 and 50 W, $p_{100W} = 0.0135$, $p_{150W} = 0.031$).

PTT exhibited a moderate negative correlation with radial SBP (Figure 4). The correlation was strength was slightly elevated in the supine condition compared to the semirecumbent, as well as the total ($\rho_{Sup} = -0.65$ vs. $\rho_{SR} = -0.57$, $\rho_{All} = -0.54$), but this difference was not statistically significant. PTT had a clear negative correlation with increasing HR ($\rho_{All} = -0.71$), but with little distinguishable difference between postures (Figure 4).

3.4 BCG amplitude

Systolic amplitude in the BCG signal increased significantly from rest at 0 W (32.4 ± 18.5) to 50 W (65.4 ± 37.8) ($p = 0.002$) and from 50 to 100 W (86.8 ± 38.0) ($p < 0.001$) (Table 2), but the difference between 100 and 150 W was not significant ($p = 0.24$). There was wide variation between participants, but the mean amplitude increased threefold between rest and 150 W in both postures, reaching close to maximum value at 100 W. There was not a significant difference in amplitude between supine and semirecumbent exercise across all conditions or between individual conditions.

3.5 Stroke volumes

The LVOT Doppler velocity recordings during exercise were characterized by large amounts of noise, complicating VTI calculation. A subset of 7 participants with relatively clean recording series were selected and stroke volumes calculated via LVOT VTI. Normalized SV data for both postures is plotted against BCG amplitude in Figure 4, section C In this small subsample, BCG amplitude increases with SV ($\rho = 0.54$). Excluding outliers according to robust Mahalanobis distance estimates (Leys et al., 2018), the correlation across all sample conditions increased to $\rho = 0.74$ (Figure 4). Excluding outliers could be motivated by presupposing low data quality.

4 Discussion

4.1 AVO detection

Comparing the averaged and filtered BCG signals with the Doppler velocity in the LVOT shows a high frequency BCG complex occurring shortly after the onset of rapid ejection, identified by the sudden rapid increase in flow velocity in the LVOT (Figure 3). This temporal relationship continues with increasing heart rate. The initial deflection of the higher-frequency bands of the wrist BCG, around 10–40 Hz, seems to reliably mark the beginning of ventricular ejection to within a few milliseconds. It is notable that the increase in BCG amplitude with increasing exercise load may make the features of interest easier to detect than during rest or low activity, when the small signal amplitude can get lost in noise and even small motion artifacts.

Using BCG as a proximal marker of AVO and onset of ejection has been demonstrated using full-body force plate BCG, for example, by Inan et al. alongside LVOT echocardiography (Inan et al., 2009a). Wiens et al. further examined the use of wrist BCG to mark AVO (Wiens et al., 2017).

4.2 Amplitude

The amplitude of the systolic complex increased rapidly from rest to 50 and again from 50 to 100 W but leveled off between 100 and 150 W. While increases from 0 to 50 and 50–100 W were each significant ($p < 0.01$), there was no statistically significant difference between 100 and 150 W in either exercise condition. This is consistent with the hypothesis that the energy content (e.g., amplitude and peak width) of the BCG is closely related to SV, which is expected to increase linearly with HR until plateauing as ventricular filling capacity is reached. Further increase in CO then becomes primarily driven by an increase in HR. Indeed, the same leveling off at 100–150 W appears in the limited SV data available (Figure 4). Systolic amplitude corresponding to SV makes intuitive sense if interpreted as a marker of the mechanical energy delivered into the cardiovascular system per heartbeat (Inan et al., 2015). The relationship between mechanical energy in BCG and similar systems and SV, together with systolic timing intervals, has been exploited

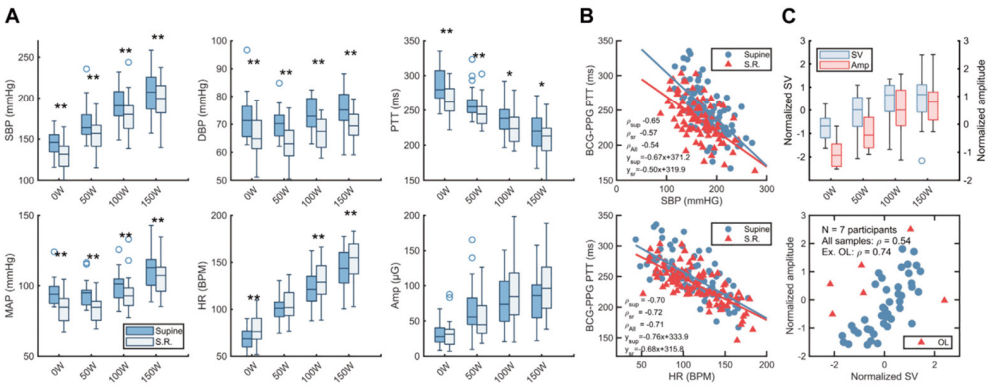

FIGURE 4
Hemodynamics between exercise states. **(A)** box charts showing distribution of systolic blood pressure (SBP), diastolic blood pressure (DBP), mean arterial pressure (MAP), heart rate (HR), BCG-PPG pulse transit time (PTT) and systolic BCG amplitude. Circles are outliers. Stars indicate significance of difference between postures via two-tailed Wilcoxon signed rank test at two different significance levels: **: $a < 0.01$, *: $a < 0.05$. **(B)** Top: scatterplot of SBP vs. BCG-PPG PTT with least-square regression lines. Bottom: scatterplot of BCG-PPG PTT vs HR. ρ is Pearson's correlation coefficient. **(C)** Top: bar chart of normalized left ventricle stroke volumes *versus* BCG amplitude across exercise conditions. Bottom: scatterplot of systolic BCG amplitude *versus* left ventricle stroke volume (SV). SV data was only available from a subset of participants. OL indicates outliers determined via the robust Mahalanobis distance at a chi-square significance level of 0.05. SV and amplitude data were normalized by z-scoring across the entire sample.

for assessment of markers of cardiovascular function such as cardiac output and oxygen uptake (Inan et al., 2009a; Shandhi et al., 2021).

Amplitude did not differ significantly between supine and semirecumbent posture. The large variance in the collected data may hide any significant differences, although it is acknowledged that BCG morphology varies substantially between individuals, reflecting differences in vascular anatomy and body composition (Starr, 1955). This variation complicates detailed morphological analysis.

Difference in coupling between the mass of the body and the supporting surface has been proposed as a contributor to posture variability in the wrist ballistocardiogram morphology (Shin et al., 2022). In this study, participants were lying on the same recumbent bicycle for the duration of the test protocol. As such the difference in mechanical coupling should be lessened between postures, although the action of the center of mass changed.

4.3 Postural effects

4.3.1 PTT

We observed significantly lower PTT in the semirecumbent state. Our findings are consistent with Shin et al. who noted significant differences in BCG-PPG PTT recorded at the wrist between upright and supine postures at rest (Shin et al., 2022). In their study, supine PTT was approximately ~20 ms higher than standing and sitting, which were not significantly different. This is in line with our observations for PTT at rest and during mild exercise (Figure 4). At higher intensities of exercise (100 and 150 W) the difference in PTT was less pronounced.

Both changes in the distending pressure in the arteries and sympathetic nerve action cause changes in arterial elasticity during dynamic exercise (Agnoletti, 2018). We observed a slight, but inconsistent increase in HR between supine and recumbent postures, while MAP remained lower in the semirecumbent position. Lefferts et al. also noted increases in arterial stiffness following acute exercise, which may be a separate confounder in our data as the rest period between each postural condition was not very long (Lefferts et al., 2018).

The difference in systolic BP and MAP between supine and semirecumbent situations may go some way to explain the disparity in PTT at rest and at light exercise. However, arterial stiffness measured via pulse wave velocity has been reported to increase between supine and semi-upright upper-body position independent of significant changes in height-corrected BP (Schroeder et al., 2017). The exact cause of this disparity in PTT between postures seems unclear. In the case of wrist based BCG measurement, Shin et al. propose hydrostatic effects between measurement sites in the upper and lower arm (Shin et al., 2022), but as we recorded BP in the lower arm we would expect to see a consistently higher BP in the semirecumbent state if the decrease in PTT were to be driven by increased BP in the peripheral limb, which is the opposite of what we observed.

4.3.2 Blood pressure

While SBP, DBP and MAP all increased with exercise intensity, BP was consistently and significantly higher in the supine posture. Part of the observed effect could be influenced by exercise-induced hypotension in the semirecumbent condition, given the short rest period between postures (Carpio-Rivera et al., 2016), but increased upper limb BP in the supine condition as compared to sitting or semi-upright postures has been previously demonstrated (Netea et al., 2003; Watanabe et al., 2007). In the context of ergometer exercise, decreased gross efficiency in the supine condition compared to recumbent exercise state at 70 W has been shown, hypothesized to be primarily due to height differences between the heart and the working muscles in turn affecting cardiovascular performance during exercise (Wehrle et al., 2021).

4.4 Study limitations

The low signal-to-noise ratio of the acceleration measurements makes continuous beat-to-beat recording of the systolic complex difficult. An inexpensive accelerometer with a noise floor of 220 μg/$\sqrt{Hz}$ was used. A low accelerometer noise floor has been reported to improve signal quality in wearable applications (Shandhi et al., 2021). The use of ensemble averages is predicated on the assumption that the signals are locally stationary, which limits the applicability of this approach as HR varies dynamically with exercise. Accelerometers with lower noise floors may allow smaller ensembles to be averaged to produce a usable signal in more dynamic exercise use cases.

A weakness of the present study lies in the use of steady state exercise. Steady exercise conditions allow multiple heartbeats to be averaged, mitigating signal quality issues to a degree. This approach however removes some of the variance in the averaged data (breathing cycles, for instance) which may be of interest. The steady states examined here may furthermore not be directly comparable to many uncontrolled exercise conditions where exertion levels might vary more dynamically. Application in more realistic exercise situations requires further work in instrumentation and signal processing to handle motion artifacts and enable the use of shorter ensemble windows. The sample size of the current study is in any case small, and extrapolation to larger populations may also be complicated by the homogenous makeup of the participant group.

The four exercise load levels–set to absolute levels of delivered work–allow for intra-individual comparison across a linearly increasing load, but individual response at each level will vary significantly. In the absence of quantitative measures of perceived exertion, i.e., Borg scale ratings, inter-individual comparisons must be made with caution.

Segmentation of the signal using BP waveforms offers interesting opportunities in combination with wearable tonometry. ECG, often used for waveform segmentation, is difficult to acquire at the wrist in a passive scenario, requiring extra leads or intentional contact to another body part. Similarly, the PPG waveform is often morphologically smooth, making consistent determination of reference points challenging. With adequate contact force, radial tonometry could provide a reliable segmentation reference for wearable applications.

5 Conclusion

Acceleration ballistocardiograms may be recorded at the wrist even during relatively high exercise loads. A secondary sensor mode acting as a reference allows segmentation of the signal and the creation of ensemble averages, from which timing references closely following AVO can be obtained at significantly elevated HR. By combining the BCG-derived proximal cardiac reference with a reference of the arrival of a peripheral pulse wave, estimates of PTT may be calculated in this way.

PTT decreased with increasing exercise load, closely following HR trends. Like both systolic, mean, and diastolic arterial blood pressure, PTT was lower in the semirecumbent posture, while HR was higher in this state. Consequently, while PTT showed clear correlation with both systolic BP and HR, not all the variance in PTT may be explained by increase in HR alone.

Convenient PTT measurement during exercise may enable broader studies of cardiovascular response to acute exercise outside the lab setting, which in turn may facilitate more naturalistic monitoring of cardiovascular performance in persons with CVD risk.

Data availability statement

The raw data supporting the conclusion of this article will be made available by the authors, without undue reservation.

Ethics statement

The studies involving human participants were reviewed and approved by Regional Committee for Medical Ethics Central Norway. The patients/participants provided their written informed consent to participate in this study. Written informed consent was obtained from the individual(s) for the publication of any potentially identifiable images or data included in this article.

Author contributions

TS, EI, HF, and IK-G conceptualized the study. TS, HF, and IK-G performed the experiment and collected the data. FES organized the data. TS wrote the code and analysed the results with input from FES, IK-G, and TS, FSS, and MS designed and constructed the investigational device. HF and IK-G were responsible for the clinical aspect of the study. TS led the writing of the manuscript. All authors reviewed the manuscript and approved the submitted version. All authors contributed to the article and approved the submitted version.

Conflict of interest

The authors declare that the research was conducted in the absence of any commercial or financial relationships that could be construed as a potential conflict of interest.

Publisher's note

Supplementary material

The Supplementary Material for this article can be found online at: https://www.frontiersin.org/articles/10.3389/fphys.2023.1189732/full#supplementary-material

References

Agnoletti, D. (2018). The aerobic exercise training in hypertension: A matter of baking ingredients. *J. Hypertens.* 36, 1651–1653. doi:10.1097/HJH.0000000000001776

Ashouri, H., Orlandic, L., and Inan, O. T. (2016). Unobtrusive estimation of cardiac contractility and stroke volume changes using ballistocardiogram measurements on a high bandwidth force plate. *Sensors* 16, 787. doi:10.3390/s16060787

Campo, D., Khettab, H., Yu, R., Genain, N., Edouard, P., Buard, N., et al. (2017). Measurement of aortic pulse wave velocity with a connected bathroom scale. *Am. J. Hypertens.* 30, 876–883. doi:10.1093/ajh/hpx059

Carpio-Rivera, E., Moncada-Jiménez, J., Salazar-Rojas, W., and Solera-Herrera, A. (2016). Acute effects of exercise on blood pressure: A meta-analytic investigation. *Arq. Bras. Cardiol.* 106, 422–433. doi:10.5935/abc.20160064

Czapanskiy, M. F., Ponganis, P. J., Fahlbusch, J. A., Schmitt, T. L., and Goldbogen, J. A. (2022). An accelerometer-derived ballistocardiogram method for detecting heart rate in free-ranging marine mammals. *J. Exp. Biol.* 225, jeb243872. doi:10.1242/jeb.243872

Diedenhofen, B., and Musch, J. (2015). Cocor: A comprehensive solution for the statistical comparison of correlations. *PLOS ONE* 10, e0121945. doi:10.1371/journal.pone.0121945

Enayati, M. (2019). Data-driven methods for analyzing ballistocardiograms in longitudinal cardiovascular monitoring. Available at: https://mospace.umsystem.edu/xmlui/handle/10355/72208 (Accessed November 11, 2022).

Finnegan, E., Davidson, S., Harford, M., Jorge, J., Watkinson, P., Young, D., et al. (2021). Pulse arrival time as a surrogate of blood pressure. *Sci. Rep.* 11, 22767. doi:10.1038/s41598-021-01358-4

Geddes, L. A., Voelz, M. H., Babbs, C. F., Bourland, J. D., and Tacker, W. A. (1981). Pulse transit time as an indicator of arterial blood pressure. *Psychophysiology* 18, 71–74. doi:10.1111/j.1469-8986.1981.tb01545.x

Gjerde, S. G., Steffensen, T. L., Vestad, H. N., and Steinert, M. (2022). "Windows to the sole: Prototyping soft sensors for wearable ballistocardiography," in 2022 IEEE 18th International Conference on Wearable and Implantable Body Sensor Networks (BSN), Ioannina, Greece, Sep 26, 2022 - Sep 30, 2022.

Gordon, J. W. (1877). Certain molar movements of the human body produced by the circulation of the blood. *J. Anat. Physiol.* 11, 533–536.

Inan, O. T., Etemadi, M., Paloma, A., Giovangrandi, L., and Kovacs, G. T. A. (2009a). Non-invasive cardiac output trending during exercise recovery on a bathroom-scale-based ballistocardiograph. *Physiol. Meas.* 30, 261–274. doi:10.1088/0967-3334/30/3/003

Inan, O. T., Etemadi, M., Wiard, R. M., Giovangrandi, L., and Kovacs, G. T. A. (2009b). Robust ballistocardiogram acquisition for home monitoring. *Physiol. Meas.* 30, 169–185. doi:10.1088/0967-3334/30/2/005

Inan, O. T., Migeotte, P.-F., Park, K.-S., Etemadi, M., Tavakolian, K., Casanella, R., et al. (2015). Ballistocardiography and seismocardiography: A review of recent advances. *IEEE J. Biomed. Health Inf.* 19, 1414–1427. doi:10.1109/JBHI.2014.2361732

Jung, H., Kimball, J. P., Receveur, T., Agdeppa, E. D., and Inan, O. T. (2021). Accurate ballistocardiogram based heart rate estimation using an array of load cells in a hospital bed. *IEEE J. Biomed. Health Inf.* 25, 3373–3383. doi:10.1109/JBHI.2021.3066885

Kim, C.-S., Carek, A. M., Mukkamala, R., Inan, O. T., and Hahn, J.-O. (2015). Ballistocardiogram as proximal timing reference for pulse transit time measurement: Potential for cuffless blood pressure monitoring. *IEEE Trans. Biomed. Eng.* 62, 2657–2664. doi:10.1109/TBME.2015.2440291

Kim, C.-S., Ober, S. L., McMurtry, M. S., Finegan, B. A., Inan, O. T., Mukkamala, R., et al. (2016). Ballistocardiogram: Mechanism and potential for unobtrusive cardiovascular health monitoring. *Sci. Rep.* 6, 31297. doi:10.1038/srep31297

Laughlin, M. H. (1999). Cardiovascular response to exercise. *Adv. Physiology Educ.* 277, S244–S259. doi:10.1152/advances.1999.277.6.S244

Lefferts, W. K., DeBlois, J. P., Receno, C. N., Barreira, T. V., Brutsaert, T. D., Carhart, R. L., et al. (2018). Effects of acute aerobic exercise on arterial stiffness and cerebrovascular pulsatility in adults with and without hypertension. *J. Hypertens.* 36, 1743–1752. doi:10.1097/HJH.0000000000001752

Leys, C., Klein, O., Dominicy, Y., and Ley, C. (2018). Detecting multivariate outliers: Use a robust variant of the Mahalanobis distance. *J. Exp. Soc. Psychol.* 74, 150–156. doi:10.1016/j.jesp.2017.09.011

Liu, M., Jiang, F., Jiang, H., Ye, S., and Chen, H. (2017). Tree diversity regulates soil respiration through elevated tree growth in a microcosm experiment. *Comput. Industry* 91, 24–28. doi:10.1016/j.pedobi.2017.05.005

Liu, Q., Yan, B. P., Yu, C.-M., Zhang, Y.-T., and Poon, C. C. Y. (2014). Attenuation of systolic blood pressure and pulse transit time hysteresis during exercise and recovery in cardiovascular patients. *IEEE Trans. Biomed. Eng.* 61, 346–352. doi:10.1109/TBME.2013.2286998

Malik, A. R., and Boger, J. (2021). Zero-effort ambient heart rate monitoring using ballistocardiography detected through a seat cushion: Prototype development and preliminary study. *JMIR Rehabilitation Assistive Technol.* 8, e25996. doi:10.2196/25996

Marazzi, N. M., Guidoboni, G., Zaid, M., Sala, L., Ahmad, S., Despins, L., et al. (2022). Combining physiology-based modeling and evolutionary algorithms for personalized, noninvasive cardiovascular assessment based on electrocardiography and ballistocardiography. *Front. Physiology* 12, 739035. doi:10.3389/fphys.2021.739035

Miyai, N., Arita, M., Miyashita, K., Morioka, I., Shiraishi, T., and Nishio, I. (2002). Blood pressure response to heart rate during exercise test and risk of future hypertension. *Hypertension* 39, 761–766. doi:10.1161/hy0302.105777

Netea, R. T., Lenders, J. W. M., Smits, P., and Thien, T. (2003). Both body and arm position significantly influence blood pressure measurement. *J. Hum. Hypertens.* 17, 459–462. doi:10.1038/sj.jhh.1001573

Quesada, O., Shandhi, M. M. H., Beach, S., Dowling, S., Tandon, D., Heller, J., et al. (2021). Use of ballistocardiography to monitor cardiovascular hemodynamics in preeclampsia. *Womens Health Rep. New. Rochelle)* 2, 97–105. doi:10.1089/whr.2020.0127

Rappaport, M. B. (1956). Displacement, velocity, and acceleration ballistocardiograms as registered with an undamped bed of ultralow natural frequency. III. The normal ballistocardiogram. *Am. Heart J.* 52, 847–857. doi:10.1016/0002-8703(56)90151-x

Schroeder, E. C., Rosenberg, A. J., Hilgenkamp, T. I. M., White, D. W., Baynard, T., and Fernhall, B. (2017). Effect of upper body position on arterial stiffness: Influence of hydrostatic pressure and autonomic function. *J. Hypertens.* 35, 2454–2461. doi:10.1097/HJH.0000000000001481

Shandhi, M. M. H., Bartlett, W. H., Heller, J. A., Etemadi, M., Young, A., Plötz, T., et al. (2021). Estimation of instantaneous oxygen uptake during exercise and daily activities using a wearable cardio-electromechanical and environmental sensor. *IEEE J. Biomed. Health Inf.* 25, 634–646. doi:10.1109/JBHI.2020.3009903

Shin, S., Mousavi, A. S., Lyle, S., Jang, E., Yousefian, P., Mukkamala, R., et al. (2022). Posture-dependent variability in wrist ballistocardiogram-photoplethysmogram pulse transit time: Implication to cuff-less blood pressure tracking. *IEEE Trans. Biomed. Eng.* 69, 347–355. doi:10.1109/TBME.2021.3094200

Solberg, F. S., Kohtala, S., Vestad, H., and Steinert, M. (2019). "A combined photoplethysmography and force sensor prototype for improved pulse waveform analysis," in 2019 ieee Sensors, Montreal, QC, Canada, 27-30 October 2019, 1–4. doi:10.1109/SENSORS43011.2019.8956487

Starr, I., Rawson, A. J., Schroeder, H. A., and Joseph, N. R. (1939). Studies on the estimation of cardiac ouptut in man, and of abnormalities in cardiac function, from the heart's recoil and the blood's impacts; the ballistocardiogram. *Am. J. Physiology-Legacy Content* 127, 1–28. doi:10.1152/ajplegacy.1939.127.1.1

Starr, I. (1955). Studies made by simulating systole at necropsy. VI. Estimation of cardiac stroke volume from the ballistocardiogram. *J. Appl. Physiol.* 8, 315–329. doi:10.1152/jappl.1955.8.3.315

Tavakolian, K., Inan, O. T., Hahn, J.-O., and Di Rienzo, M. (2022). Editorial: Cardiac vibration signals: Old techniques, new tricks, and applications. *Front. Physiology* 13, 931362. doi:10.3389/fphys.2022.931362

Thanassoulis, G., Lyass, A., Benjamin, E. J., Larson, M. G., Vita, J. A., Levy, D., et al. (2012). Relations of exercise blood pressure response to cardiovascular risk factors and vascular function in the framingham heart study. *Circulation* 125, 2836–2843. doi:10.1161/CIRCULATIONAHA.111.063933

Watanabe, N., Reece, J., and Polus, B. I. (2007). Effects of body position on autonomic regulation of cardiovascular function in young, healthy adults. *Chiropr. Man. Ther.* 15, 19. doi:10.1186/1746-1340-15-19

Wehrle, A., Waibel, S., Gollhofer, A., and Roecker, K. (2021). Power output and efficiency during supine, recumbent, and upright cycle ergometry. *Front. Sports Act. Living* 3, 667564. doi:10.3389/fspor.2021.667564

Wiens, A. D., Johnson, A., and Inan, O. T. (2017). Wearable sensing of cardiac timing intervals from cardiogenic limb vibration signals. *IEEE Sensors J.* 17, 1463–1470. doi:10.1109/JSEN.2016.2643780

Wobbrock, J. O., Findlater, L., Gergle, D., and Higgins, J. J. (2011). "The aligned rank transform for nonparametric factorial analyses using only anova procedures," in *Proceedings of the SIGCHI conference on human factors in computing systems CHI '11* (New York, NY, USA: Association for Computing Machinery), 143–146. doi:10.1145/1978942.1978963

Wu, Z., and Huang, N. E. (2011). Ensemble empirical mode decomposition: A noise-assisted data analysis method. *Adv. Adapt. Data Analysis* 01, 1–41. doi:10.1142/S1793536909000047

Yousefian, P., Shin, S., Mousavi, A. S., Kim, C.-S., Finegan, B., McMurtry, M. S., et al. (2019). Physiological association between limb ballistocardiogram and arterial blood pressure waveforms: A mathematical model-based analysis. *Sci. Rep.* 9, 5146. doi:10.1038/s41598-019-41537-y

Zaid, M., Sala, L., Ivey, J. R., Tharp, D. L., Mueller, C. M., Thorne, P. K., et al. (2022). Mechanism-driven modeling to aid non-invasive monitoring of cardiac function via ballistocardiography. *Front. Med. Technol.* 4, 788264. doi:10.3389/fmedt.2022.788264

145

C4. Cuffless estimation of continuous blood pressure during recumbent bike exercise: comparison of wearable tonometry and PPG against invasive ground-truth measurements

Abstract, manuscript in preparation

Torjus Lines Steffensen, Filip Emil Schjerven, Hans Martin Flade, Idar Kirkeby-Garstad, Emma Ingeström, Fredrik Samdal Solberg, and Martin Steinert

This paper is awaiting publication and is therefore not included.

Cuffless estimation of continuous blood pressure during recumbent bike exercise using wearable tonometry and invasive ground-truth measurements

Torjus L. Steffensen[1], Filip E. Schjerven[2], Hans M. Flade[1,3], Idar Kirkeby-Garstad[1,3], Emma Ingeström[1], Fredrik S. Solberg[4], and Martin Steinert[5]

[1]Department of Circulation and Medical Imaging, Norwegian University of Science and Technology, Trondheim, Norway
[2]Department of Computer Science, Norwegian University of Science and Technology, Trondheim, Norway
[3]St. Olav's University Hospital, Trondheim, Norway
[4]Department of Mechanical Engineering, Stanford University, Palo Alto, California, USA
[5]Department of Mechanical Engineering, Norwegian University of Science and Technology, Trondheim, Norway

Abstract

Objective: This pilot study aimed to estimate blood pressure (BP) during recumbent bike exercise in healthy volunteers using non-invasive and cuffless methods. Cardiovascular responses to exercise, such as BP, can be risk markers for cardiovascular events. Most cuffless BP estimation work is focused on rest conditions, leaving a research gap for exercise conditions. We aimed to contribute to cuffless BP sensor development by collecting data in a controlled exercise context.

Methods: 25 healthy volunteers were included in a dual-posture ramping exercise protocol performed on a recumbent bicycle. Primary measurements were collected using invasive BP via radial artery catheter, ECG, and PPG, tonometry, and accelerometry from an investigational device. A 1-dimensional convolutional neural network (CNN) was trained using downsampled individual tonometry beat waveforms for systolic BP estimation. The model was trained and tested using a leave-one-subject-out scheme, assessing its performance on unseen data.

Results: The CNN model demonstrated a broad range of Mean Absolute Error (MAE) between participants (7.6 to 27.9 mmHg, mean 15.2 mmHg), suggesting variations in the model's ability to capture individual physiological responses. Nonetheless, a reasonably high average correlation (Spearman's rank correlation, ρ_{Mean} = 0.79, range 0.39 to 0.96) was achieved between the model predictions and the ground truth. This result implies that while the model did not provide a satisfactory generalization, it captured drastic changes in systolic BP during exercise.

Significance: This work adds to the literature demonstrating potential of noninvasive waveform data for continuously estimating BP during exercise. Continuously tracking trends and relative changes from baseline BP could be valuable for applications such as post-surgery recovery monitoring, detecting postural hypotension, or sports performance evaluation. Further advancements could improve calibration with the inclusion of additional sensor data and explore the potential of these models for cardiovascular disease risk assessment.

C5. Ultrasound phantom

United States Patent No. US20220304922A1. Pending.

Torjus Lines Steffensen, Carlo Kriesi, Martin Steinert, Thomas Lafrenz, Jostein Rødseth Brede, and Marius Auflem

This is a pending patent and is not included.

C6. TrollBOT: A Spontaneous Networking Tool Facilitating Rapid Prototyping of Wirelessly Communicating Products

Procedia CIRP, 2020

Torjus Lines Steffensen, Sampsa Kohtala, Håvard Vestad, and Martin Steinert

Available online at www.sciencedirect.com

ScienceDirect

Procedia CIRP 91 (2020) 634–638

www.elsevier.com/locate/procedia

30th CIRP Design 2020 (CIRP Design 2020)

TrollBOT: A Spontaneous Networking Tool Facilitating Rapid Prototyping of Wirelessly Communicating Products

Torjus Steffensen*, Sampsa Kohtala, Håvard Vestad, Martin Steinert

NTNU – Norwegian University of Science and Technology – Department of Mechanical and Industrial Engineering, Richard Birkelands vei 2B, 7491 Trondheim, Norway

* Corresponding author. *E-mail address:* torjus.l.steffensen@ntnu.no

Abstract

In early stages of product development, prototyping is an invaluable tool which allows designers to generate learnings and uncover unknown challenges which can be used to further construct design requirements. While generous use of prototyping early in the design process might reduce the risk of premature design decisions, it also demands significant investments in terms of resources such as time, material, and skills. Tools that allow designers to rapidly implement and test new functionalities are therefore desired. With wirelessly communicating products having become ubiquitous in modern society, designers should be comfortable designing products utilizing these technologies. In this paper we present an Arduino library, named TrollBOT, that facilitates rapid implementation of wireless communication between two or more Arduinos. The Arduinos form nodes in a tree topology using inexpensive nRF24-based radio transceivers. The library is constructed in such a way that a minimal amount of new language syntax must be learned. All nodes can be programmed from a single master node in an intuitive manner, significantly reducing the amount of code that needs to be written as compared to similar existing solutions.

Keywords: Prototyping; Makerspaces; Arduino

1. Introduction

Prototyping is an essential part of the product development process [1] and utilizing prototyping efficiently as a tool to make informed design decisions is an invaluable asset to design teams. Where a prototype may be in the form of both physical, digital, or analytical models, all prototypes aim to answer important design questions and gain insights for the design process [2]. Thus, value created by a prototype is also the insights and learnings gained independently from the prototypes' resolution and fidelity. Emphasizing on these learnings through the implementation of fast, low resolution prototyping can be an important way to uncover unknown problems, but also important opportunities to the design team [3]. As such, prototyping can be used not only to verify whether a solution fits pre-decided requirements, but also to derive and form the product requirements based on learnings from explorative prototyping [4]. We call this prototyping in the pre-requirement space.

While thorough exploration of the problem and solution space early in the process aims to combat premature design decisions [5], both material resources, tools, and work hours are evident costs. Less evident, but not less important, is the education and training of the designers in the necessary skills to carry out the needed prototyping. In ever more multidisciplinary product development, education of users is one of the main challenges facing creative spaces and makerspaces [6]. Creating tools that lower the skill threshold for trying out technologies and solutions could greatly reduce the associated cost with such prototyping activities and potentially enable higher resolution prototypes in shorter timeframes.

10.1016/j.procir.2020.03.111

In this paper we present one such tool, called TrollBOT. The Arduino library TrollBOT was developed as an internal tool for use at TrollLABS, a makerspace like academic research lab located at the Norwegian University of Science and Technology. TrollLABS is dedicated to creating an environment for product development project work as well as research based on the applied methods and outcome via providing access to tools, machinery and materials appropriate for creating prototypes of different levels of complexity [7]. TrollBOT was developed by a three-student team as part of their coursework for TMM4245 "Fuzzy Front End", taught at TrollLABS. The library was a result of the team's efforts into enabling faster and easier prototyping of robotics concepts and features a low effort way of programming different functional Arduino-nodes to communicate and send signals using radio frequencies (RF).

1.1. RF communication and Arduino

Wireless communication between electronic devices has become increasingly ubiquitous in every aspect of our lives. From household consumer electronics to industrial tracking systems, our society is dependent on these technologies.

Today most applications of low-power, short-distance radiofrequency (RF) communications, including many devices in the Internet-of-Things (IoT) paradigm, take place in the ISM bands. These are ranges of the electromagnetic frequency spectrum that generally do not require government licensing to operate in, and consequently see much consumer and industrial application. For example, the Bluetooth standard operates in the 2.4 GHz band, and Wi-Fi, based on the IEEE 802.11 standard, primarily operates in the 2.4 and 5.0 GHz bands. Most programmable radio transceivers available to consumers are also designed to operate in these frequency ranges.

For the purpose of rapidly iterating prototypes of wirelessly communicating products, RF modules that are easily controllable via a development board such as Arduino is desirable. The Arduino platform is a simple ATmega328-based microcontroller, programmed in C or C++ via a minimalist integrated development environment (IDE). Commonly used in engineering education [8,9], its simplicity, ease of use and low cost make it especially well-suited for simple projects and rapid prototyping applications.

Several small, low-power RF transceivers compatible with Arduino are commonly available. One module based on the nRF24L01+ transceiver made by Nordic Semiconductor, seen in Fig. 1, is popular for its low cost and power usage.

These RF modules do not implement a full protocol stack and can to a great extent be programmed by the user. This is in comparison to more complex and expensive radios, such as the XBee family of radio modules (Digi International, USA).

Fig. 1. An RF communications module identical to those used in this case report, based on the nRF24L01+ transceiver. Manufactured by Seeed Studio.

This implies that, while cheap and flexible, these simpler radios are not necessarily straightforward to use. A typical user might implement existing open-source code libraries to control them, such as the nRF24 and nRF24Network libraries [10,11]. This in turn requires the user to familiarize themselves with relevant documentation and APIs.

2. Case background

The 7.5 ECTS course TMM4245 "Fuzzy Front End" taught at TrollLABS teaches graduate level engineering students methods and techniques for engineering design in the pre-requirement phase of new product development. The course is structured around project work with open-ended engineering design or product development problems from industry partners or research. Students are encouraged to develop a concept solution via rapid iterations of product prototypes [12]. A weekly stand-up meeting forces teams to communicate their current project status and to solicit input from other teams, similar to a sprint meeting in the scrum framework. This promotes skill- and knowledge sharing [13].

Students taking the course are encouraged to look for underlying causes, bigger-picture problems, and to pivot their project direction as necessary.

The students have varied backgrounds, and consequently often have limited preexisting mechatronics experience and start manipulating microcontrollers at a novice level.

3. Development

One project undertaken as part of this course was "TrollBOT", with which the authors had direct involvement. The initial goal of the project as stated was to "develop a robust, modular platform for robotics prototyping at TrollLABS". This goal was intentionally loose and vaguely stated.

Thus, the intended user group of the developed solution was assumed to be the users of TrollLABS. After experimenting with existing, established robotics frameworks such as Robot Operating System [14], project members concluded that as the typical users of TrollLABS often desired to build rapid, low-resolution prototypes for proof-of-concept testing, the immediate need was at a lower level of complexity – especially simple, quick-to-employ tools for rapidly building new prototype iterations of their various concepts.

The focus of the project consequently changed to developing tools for solving the group's own encountered challenges in building simple mechatronic concepts.

Within the problem statement of a *robust and modular platform*, the identified challenges were how to connect arbitrary physical components or modules to a central platform, potentially with radically different form factors, and how to implement control code for such de-centralized modules. Fig. 2 illustrates one such incarnation.

The project at this stage was using Arduino-based modules to test, on a basic level, various functionalities potentially interesting to a mechatronic robot system, such as sensors, motor control, power management and human input/output. To keep with the idea of a modular platform, these functionalities took the form of interacting cube modules, communicating

wirelessly via RF and interfacing structurally and electrically via magnetic connectors.

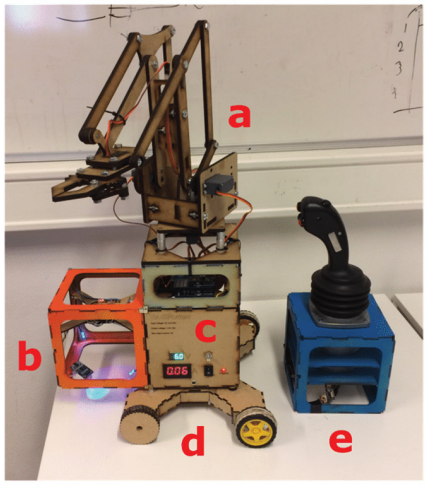

Fig. 2. An iteration of the modular cube-bot concept. Each cube contains a "slave" Arduino board, and communicates wirelessly with the "master" Arduino. The cubes receive power from the power supply via magnetic connectors. (a) 3-DOF gripper arm; (b) sensors unit; (c) power supply; (d) propulsion; (e) remote control housing the master Arduino.

4. Outcomes

While power was provided via the magnet connections, the Arduino controllers were set up to communicate wirelessly in a networked manner. To do this, the Arduinos were connected to RF-modules based on the Nordic Semiconductor nRF24L01+ transceiver (Fig. 1.). The radios communicated via an open-source protocol implemented via two pre-existing Arduino libraries: RF24 [10], providing fundamental radio control comparable to the link layer in the TCP/IP protocol [15], and RF24Network [11], providing functionality equivalent to the TCP/IP network layer [15]. Learning how the radios worked and understanding the libraries through their documentation required an investment of time that was significant within the scope of a one-semester course.

Concurrently, there was clear interest from other project teams in the same course to implement similar wireless functionalities. In the interest of facilitating ease of use both for themselves and for outside users who had not yet developed the necessary skill but wanted to integrate wireless functionalities into their own projects, an Arduino library was written.

The motivation guiding the formulation of this library was to aim it at the lowest common skill denominator, so that the library could serve as a tool enabling a user with only rudimentary skills and experience with Arduino to implement their own wireless functionality very quickly.

4.1. The TrollBOT library

The library enables the user to address and program several Arduino microcontrollers in a wireless network from one central, "master" Arduino. The "slave" nodes only run a communication loop, and execute commands sent from the master, as shown in Fig. 3. The API is constructed in such a way that the user addresses each node as an instance of the TrollBOT object and can write any other Arduino command as though they were coding on the Arduino node in question. A simple example may be seen in Fig. 4. This results in a coding process requiring the use of minimal new language syntax or direct manipulation of the wireless protocol library, in addition to keeping the code simple and easy to understand. In other words, abstraction has been applied with a user-centered focus to tailor the programming and prototyping experience for the user.

This allows even a very novice user to follow a simple wiring diagram, decide on a channel, and establish a wireless network. The network establishes a tree-type topology, with five possible layers of five nodes each.

To compare the use of the TrollBOT library with conventional programming methods and RF alternatives, an example scenario was created where sensor data is read from a potentiometer using an Arduino and sent to another Arduino for processing the data and fading an LED. The number of logical source lines of code (SLOC) needed to accomplish the scenario was then compared. SLOC is a widely-used code metric in software development, and while simplistic, it is generally accepted to be correlated with code complexity and development effort [16,17].

```
// Include the TrollBot library
#include"TrollBot.h"

// Initiate this node with
// address 01 on channel 100
TrollBot Alf(01, 100);

//Run the setup for this node
void setup() {
  Alf.setup();
}

// Run the main loop for this node
void loop() {
  Loop();
}
```

Fig. 3. Code example from a "slave" node. The only information the user must edit from the default code is the node address and RF channel.


```
// Include the TrollBot library
#include"TrollBot.h"

// Initiate the node objects
// with addresses 00-02 on channel 100
TrollBot Master(00, 100);
TrollBot Alf(01, 100);
TrollBot Bob(02, 100);

void setup() {
  // Run the setup functions for the master node
  Master.setup();
  // Set the pin 6 as output on Alf node
  Alf.pinMode(6, OUTPUT);
}

void loop() {
  // Refresh master loop once per cycle
  Master.masterLoop();
  // Read and store potentiometer value from Bob
  int pot = Bob.analogRead(A0);
  // Map the read value from 0-1023 to 0-255
  int light = map(pot, 0, 1023, 0, 255);
  // Write the value onto the LED on Alf
  Alf.analogWrite(6, light);
}
```

Fig. 4. Code example from a "master" node networked with two "slave" nodes. The user can read from and write to the slave nodes directly from the master code.

RF alternatives included in our comparison consists of the ZigBee protocol, Bluetooth and Wi-Fi. The same RF module used in the development project without using the TrollBOT library was also included. To the authors' knowledge, having consulted with the relevant online programming communities, minimum amounts of code to reproduce similar functionalities with the alternative methods were found. The codes used for the comparison can be found in Appendix A. The results are presented in the next section.

5. Results and discussion

5.1. TrollBot efficiency evaluation

As shown in Table 1, using TrollBOT has a clear advantage in terms of the required number of lines needed to program the simple example scenario. The Bluetooth example required an initial setup program to pair the two devices which increased the program size considerably. This is comparable to the less complicated setup code needed for the slave nodes of TrollBOT shown in Fig. 3. Overall, the TrollBOT code requires less than half of the number of lines used by the other methods.

After the initial setup, another advantage of TrollBOT compared to the rest is the fact that changes to the code can be done on only one of the Arduinos, since the Master contains all the code controlling the other nodes. This feature is unique to the TrollBOT library in this comparison. TrollBOT can thus facilitate users that are familiar with programming a single Arduino to expand their prototyping capabilities by increasing the number of units (more pins for reading sensors or controlling actuators), in addition to allowing different physical locations of the units while programming only one Arduino.

Unit costs have been overlooked due to wide variability of price levels from different suppliers for the same products, though it is noted that prices are broadly comparable.

Table 1. Comparison of alternatives for wireless communication on Arduino.

RF alternative	Protocol	Nominal data rate [Mbps]	Example scenario SLOC
XBee [18]	ZigBee	0.25	38
Bluetooth (Itead HC-05) [19]	Bluetooth 2.0 + EDR	2	70
Wi-Fi (ESP8266) [20]	Wi-Fi 802.11n	72.2	41
nRF24 [21]	Proprietary (Nordic ESB)	2	33
nRF24 with TrollBOT	Proprietary (Nordic ESB)	2	16

5.2. Observations

After the library was made available to other lab users, it disseminated to other project groups as an example of in-lab skill sharing. This allowed the other groups to make their own "skill-jumps" as they had an easy to use starting point for their own applications.

A project running simultaneously in the same course developing an aquatic robot using snake-like propulsion was able to very quickly implement wireless control of their vehicle, which had previously been a stumbling block, thus freeing up development time for other critical issues [12].

In the semester following the project's development, the course "TMM4150 – Machine Design and Mechatronics", another project-based graduate course taught in the same department, provided the library to course participants as a simple way of implementing remote control of a small vehicle.

Separately, a student working on a master's project developing remotely controlled eyes for medical simulation manikins became aware of the project, and quickly implemented it for sending motor control input from a control rig to the eye module [22].

In common, it was observed among these distinct applications that using this simple tool to rapidly implement simple forms of wireless communication allowed for the users to spend their project time on more distinctive and novel parts of their projects. While RF communication was an important functionality, it was not in any case the focus of the projects. But the resources freed up enabled the designers to further refine other parts of their prototypes, resulting in a higher technical level in their final project outcomes.

5.3. Limitations

An argument can be made that opportunities for learning may be missed by adding another layer of abstraction between the user and the code controlling the radio. While it is true that experience interacting more directly with radio circuitry is bypassed, the intent of this library – and of many other tools – is to facilitate some other process or outcome.

Perhaps ironically, this library does remove some of the flexibility inherent to non-protocol radios in the interest of

ease-of-use. Thus, for applications requiring specialized or advanced communications capabilities this library may not be the most performant. While no rigorous comparison of networking metrics such as throughput and power consumption were carried out, literature suggests that the RF24 library which TrollBOT builds on outperforms other low-power RF alternatives such as the XBee in terms of data throughput, but exhibits poor power efficiency [15]. This was not considered to be a significant hindrance in the setting of low-resolution prototyping but should be considered by designers moving beyond the pre-requirement design stage.

6. Conclusions and outlook

A software library, named TrollBOT, for controlling nRF24L01+ RF transceivers via Arduino has been presented.

The library enables the user to program several Arduino nodes on a wireless network via a master and slave configuration, allowing the user to program all logical code for their application on only one Arduino. In effect this can drastically reduce the amount of code the user needs to write. Additionally, the library introduces minimal new language syntax, allowing users even at a novice level to implement wireless node-to-node communication between two or more Arduinos.

By providing a way to set up wireless communication at a minimum of required effort, TrollBOT facilitates the rapid prototyping and testing of design concepts early in the design process. This in turn allows design requirements to be defined through iterative prototyping.

Access to this tool allowed other project teams in a graduate engineering design course to quickly implement useful features to their own design concepts, freeing up development time and resulting in higher prototype resolution by the end of their projects. The tool also proved valuable as a provided functionality in a graduate level mechatronics course. We are presenting this tool in the hope that others may find it as useful as we have.

We acknowledge that the results presented are particular to a specific, constructed case as observed by the authors. In future research we would like to generate a more general quantitative comparison of the effectiveness of this library, for example by presenting two groups of designers with a specific engineering design problem and allowing one group to use the TrollBOT library and the other to choose and create their own tools. The resulting time to reach defining design milestones as well as comparative measures of prototype resolution might then be compared.

Appendix A. GitHub depository

The full source code and documentation of the TrollBOT library is provided for free use. It may be accessed via the following DOI: 10.5281/zenodo.3518333 [23].

References

[1] Eppinger S, Ulrich K. Product Design and Development. 5th Edition. New York: McGraw/Hill; 2012.

[2] Houde S, Hill C. What do prototypes prototype? Handb. Hum.-Comput. Interact. Second edition, Cupertino, California: Elsevier Science B.V.; 1997.

[3] Kriesi C, Blindheim J, Bjelland Ø, Steinert M. Creating Dynamic Requirements through Iteratively Prototyping Critical Functionalities. Procedia CIRP 2016;50:790–5. https://doi.org/10.1016/j.procir.2016.04.122.

[4] Schrage M. The Culture(s) of PROTOTYPING. Des Manag J Former Ser 1993;4:55–65. https://doi.org/10.1111/j.1948-7169.1993.tb00128.x.

[5] Auflem M, Erichsen JF, Steinert M. Exemplifying Prototype-Driven Development through Concepts for Medical Training Simulators. Procedia CIRP 2019;84:572–8. https://doi.org/10.1016/j.procir.2019.04.202.

[6] Jensen MB, Semb CCS, Vindal S, Steinert M. State of the Art of Makerspaces - Success Criteria When Designing Makerspaces for Norwegian Industrial Companies. Procedia CIRP 2016;54:65–70. https://doi.org/10.1016/j.procir.2016.05.069.

[7] Slåttsveen K, Kriesi C, Steinert M, Aasland KE. Experiences from a positivistic way of teaching in the Fuzzy Front End. 93 Proc. 20th Int. Conf. Eng. Prod. Des. Educ. EPDE 2018 Dyson Sch. Eng. Imp. Coll. Lond. 6th - 7th Sept. 2018, 2018.

[8] Hertzog PE, Swart AJ. Arduino — Enabling engineering students to obtain academic success in a design-based module. 2016 IEEE Glob. Eng. Educ. Conf. EDUCON, 2016, p. 66–73. https://doi.org/10.1109/EDUCON.2016.7474533.

[9] Jamieson P, Herdtner J. More missing the Boat — Arduino, Raspberry Pi, and small prototyping boards and engineering education needs them. 2015 IEEE Front. Educ. Conf. FIE, 2015, p. 1–6. https://doi.org/10.1109/FIE.2015.7344259.

[10] TMRh20. Optimized fork of nRF24L01 for Arduino & Raspberry Pi/Linux Devices. https://github.com/nRF24/RF24; 2019.

[11] TMRh20. Optimized Network Layer for nRF24L01(+) Radios on Arduino and Raspberry Pi. https://github.com/nRF24/RF24Network; 2019.

[12] Vestad H, Kriesi C, Slåttsveen K, Steinert M. Observations on the Effects of Skill Transfer through Experience Sharing and In-Person Communication. Proc Des Soc Int Conf Eng Des 2019;1:199–208. https://doi.org/10.1017/dsi.2019.23.

[13] Chau T, Maurer F, Melnik G. Knowledge sharing: agile methods vs. Tayloristic methods. WET ICE 2003 Proc. Twelfth IEEE Int. Workshop Enabling Technol. Infrastruct. Collab. Enterp. 2003, 2003, p. 302–7. https://doi.org/10.1109/ENABL.2003.1231427.

[14] Open Source Robotics Foundation. ROS.org. ROS n.d. https://www.ros.org/ (accessed October 20, 2019).

[15] Saha H, Mandal S, Mitra S, Banerjee S, Saha U. Comparative performance analysis between nRF24L01+ and XBEE ZB module based wireless ad-hoc networks. Int J Comput Netw Inf Secur 2017;9:36. https://doi.org/10.5815/ijcnis.2017.07.05.

[16] Albrecht AJ, Gaffney JE. Software Function, Source Lines of Code, and Development Effort Prediction: A Software Science Validation. IEEE Trans Softw Eng 1983;SE-9:639–48. https://doi.org/10.1109/TSE.1983.235271.

[17] Bhatia S, Malhotra J. A survey on impact of lines of code on software complexity. 2014 Int. Conf. Adv. Eng. Technol. Res. ICAETR - 2014, 2014, p. 1–4. https://doi.org/10.1109/ICAETR.2014.7012875.

[18] Digi XBee and XBee-PRO Zigbee RF Modules | Digi International n.d. https://www.digi.com/products/embedded-systems/digi-xbee/rf-modules/2-4-ghz-modules/xbee-zigbee#specifications (accessed March 2, 2020).

[19] ITEAD INTELLIGENT SYSTEMS CO. LTD. HC-05 Bluetooth to Serial Port Module 2010.

[20] Espressif Systems. ESP8266EX Datasheet. Version 6.3 2019.

[21] Nordic Semiconductor. nRF24L01+ Single Chip 2.4GHz Transceiver Preliminary Product Specification v1.0 2008.

[22] Nygaard T, Kriesi C, Sjöman H, Steinert M. From the Eyes of the Patient: Real Time Gaze Control of Medical Training Mannequins. Proc. 10th Nord. Conf. Hum.-Comput. Interact., New York, NY, USA: ACM; 2018, p. 932–935. https://doi.org/10.1145/3240167.3240228.

[23] Sampsa Kohtala, Torjus Steffensen, Håvard Vestad. TrollBot. Zenodo; 2019. https://doi.org/10.5281/zenodo.3518333.

C7. Playing the pipes: Acoustic sensing and machine learning for performance feedback during endotracheal intubation simulation

Frontiers in Robotics and AI. Under review.

Torjus Lines Steffensen, Brage Bartnes, Maja Lucia Fuglstad, Marius Auflem and Martin Steinert

frontiers

Playing the Pipes: Acoustic Sensing and Machine Learning for Performance Feedback During Endotracheal Intubation Simulation

Torjus L. Steffensen[1*], Barge Bartnes[2], Maja L. Fuglstad[2], Marius Auflem[2], and Martin Steinert[2]

[1]Department of Circulation and Medical Imaging, Norwegian University of Science and Technology, Trondheim, Norway

[2] Department of Mechanical Engineering, Norwegian University of Science and Technology, Trondheim, Norway

*** Correspondence:**
Torjus L. Steffensen
torjus.l.steffensen@ntnu.no

Keywords: medical simulation training, endotracheal intubation, acoustic sensing, machine learning in healthcare, convolutional neural network (CNN), support vector machine (SVM), audio classification, transfer learning

Abstract

Objective: In emergency medicine, airway management is a core skill that includes endotracheal intubation (ETI), a common technique that can result in ineffective ventilation and laryngotracheal injury if executed incorrectly. We present a method for automatically generating performance feedback during ETI simulator training, potentially augmenting training outcomes on robotic simulators.

Method: Electret microphones recorded ultrasonic echoes pulsed through the complex geometry of a simulated airway during ETI performed on a full-size patient simulator. As the endotracheal tube is inserted deeper and the cuff is inflated, the resulting changes in geometry are reflected in the recorded signal. We trained machine learning models to classify 240 intubations distributed equally between six conditions: three insertion depths and two cuff inflation states. The best performing models were cross validated in a leave-one-subject-out scheme.

Results: Best performance was achieved by transfer learning with a convolutional neural network pre-trained for sound classification, reaching global accuracy above 98% on 1-second-long audio test samples. A support vector machine trained on different features achieved a median accuracy of 85% on the full label set and 97% on a reduced label set of tube depth only.

Significance: This proof-of-concept study demonstrates a method of measuring qualitative performance criteria during simulated ETI in a relatively simple way that does not damage ecological validity of the simulated anatomy. As traditional sonar is hampered by geometrical complexity compounded by the introduced equipment in ETI, the accuracy of machine learning methods in this confined design space enables application in other invasive procedures. By enabling better interaction between the human user and the robotic simulator, this approach could improve training experiences and outcomes in medical simulation for ETI as well as many other invasive clinical procedures.

1 Introduction

Airway management is critically important in emergency medicine and critical care (Trueger, 2013). Endotracheal intubation (ETI) is a widely used technique in intensive care units (Narendra et al., 2016) for unconscious or semi-conscious patients who cannot maintain breathing independently (Trueger, 2013; Kovacs and Sowers, 2018). This invasive non-surgical procedure involves the insertion of an endotracheal tube to establish an artificial airway, securing the airway and preventing aspiration while allowing healthcare practitioners to control patient ventilation.

However, ETI carries risks, such as laryngotracheal injury (Tikka and Hilmi, 2019), and hypoxia or even brain damage and death if a free airway is not established in critical care settings. Consequently, adequate training in laryngoscopy and ETI is crucial for safe and accurate procedural execution. Patient simulators play an important role in this training, complementing procedural competence and failure mode awareness before practicing on real patients.

In simulation-based training for clinical skills and procedural routines, such as ETI, the equipment should demand similar cognitive and psychomotor loading as performing the routines would on real patients (McGaghie et al., 2006). This is considered by the ecological validity of simulation, meaning that the simulated procedure should facilitate repeated practice of relevant tasks by using sufficient equipment for trainees to realistically perform them (Kushniruk et al., 2013). The design of simulators should, therefore, provide lifelike experiences for both skilled and novice medical practitioners in training, which is essential to mitigate sources of false learning and achieve familiarity effects for skills and experiences to transfer into clinical practice. Replicating relevant anatomy accurately is often complex, yet critical for practitioners to develop the skills and knowledge required to perform procedures such as ETI safely.

Providing actionable and descriptive feedback during and after training events is paramount (Issenberg et al., 2005; McGaghie et al., 2006). Quality performance metrics and feedback should integrate within and enhance simulated training models, crucially without compromising simulator realism. This would require sensors or other foreign elements to not cause visual or tactile disturbances, limiting training validity. Replicating the tactile sensation of ETI while providing performance feedback is a significant challenge in ETI simulation; a design objective with anatomical constraints, tactile compliance requirements, and obstructed visibility of the procedure.

This paper presents a proof of concept of a method that combines acoustic measurement and artificial intelligence (AI) to classify ETI user performance on patient simulators in terms of endotracheal intubation depth and cuff inflation status. This method transmits inaudible ultrasonic pulses into the simulated manikin airway and records the sound in a location away from the trachea. As the airway geometry is highly complex, traditional sonar methods are difficult to implement without sacrificing anatomical accuracy. Instead, machine learning classifiers are trained on the reflected audio's spectral content to detect subtle changes in reflected sound resulting from altered airway geometry acoustics. The method is non-intrusive and avoids tracheal instrumentation that could interfere with procedure realism.

To demonstrate the feasibility of this proof of concept, expert users performed 240 intubations on a patient simulator to generate a dataset for training and validating our model. To investigate the effect of equipment location, two configurations were used for both the sound source and microphone. Two classification approaches were employed: support vector machine (SVM) and convolutional neural network (CNN) with transfer learning. By using two different approaches, we aimed to enhance the

robustness of our findings and prompt deeper understanding of the integration problem as well as underlying patterns in the data. SVM provides a solid baseline for audio classification performance (Cortes and Vapnik, 1995; Laput et al., 2015), while CNN transfer learning, leveraging pre-trained models, captures more complex relationships within the data, leading to potentially better performance (Pan and Yang, 2010; LeCun et al., 2015). The best-performing model was tested using a leave-one-intubation-out cross-validation scheme, achieving a median best performance of 98% global accuracy on 1-second audio recordings.

This approach provides a valuable tool for classifying endotracheal intubation training performance on patient simulators. The system is flexible and easily integrated, with potential applications beyond intubation training. By demonstrating the success of this initial proof of concept, we hope to enable integration in medical simulation, where providing quality performance metrics and feedback can support better training experiences and outcome.

2 Materials and methods

2.1 Intubation procedure

Intubation is a crucial procedure in airway management, involving the administration of anesthesia and muscle relaxants to the patient, followed by preoxygenation with 100% oxygen via a mask and bag (Butterworth et al., 2013; Wiengand, 2016). The endotracheal tube is then inserted using a laryngoscope to expose the vocal cords, with the tube's depth indicated by markings on the tube (Haas et al., 2014). Once the tube is in place, the cuff is inflated sufficiently to ensure a proper seal and prevent movement during the procedure (Artime and Hagberg, 2020; Hagberg, 2022). The endotracheal tube's cuff serves two main purposes: preventing gastric content and other substances from entering the airways and avoiding airflow leakages around the tube (Nejla et al., 2017).

Incorrect cuff inflation can lead to complications. Underinflation may result in microaspiration (Stewart et al., 2003; Gunasekera and Gratrix, 2016; Nejla et al., 2017) or laryngeal and tracheal complications due to tube movement (Jougon et al., 2000). Overinflation can cause tracheal mucosal damage (Tu et al., 1999; Gunasekera and Gratrix, 2016), ischemia, ulceration, inflammation, tracheal rupture, granulation, and tracheal stenosis (Ganner, 2001; Fan et al., 2004; Butterworth et al., 2013).

Proper endotracheal tube placement minimizes risk of airway injury (Mort et al., 2013). Shallow placement can damage the upper airway structures, including vocal cord paralysis, ulceration, or dysfunction (Lu et al., 1999; Butterworth et al., 2013; Mort et al., 2013). Deep placement can impact the carina, leading to hypertension, tachycardia, and bronchospasm (Varshney et al., 2011). Moreover, endobronchial intubation, or unintended placement of the tube in the left or (more commonly) right main bronchi, can result in one-lung ventilation (De Marchi, 2014; Lohser and Slinger, 2015; Heyne et al., 2022), causing injury to both lungs. The ventilated lung can suffer from tension pneumothorax (Salem and Baraka, 2013) and reduced residual air (Lohser and Slinger, 2015), while the unventilated lung may experience atelectasis, hypoxemia, and hypercapnia (Lohser and Slinger, 2015).

2.2 Data acquisition

2.2.1 Acoustic equipment

A full-size patient simulator (SimMan, Laerdal Medical, Norway) was outfitted with two small electret condenser microphones (EM272, Primo, Japan) and a small piezoelectric buzzer

(MCUST10P40B07RO, Farnell, USA). The microphones are small enough to be built into space-constrained environments and are sensitive to ultrasonic frequencies. The usable frequency range extends to approximately 60 kHz, but with strong attenuation above approximately 40 kHz. The two mono microphones were connected in stereo to an audio A/D interface (Xonar U5, ASUS, Taiwan) and recorded at a sample rate of 192 kHz to a MacBook as separate audio channels using open-source software (Audacity 3.2.5, Audacity Team).

The piezo buzzer has a peak sound pressure at 40 kHz, but also a reasonable output from about 10 kHz to 60 kHz. During the experiment, the buzzer was driven using an arbitrary waveform generator (UTG2025A, Uni-Trend, China). A few different waveforms were tried, but in the end we followed the suggestion of earlier work (Laput et al., 2015) and used a repeating sinusoidal linear sweep from 20 kHz to 60 kHz with a sweep duration of 100 ms. The resulting output was inaudible and seemed to provide good classification performance in our setting.

One microphone was fixed in the manikin's head, above the airway, while the other was fixed in a tube below the airway (Figure 1). Two series of recordings were made. In the first series, the piezo buzzer was placed in the chest cavity of the manikin, outside the airway assembly, while in the second series, the buzzer was fixed directly in the airway tube across from the second microphone.

2.2.2 Recording protocol

Intubations were recorded in six distinct categories derived from the combination of tube placement depth (correct, deep, and shallow) and cuff inflation status (inflated/deflated).

Prior to recording, an expert user performed the intubation procedure using a laryngoscope and standard ET tube. Following manikin manufacturer recommendations, a purpose-made silicone lubricant was applied before intubating. With the endotracheal tube in place, 25 seconds of audio were recorded while the buzzer was active. The tube's cuff was then inflated, and another 25 seconds of audio were recorded.

In both series, 40 intubations were made in each of the three positions (shallow, correct, deep), resulting in 120 intubations per buzzer configuration and 240 intubations in total. With and without inflation, the total recorded data set consists of 480 recordings, divided equally among the six classes. A total of 12,000 seconds of audio were recorded (Table 1).

2.3 SVM model

2.3.1 Preprocessing and feature extraction

SVMs are robust models for complex ultrasound sound characterization (Temko and Nadeu, 2006; Laput et al., 2015) . To train the SVM classifier, recordings from configuration B1, M2 (Figure 2) were first split into testing (20%) and training cohorts. Audio was highpass filtered using a Butterworth filter with a 20 kHz passband, emphasizing the inaudible portion of the spectrum, and normalized before being split into 0.5-second-long segments resulting in a total of 9600 training and 2400 test segments. For each segment, we extracted a set of features consisting of the zero-crossing rate, 2-norm, root-mean-square values, spectral centroids as well as the magnitude of the discrete FFT. The dimensionality of the resulting feature vector was reduced via principal component analysis. The first 1000 components were kept, containing more than 99.9% of the explained data variance.

Features including mel-frequency cepstral coefficients and wavelet scattering coefficients resulted in worse performance (Supplementary Figure 1).

2.3.2 Model training

A linear kernel SVM classifier with one vs. rest decision function was trained on the training data with two sets of labels using libsvm (Chang and Lin, 2011; Pedregosa et al., 2011). In the first label set, audio segments were only labeled according to depth of tube insertion, making three classes. In the second set, segments were additionally labelled with cuff inflation status, making six classes.

2.4 Transfer learning

In addition to the SVM classifier we employed a transfer learning approach using a pre-trained deep learning model, YAMNet (Hershey et al., 2017). YAMNet is a convolutional neural network (CNN) trained on a large dataset of audio signals, designed for environmental sound classification. YAMNet has been demonstrated to be effective in transfer learning applications (Tsalera et al., 2021).

2.4.1 Preprocessing

We processed the audio data similarly to the SVM model. Audio was highpass filtered with a 20 kHz passband, normalized, and split into 1-second chunks. A sliding-window approach could yield more spectrograms, but we opted not to do so in order to simplify input size analysis, additionally assuming the audio signal to be relatively stationary in our controlled environment.

The signal was resampled to 16 kHz using the MATLAB Signal Processing Toolbox. The short-time Fourier transform (STFT) was computed for each downsampled signal using a Hann window with period 128, FFT length of 512 and 75% overlap. The STFT was filtered with a 64-band mel-scale filter bank and the resulting spectrograms divided into 10ms bins, yielding 96x64 sized spectrograms suitable for input to the network (Figure 3).

2.4.2 Model training

The last fully connected layer and the output layer of the network were replaced to reflect our classification labels. Using the training spectrograms, the network was trained on a single GPU (GTX 2080 TI, Nvidia, USA) using the adam optimizer with mini batches of size 128 for 5 epochs and an initial learning rate of 0.001 halving every two epochs. The loss function was cross-entropy.

2.4.3 CNN Cross-validation

We implemented a leave-one-intubation-out cross-validation approach. One intubation (both deflated and inflated cuff) was excluded from the training process at a time. For each intubation, we trained the model on the remaining 239 intubations, and tested the classifier on the held-out intubation.

To compare the influence of microphone and buzzer location, we repeated the training and testing process for each of the four microphone and buzzer combinations: microphone over / under airway (M1, M2), and buzzer inside / outside the airway (B1, B2) (Figure 1).

To evaluate the classifier's performance using different audio input sizes, we selected 1000 random permutations of the 25 labelled 0.96-second spectrograms within each test intubation set. These permutations were incremented by 1 second, from 1 to 25 seconds. The output class was determined by the mode of the subset of test labels (Figure 4).

3 Results

3.1 SVM model

For 100 random test-train splits the median global accuracy was 0.85 (0.70 – 0.93) on all 6 labels and 0.97 (0.91 – 0.99) for the reduced depth-only set of 3 labels. Confusion matrices for one test-train split are shown in Figure 2. While the model has good sensitivity to intubation depth, it seems to have difficulty distinguishing cuff status. Sensitivity to cuff status during shallow intubations is particularly poor.

3.2 CNN model

The transfer learning approach using the pretrained YAMNet network significantly enhanced performance on the audio classification task compared to the SVM classifier. Cross-validation results demonstrated high classification metrics across all categories, with macro averages for precision, sensitivity, specificity, accuracy, and F-measure at 0.980. Performance metrics of the CNN model for the best audio configuration (B1, M2) are presented in Table 2. The classifier achieved a best global accuracy of 97.57% across the entire feature set of spectrograms (Figure 4). Per intubation, the trained classifier achieved a best global accuracy of 98.75% when exposed to the full set of 25 seconds of audio for each intubation case during the classification step. Best case accuracy reached 100% but went back down as classification set size approached the full classification set, reflecting the unbalanced distribution of incorrect predictions. Classification performance improved when pooling longer inputs (Figure 4). For the best-performing configuration, mean accuracy did not increase significantly with input sizes above 5 seconds of audio, although the worst-case classification accuracy did continue to improve until about 15 seconds.

3.3 Equipment configuration

Microphone and buzzer location significantly affected the classifier's performance. Microphone location 2 (inside the closed airway tubing) resulted in a consistently better classification accuracy. Microphone location 1 (mouth assembly) had significantly worse classification accuracy when the buzzer was not placed inside the airway assembly, but only had slightly decreased performance with the buzzer in the airway.

4 Discussion

4.1 Equipment configuration and model performance

Our results demonstrated that the transfer learning approach using the pretrained YAMNet network outperformed the SVM classifier, with high classification metrics across all categories. Our findings indicate that the transfer learning strategy is effective in accurately classifying audio signals for this application, while the good SVM performance on the depth-only label set argues against the performance of the CNN model being due to overtraining or model-specific behaviour.

The equipment configuration (microphone and buzzer location) influenced classification performance. The best performance was achieved with microphone location 1 (inside closed airway tubing) and lower airway audio configuration. This may be explained by the increased proximity of the buzzer to the microphone in this configuration. Sound recorded from the bronchial pathway could differentiate between changing windpipe geometries, even with the buzzer outside the windpipe assembly, while the microphone above the airway performed significantly worse when the buzzer was further away.

The pretrained CNN's ability to discern sound events resampled from a much higher frequency range is noteworthy, as being able to leverage the classification performance of models trained on very large datasets of audible sound – YAMNet is trained on the Audioset-YouTube corpus(Gemmeke et al., 2017) – to classify audio that is intentionally inaudible is quite powerful.

4.2 Comparison of SVM and CNN models

Our study showed that the pretrained CNN model significantly outperformed the SVM model. This could potentially be explained by a CNN's particular aptitude to learn complex patterns in high-dimensional data like audio signals (LeCun et al., 2015). The differences in performance between the two models could also be partially attributed to the relative complexity of the feature extraction process and interpretation. Future work on this approach could investigate the impact of using alternative or combined feature extraction techniques on SVM model performance.

4.3 Network activation

Given the significant compression to a low sampling rate, it is prudent to examine the features of the compressed signal on which the CNN operates. Figure 4 presents averaged spectrograms for each condition with LIME and occlusion sensitivity maps. LIME (locally interpretable model-agnostic explanations) and occlusion sensitivity are decision explanation tools that assign a relative importance to regions of the input data (Kakogeorgiou and Karantzalos, 2021). These maps help estimate the input data's relative importance for classification decisions. Notably, even with very aggressive compression and aliasing, the higher frequency range remained significant, particularly for the "correct" condition. However, classification performance for shallow intubation was consistently lower, possibly due to the lack of distinct discriminatory feature regions in this condition.

4.4 Advantages of acoustic sensing in medical simulators

The remote nature of acoustic sensing offers flexibility for designers, allowing them to instrument simulators without altering the relevant anatomy or compromising the fidelity or validity of the simulation. As a "black box" solution, our approach requires minimal implementation effort, and to our knowledge no comparable AI-based acoustic classification methods have been reported to similar ends in medical simulators. Although our proof of concept focused on intubation training, ease of integration implies it could be extended to other procedures where the introduction of instruments into the patient's body is involved, such as larynx mask insertion, phlegm suction, and intravascular procedures.

4.5 Implications for designers and training outcomes

Our acoustic sensing approach offers designers flexibility and ease of integration, enabling them to incorporate advanced sensing into existing product architectures without altering simulated anatomical structures. While we cannot draw definitive conclusions about the impact on medical training outcomes, improving the quality of simulator feedback could potentially enhance them. By providing insights into otherwise invisible processes, our approach can improve feedback and assessment, supporting better training experiences and outcomes in medical simulation.

4.6 Model design

The proposed feedback model can only provide feedback on discrete states, not a continuous measurement of insertion depth. Discrete state classification was chosen due to practical relevance,

reduced complexity, and increased robustness. Discrete classification aligns with intubation training goals, as it focuses on distinguishing correct from incorrect tube placement. This approach simplifies the task of the feedback system, avoiding challenges associated with the complex airway geometry. Moreover, discrete classification is likely to be more robust and less sensitive to measurement noise. It may more easily be generalizable across different training scenarios where this approach may be relevant.

4.7 Study limitations and future work

The study was conducted in a controlled setting, which may not accurately represent the variability and challenges encountered in real-world medical training environments. Factors such as background noise, differences in equipment, and variations in patient simulators might impact the performance of our acoustic sensing method. Secondly, the evaluation of preprocessing methods and SVM features was not exhaustive. Although our approach demonstrated promising results using the YAMNet network and transfer learning, other preprocessing steps and classification algorithms might yield better performance on more explainable models and might be more robust outside a controlled lab setup.

Additionally, our study did not account for potential confounders such as microphone and buzzer calibration. The performance of the acoustic sensing method could be influenced by inconsistencies in the hardware or differences in the acoustics of the training environment. Future research could evaluate the robustness and generalizability of this acoustic sensing approach using different equipment and less controlled environments.

5 Conclusion

Acoustic sensing in combination with machine learning can capture geometric changes in complex anatomical structures with high accuracy. This enables collecting valuable feedback on otherwise hidden processes during skill and procedural training on simulated anatomy. This study highlights the value of the acoustic sensing approach in providing a simple and effective solution for classifying ETI user performance. Remarkably, the method achieved good results even without serious attempts at equipment calibration or an exhaustive evaluation of features or algorithms. This robustness lowers implementation cost and adaptability for use in various clinical training contexts. Reasonable classification performance on a secondary machine learning model trained on different feature types on the same data set is encouraging, indicating that the high performance of the CNN model is not the result of overfitting.

Our results highlight the effect of microphone and buzzer positioning on classifier performance, and the significance of optimal placement to achieve accurate results. We further illustrate the positive correlation between increased test input size and classifier accuracy, indicating the potential benefits of utilizing longer audio segments for improved classification reliability.

By refining and building upon this initial work, similar acoustic sensing methods could become a valuable tool for enhancing the quality of feedback and performance metrics in medical simulation, contributing to better training experiences and outcomes in critical airway management procedures. Further investigation may focus on refining the models and examining the potential integration of this approach into real-time monitoring systems for intubation training procedures.

6 Conflict of Interest

The authors declare that the research was conducted in the absence of any commercial or financial relationships that could be construed as a potential conflict of interest.

7 Author Contributions

MA and TS conceptualized and designed the study. BB and MF conducted experimental work and organized the database. TS prepared the initial draft of the manuscript. TS, MF, BB, and MA wrote sections of the manuscript. All authors contributed to manuscript revision, read, and approved the submitted version.

8 Funding

This research was supported by the Research Council of Norway through project number 290404.

9 References

Artime, A., and Hagberg, C. A. (2020). Airway management in the adult. *Miller's Anesthesia. 9th ed. Philadelphia: Elsevier*, 1373–1412.

Butterworth, J. F., Mackey, D. C., and Wasnick, J. D. (2013). *Morgan & Mikhail's Clinical Anesthesiology*. 5th ed. McGraw-Hill Education.

Chang, C.-C., and Lin, C.-J. (2011). LIBSVM: A library for support vector machines. *ACM Trans. Intell. Syst. Technol.* 2, 27:1-27:27. doi: 10.1145/1961189.1961199.

Cortes, C., and Vapnik, V. (1995). Support-Vector Networks. *Machine Learning* 20, 273–297. doi: 10.1023/A:1022627411411.

De Marchi, L. (2014). "Endobronchial Intubation," in *Anesthesiology Core Review: Part One Basic Exam*, eds. B. S. Freeman and J. S. Berger (New York, NY: McGraw-Hill Education). Available at: accessanesthesiology.mhmedical.com/content.aspx?aid=1102567869 [Accessed April 19, 2023].

Fan, C.-M., Ko, P. C.-I., Tsai, K.-C., Chiang, W.-C., Chang, Y.-C., Chen, W.-J., et al. (2004). Tracheal rupture complicating emergent endotracheal intubation. *The American Journal of Emergency Medicine* 22, 289–293. doi: 10.1016/j.ajem.2004.04.012.

Ganner, C. (2001). The accurate measurement of endotracheal tube cuff pressures. *British Journal of Nursing* 10, 1127. doi: 10.12968/bjon.2001.10.17.9952.

Gemmeke, J. F., Ellis, D. P. W., Freedman, D., Jansen, A., Lawrence, W., Moore, R. C., et al. (2017). Audio Set: An ontology and human-labeled dataset for audio events. in *2017 IEEE International Conference on Acoustics, Speech and Signal Processing (ICASSP)*, 776–780. doi: 10.1109/ICASSP.2017.7952261.

Gunasekera, P., and Gratrix, A. (2016). Ventilator-associated pneumonia. *BJA Education* 16, 198–202. doi: 10.1093/bjaed/mkv046.

Haas, C. F., Eakin, R. M., Konkle, M. A., and Blank, R. (2014). Endotracheal Tubes: Old and NewDiscussion. *Respiratory Care* 59, 933–955. doi: 10.4187/respcare.02868.

Hagberg, C. A. (2022). *Hagberg and Benumof's Airway Management*. Elsevier Health Sciences Available at: https://books.google.no/books?id=TiPuzgEACAAJ.

Hershey, S., Chaudhuri, S., Ellis, D. P. W., Gemmeke, J. F., Jansen, A., Moore, R. C., et al. (2017). CNN architectures for large-scale audio classification. in *2017 IEEE International Conference on Acoustics, Speech and Signal Processing (ICASSP)*, 131–135. doi: 10.1109/ICASSP.2017.7952132.

Heyne, G., Ewens, S., Kirsten, H., Fakler, J. K. M., Özkurtul, O., Hempel, G., et al. (2022). Risk factors and outcomes of unrecognised endobronchial intubation in major trauma patients. *Emerg Med J* 39, 534–539. doi: 10.1136/emermed-2021-211786.

Issenberg, S. B., Mcgaghie, W. C., Petrusa, E. R., Gordon, D. L., and Scalese, R. J. (2005). Features and uses of high-fidelity medical simulations that lead to effective learning: a BEME systematic review. *Medical Teacher* 27, 10–28. doi: 10.1080/01421590500046924.

Jougon, J., Ballester, M., Choukroun, E., Dubrez, J., Reboul, G., and Velly, J.-F. (2000). Conservative treatment for postintubation tracheobronchial rupture. *The Annals of Thoracic Surgery* 69, 216–220. doi: 10.1016/S0003-4975(99)01129-7.

Kakogeorgiou, I., and Karantzalos, K. (2021). Evaluating explainable artificial intelligence methods for multi-label deep learning classification tasks in remote sensing. *International Journal of Applied Earth Observation and Geoinformation* 103, 102520. doi: 10.1016/j.jag.2021.102520.

Kovacs, G., and Sowers, N. (2018). Airway Management in Trauma. *Emergency Medicine Clinics of North America* 36, 61–84. doi: 10.1016/j.emc.2017.08.006.

Kushniruk, A., Nohr, C., Jensen, S., and Borycki, E. M. (2013). From Usability Testing to Clinical Simulations: Bringing Context into the Design and Evaluation of Usable and Safe Health Information Technologies: Contribution of the IMIA Human Factors Engineering for Healthcare Informatics Working Group. *Yearbook of Medical Informatics* 22, 78–85. doi: 10.1055/s-0038-1638836.

Laput, G., Brockmeyer, E., Hudson, S. E., and Harrison, C. (2015). Acoustruments: Passive, Acoustically-Driven, Interactive Controls for Handheld Devices. in *Proceedings of the 33rd Annual ACM Conference on Human Factors in Computing Systems* CHI '15. (New York, NY, USA: Association for Computing Machinery), 2161–2170. doi: 10.1145/2702123.2702414.

LeCun, Y., Bengio, Y., and Hinton, G. (2015). Deep learning. *Nature* 521, 436–444. doi: 10.1038/nature14539.

Lohser, J., and Slinger, P. (2015). Lung Injury After One-Lung Ventilation: A Review of the Pathophysiologic Mechanisms Affecting the Ventilated and the Collapsed Lung. *Anesthesia & Analgesia* 121, 302. doi: 10.1213/ANE.0000000000000808.

Lu, Y. H., Hsieh, M. W., and Tong, Y. H. (1999). Unilateral vocal cord paralysis following endotracheal intubation--a case report. *Acta Anaesthesiol Sin* 37, 221–224.

McGaghie, W. C., Issenberg, S. B., Petrusa, E. R., and Scalese, R. J. (2006). Effect of practice on standardised learning outcomes in simulation-based medical education. *Medical Education* 40, 792–797. doi: 10.1111/j.1365-2929.2006.02528.x.

Mort, T. C., Keck, J. P., and Meisterling, L. (2013). "Chapter 47 - Endotracheal Tube and Respiratory Care," in *Benumof and Hagberg's Airway Management (Third Edition)*, ed. C. A. Hagberg (Philadelphia: W.B. Saunders), 957-980.e5. doi: 10.1016/B978-1-4377-2764-7.00047-6.

Narendra, R., Rajesh, P., Manish, M., and Sudhir, K. eds. (2016). Airway Management in ICU. Available at: https://doi.org/10.5005/jp/books/12670_3.

Nejla, T., Habiba, B. S. A., Oussema, J., Rim, G., Nabil, D., Mohamed, F. H., et al. (2017). Impact of Monitoring Endotracheal Cuff Pressure on Endoscopic Laryngo-Tracheal Injury: A Randomized Pilot Study. *Journal of Advances in Medicine and Medical Research*, 1–10. doi: 10.9734/JAMMR/2017/37186.

Pan, S. J., and Yang, Q. (2010). A Survey on Transfer Learning. *IEEE Transactions on Knowledge and Data Engineering* 22, 1345–1359. doi: 10.1109/TKDE.2009.191.

Pedregosa, F., Varoquaux, G., Gramfort, A., Michel, V., Thirion, B., Grisel, O., et al. (2011). Scikit-learn: Machine Learning in Python. *Journal of Machine Learning Research* 12, 2825–2830.

Salem, M. R., and Baraka, A. S. (2013). "Chapter 32 - Confirmation of Endotracheal Intubation," in *Benumof and Hagberg's Airway Management (Third Edition)*, ed. C. A. Hagberg (Philadelphia: W.B. Saunders), 657-682.e4. doi: 10.1016/B978-1-4377-2764-7.00032-4.

Stewart, S. L., Secrest, J. A., Norwood, B. R., and Zachary, R. (2003). A comparison of endotracheal tube cuff pressures using estimation techniques and direct intracuff measurement. *AANA Journal* 71.

Temko, A., and Nadeu, C. (2006). Classification of acoustic events using SVM-based clustering schemes. *Pattern Recognition* 39, 682–694. doi: 10.1016/j.patcog.2005.11.005.

Tikka, T., and Hilmi, O. J. (2019). Upper airway tract complications of endotracheal intubation. *Br J Hosp Med* 80, 441–447. doi: 10.12968/hmed.2019.80.8.441.

Trueger, N. S. (2013). "Airway management," in *Practical Emergency Resuscitation and Critical Care*, eds. J. Lee, K. Medlej, K. Shah, and S. D. Weingart (Cambridge: Cambridge University Press), 17–27. doi: 10.1017/CBO9781139523936.004.

Tsalera, E., Papadakis, A., and Samarakou, M. (2021). Comparison of Pre-Trained CNNs for Audio Classification Using Transfer Learning. *Journal of Sensor and Actuator Networks* 10, 72. doi: 10.3390/jsan10040072.

Tu, H. N., Saidi, N., Lieutaud, T., Bensaid, S., Menival, V., and Duvaldestin, P. (1999). Nitrous Oxide Increases Endotracheal Cuff Pressure and the Incidence of Tracheal Lesions in Anesthetized Patients. *Anesthesia & Analgesia* 89, 187. doi: 10.1213/00000539-199907000-00033.

Varshney, M., Sharma, K., Kumar, R., and Varshney, P. G. (2011). Appropriate depth of placement of oral endotracheal tube and its possible determinants in Indian adult patients. *Indian Journal of Anaesthesia* 55, 488. doi: 10.4103/0019-5049.89880.

Wiengand (2016). *Procedure Manual for High Acuity, Progressive, and Critical Care - E-Book*. Elsevier Health Sciences.

10 Tables

Table 1. Data breakdown

Class	Recordings	Seconds
Shallow	80	2000
Shallow, inflated cuff	80	2000
Correct	80	2000

Table 2 Classification metrics

Metric	Correct	Correct cuffed	Deep	Deep cuffed	Shallow	Shallow cuffed	Macro AVG
True positive	974	975	999	985	960	984	980
False positive	16	2	0	9	26	70	21
False negative	26	25	1	15	40	16	21
True negative	4984	4998	5000	4991	4974	4930	4980
Precision	0,984	0,998	1,000	0,991	0,974	0,934	0,980

11 Figure captions

Figure 1: Diagram of the airway showing intubation tube placement and instrumentation. A: Three progressively deep intubations in the simulated airway. Top: shallow intubation. The tube has correctly entered the trachea but at insufficient depth. Middle: correct placement deep into the trachea, but not at risk of impacting the carina. Bottom: deep intubation. The tip of the tube is hitting the carina, and the tube is on its way into the right bronchus. B: Illustration of the location of the two microphones, M1 above the airway in the nasal cavity and M2 below the airway in the left bronchus. The two buzzer configurations, B1 inside the right bronchus and B2 outside the airway in the chest cavity. Note that B1 was not in place when B2 was active, and vice versa.

Figure 2: Illustration of the SVM model pipeline. Top: Flowchart illustrating the SVM pipeline, including splitting of recordings into training and testing cohorts, the preprocessing step of highpass filtering with a 20 kHz Butterworth filter and normalization, segmenting into 0.5-second intervals, and extraction of various audio features for input to the classifier. Bottom: confusion matrices for the SVM classifier. Left: classification using the full 6-label set of both depth and cuff status. Right: classification on the reduced-size 3 label set of only tube insertion depth.

Figure 3: Illustration of YAMnet preprocessing and resulting spectrograms. Top: A step-by-step depiction of the preprocessing pipeline, including audio segmentation, normalization, highpass filtering with an 18 kHz passband Butterworth filter, resampling to a 16 kHz sample rate, computing the STFT, and applying a 64-band mel scale filterbank to generate input spectrograms with 96 frames of 10 ms duration. Bottom: Comparison of mean spectrograms from 1000 samples per case, recorded in the lower airway. Left: Buzzer located inside the airway assembly; Right: Buzzer placed in the chest cavity. The input features exhibit distinct qualitative differences.

Figure 4: Classifier performance improves as input size increases. Top: Audio was divided into 0.96-second segments from 480 recordings, each with 25 seconds of available audio. For input lengths ranging from 1 to 25 seconds, 1000 random permutations of test features were used for classification. The class was determined by the mode of the classifications. Left: Global accuracy for the four combinations of microphone and buzzer locations. Center: Global accuracy, and Left: absolute misclassifications for the top two configurations (B2). Dashed lines represent the range of classification accuracy for each set size (n=1 to 25), with color-coded histogram bins displaying the distribution of the 1000 permutations per set size. The central line indicates the mean accuracy per set size. Bottom: Confusion matrices for the CNN classifier. Left: Confusion matrix representing classifier performance on the full feature set of 12,000 seconds of recordings. Center: Classifier performance when tested on a random 1-second segment from each intubation. Right: Classification using the mode of 5 one-second segments from each intubation.

Figure 5: LIME and occlusion sensitivity maps across 1000 averaged input features in the best performing configuration.

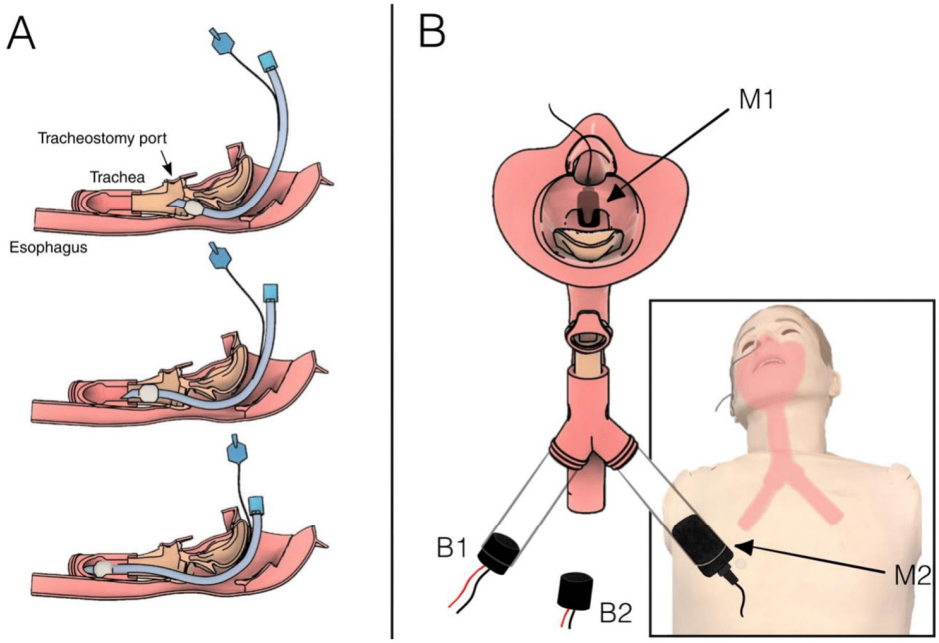

481

482

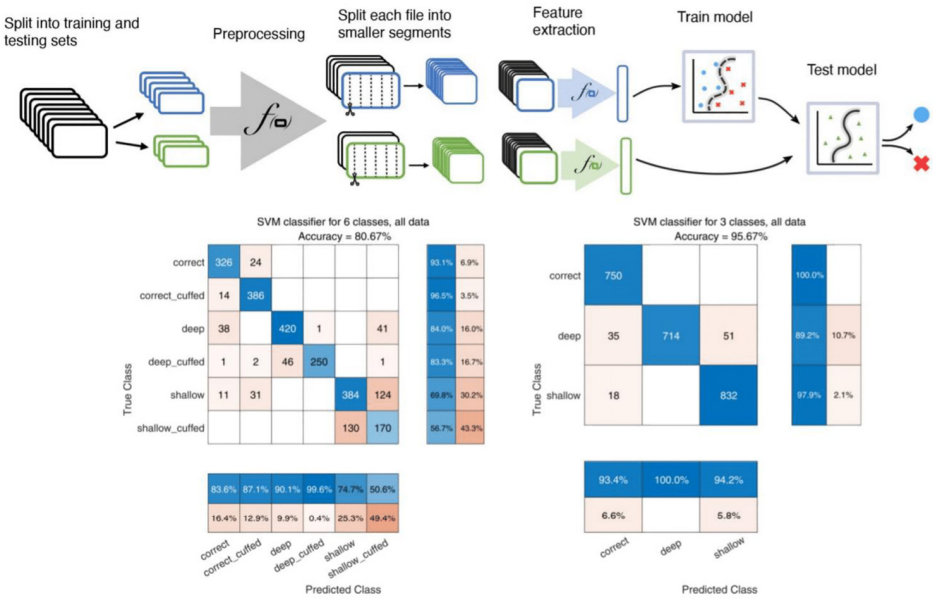
Split into training and testing sets
Preprocessing
Split each file into smaller segments
Feature extraction
Train model
Test model
SVM classifier for 6 classes, all data
Accuracy = 80.67%
correct
correct_cuffed
deep
deep_cuffed
shallow
shallow_cuffed
True Class
Predicted Class
SVM classifier for 3 classes, all data
Accuracy = 95.67%
correct
deep
shallow
True Class
Predicted Class

483

484

194

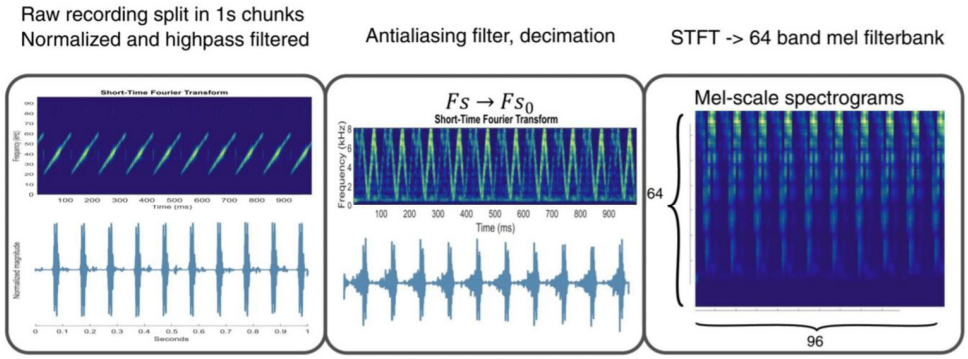
Raw recording split in 1s chunks
Normalized and highpass filtered
Antialiasing filter, decimation
STFT -> 64 band mel filterbank
Short-Time Fourier Transform
$Fs \rightarrow Fs_0$
Short-Time Fourier Transform
Mel-scale spectrograms
64
96
Time (ms)
Seconds

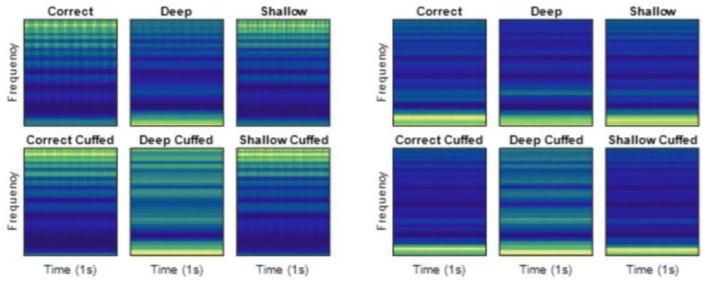
Correct
Deep
Shallow
Correct Cuffed
Deep Cuffed
Shallow Cuffed
Frequency
Time (1s)

485

486

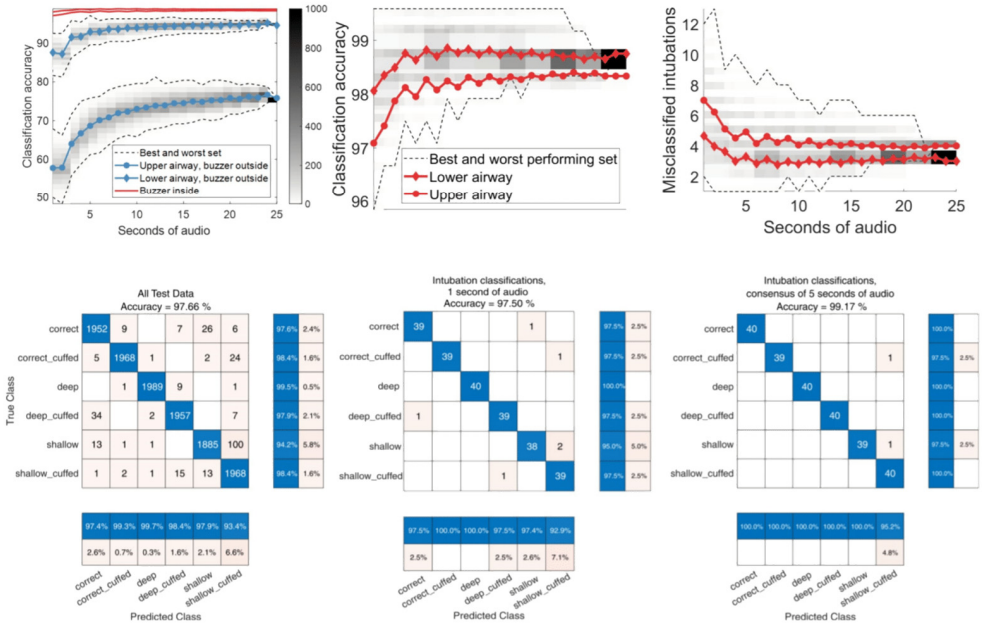
Classification accuracy
Seconds of audio
Best and worst set
Upper airway, buzzer outside
Lower airway, buzzer outside
Buzzer inside
Best and worst performing set
Lower airway
Upper airway
Misclassified intubations
All Test Data
Accuracy = 97.66 %
Intubation classifications,
1 second of audio
Accuracy = 97.50 %
Intubation classifications,
consensus of 5 seconds of audio
Accuracy = 99.17 %
True Class
Predicted Class
correct
correct_cuffed
deep
deep_cuffed
shallow
shallow_cuffed

487

488

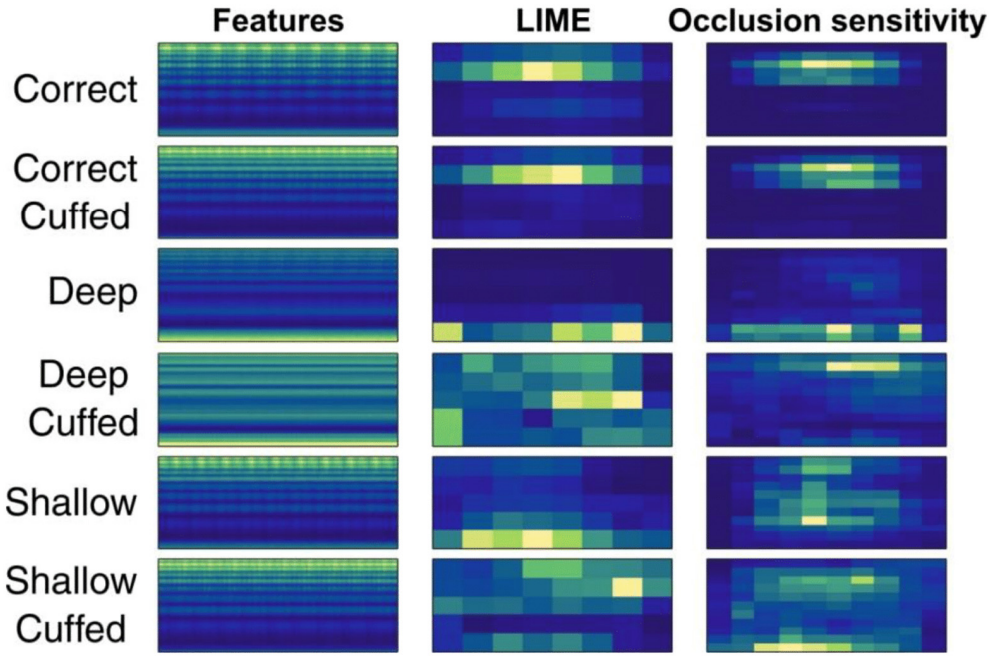
Features
LIME
Occlusion sensitivity
Correct
Correct Cuffed
Deep
Deep Cuffed
Shallow
Shallow Cuffed

489

ISBN 978-82-326-7416-9 (printed ver.)
ISBN 978-82-326-7415-2 (electronic ver.)
ISSN 1503-8181 (printed ver.)
ISSN 2703-8084 (online ver.)

NTNU

Norwegian University of
Science and Technology